

AD-A040 907

STANFORD RESEARCH INST MENLO PARK CALIF  
PREDICTIONS OF EFFECTS PRODUCED BY THE DICE THROW DETONATION ON--ETC(U)  
SEP 76 R L BOLLEN, V E HATFIELD, W G CHESNUT DNA001-76-C-0207  
DNA-4183T NL

UNCLASSIFIED

1 OF 2  
AD  
A040907



AD A 040907

12

DNA 4183T

*Topical Report*

**PREDICTIONS OF EFFECTS PRODUCED BY  
THE DICE THROW DETONATION ON  
EXPERIMENTAL MICROWAVE LINKS**

STANFORD RESEARCH INSTITUTE  
MENLO PARK, CALIFORNIA 94025

*September 1976*

CONTRACTS DNA001-76-C-0207  
and DNA001-76-C-0146

This work was supported by the Defense Nuclear Agency  
under RDT&E RMSS Code B3220 76464 S99QAXHB02602 H2590D  
and RDT&E RMSS Code B3220 76464 S99QAXHB05406 H2590D

Approved for public release; distribution unlimited.

*Prepared for:* DIRECTOR  
DEFENSE NUCLEAR AGENCY  
WASHINGTON, D.C. 20305  
Attention: RAAE/MAJ. EDMUND MUELLER



AD NO. \_\_\_\_\_  
DDC FILE COPY

Copy No. 23



UNCLASSIFIED

SECURITY CLASSIFICATION OF THIS PAGE (When Data Entered)

(19) REPORT DOCUMENTATION PAGE		READ INSTRUCTIONS BEFORE COMPLETING FORM	
1. REPORT NUMBER (18) DNA 4183T	2. GOVT ACCESSION NO.	3. RECIPIENT'S CATALOG NUMBER (9)	
4. TITLE (and Subtitle)  (6) PREDICTIONS OF EFFECTS PRODUCED BY THE DICE THROW DETONATION ON EXPERIMENTAL MICROWAVE LINKS.		5. TYPE OF REPORT & PERIOD COVERED Topical Report, Covering 1 January 1976 to 30 September 1976.	
7. AUTHOR(s) (10) Robert L. Bollen, Walter G. Chesnut, V. Elaine Hatfield, Georgellen Smith		6. PERFORMING ORG. REPORT NUMBER SRI Projects 4887 and 4756	
9. PERFORMING ORGANIZATION NAME AND ADDRESS Stanford Research Institute 333 Ravenswood Avenue Menlo Park, California 94025		8. CONTRACT OR GRANT NUMBER(s) (15) DNA001-76-C-0207 new DNA001-76-C-0146	
11. CONTROLLING OFFICE NAME AND ADDRESS Director Defense Nuclear Agency Washington, D.C. 20305		10. PROGRAM ELEMENT, PROJECT, TASK AREA & WORK UNIT NUMBERS NWED 62704H S99QAXHB026-02 NWED 62704H S99QAXHB054-06	
14. MONITORING AGENCY NAME & ADDRESS (if diff. from Controlling Office) (12) 124p.		12. REPORT DATE (11) September 1976	
		13. NO. OF PAGES 128	
		15. SECURITY CLASS. (of this report)  UNCLASSIFIED	
		15a. DECLASSIFICATION/DOWNGRADING SCHEDULE N/A	
16. DISTRIBUTION STATEMENT (of this report)  Approved for public release; distribution unlimited.			
17. DISTRIBUTION STATEMENT (of the abstract entered in Block 20, if different from report)			
18. SUPPLEMENTARY NOTES This work was sponsored by the Defense Nuclear Agency under RDT&E RMSS Code B322076464 S99QAXHB02602 H2590D.			
19. KEY WORDS (Continue on reverse side if necessary and identify by block number) DICE THROW                      Microwave absorption                      MIXED COMPANY Nuclear dust                      Lorentz-Lorenz Ejecta                      Rayleigh scattering Crater                      High explosive Microwave propagation                      SNOW BALL			
20. ABSTRACT (Continue on reverse side if necessary and identify by block number) The dust clouds produced by near-surface nuclear detonations and large-yield HE simulations of these are studied in order to produce predictions of phase and amplitude fluctuations of microwave signals that transit through these clouds. Quantitative predictions are made based on theoretical predictions of the dust cloud that is expected to be produced by the 600-ton ANFO high-explosive test code-named DICE THROW. These predictions are made for the paths and frequencies that will be used in an experimental probing by microwave links of the DICE THROW (continued) → next page			

DD FORM 1473  
1 JAN 73  
EDITION OF 1 NOV 65 IS OBSOLETE

UNCLASSIFIED

SECURITY CLASSIFICATION OF THIS PAGE (When Data Entered)

iii

332 500

13

PRECEDING PAGE, BLANK, NOT FILMED

UNCLASSIFIED

SECURITY CLASSIFICATION OF THIS PAGE (When Data Entered)

19. KEY WORDS (Continued)

20 ABSTRACT (Continued)

*cont.* dust cloud. A photographic comparison of HE and nuclear detonations is also given in order to determine the detonation altitude of a nuclear device that will be best simulated by the DICE THROW test.

It is concluded that crater ejecta will dominate the DICE THROW dust cloud generation. The dust cloud geometry probably will best simulate that produced by a kiloton nuclear device buried more than several but less than (approximately) 15 feet (~5 meters). Calculations, based on a particle size distribution that contains some large particles thought to be appropriate to ejecta clouds, show attenuation perhaps reaching 10 dB at X band (10,188 MHz) on some paths within the first one second following detonation. The attenuation is expected to decrease and be insignificant by approximately 10 seconds due to the fallout of large particles. Phase changes due to dust occulting various propagation paths will exceed 50 radians ( $3000^\circ$ ) along some X-band paths during the first second following detonation. A phase change exceeding 10 to 15 radians is predicted to be observed for more than 60 seconds. Measurable phase shifts will be detectable for many minutes that are produced by dust densities that drop to values as low as  $10^{-7}$  g/cm<sup>3</sup>. Other effects of propagation on the microwave signals such as diffraction and shock wave occultation are discussed.

UNCLASSIFIED

SECURITY CLASSIFICATION OF THIS PAGE (When Data Entered)

*Blank*

## CONTENTS

LIST OF ILLUSTRATIONS . . . . .	vii
LIST OF TABLES. . . . .	ix
ACKNOWLEDGMENTS . . . . .	xi
EXECUTIVE SUMMARY . . . . .	xiii
1. INTRODUCTION . . . . .	1
2. PHENOMENOLOGICAL DESCRIPTION OF FEATURES EXPECTED FROM DICE THROW HIGH-EXPLOSIVE DETONATION . . . . .	5
2.1 Overall Dust Cloud Morphology . . . . .	7
2.1.1 Early Time--Up to Five Seconds . . . . .	7
2.1.2 Cratering. . . . .	10
2.1.3 Intermediate Time--Five to Fifteen Seconds . . . . .	12
2.1.4 Late Time--After Fifteen Seconds . . . . .	14
2.2 Photographic Geometry of HE and Nuclear Dust Clouds . . . . .	17
2.3 Measurements of Dimension from PDT II-2 Photographs . . . . .	34
2.4 Summary . . . . .	36
3. THEORETICAL PREDICTIONS OF THE DICE THROW DUST ENVIRONMENT. . . . .	39
3.1 High-Explosive Burn . . . . .	40
3.2 Flow-Field Calculations in the Atmosphere . . . . .	40
3.3 Examples of Dust Density Distribution . . . . .	44
3.4 Examples of Dust Density Calculations for Early-Time Ejecta. . . . .	49
4. MICROWAVE PROPAGATION AND PREDICTIONS FOR DICE THROW . . . . .	53
4.1 Description of Microwave Propagation Experiment . . . . .	53
4.2 Description of Various Effects on Microwave Propagation Expected from the DICE THROW Detonation . . . . .	58

4. MICROWAVE PROPAGATION AND PREDICTIONS FOR DICE THROW (continued)	
4.2.1 Phase Variations Produced by Dust. . . . .	59
4.2.2 Attenuation (Extinction) by Dust Particles . . .	63
4.2.3 Diffraction and Refraction Phenomena . . . . .	71
4.3 Prediction for Microwave Propagation Experiment on DICE THROW. . . . .	74
5. SUMMARY AND CONCLUSION . . . . .	85

#### APPENDICES

A. ANALYTICAL EJECTA MODEL . . . . .	89
B. BRIEF DESCRIPTION OF HULL/DUSTY ANFO CALCULATIONS AS PROVIDED BY THE AFWL. . . . .	95
C. DEMONSTRATION OF EFFECT OF ZONING SIZE IN FIREBALL REGION ON CLOUD RISE VELOCITY . . . . .	101

UNCLASSIFIED	
UNANNOUNCED	
JUSTIFICATION	
BY	
DISTRIBUTION AVAILABLE TO	
Dist.	AVAIL. SHOW
A	



## ILLUSTRATIONS

2.1	Early-Time Phenomenology . . . . .	8
2.2	Idealized Crater Profile from a Near-Surface Detonation. .	10
2.3	Intermediate-Time Phenomenology. . . . .	13
2.4	Late-Time Dust and Debris Phenomenology. . . . .	15
2.5	Terminal Velocity vs Particle Diameter . . . . .	16
2.6	100-T TNT, Pre-DICE THROW II-1 . . . . .	21
2.7	100-T ANFO, Canadian 1969. . . . .	21
2.8	120-T ANFO, Pre-DICE THROW II-2. . . . .	21
2.9	1.2-kT Nuclear at -17 ft Buster Jangle: Uncle, 1951 . . .	21
2.10	0.5-kT Nuclear at -2 ft Johnny Boy, 1962 . . . . .	21
2.11	1.2-kT Nuclear at +4 ft Buster Jangle: Sugar, 1951. . . .	21
2.12	Comparison of Two Different Charge Configurations of 500 tons, TNT. . . . .	29
2.13	Photographs of Mixed Company III at Late Times (TNT 500-T tangent sphere). . . . .	31
2.14	Measured Ejecta and Cloud Height vs Time for PDT II-2. . .	35
3.1	AFWL Flow-Field Calculations for DICE THROW and 500-T TNT Tangent Sphere at 7 s. . . . .	42
3.2	AFWL Flow-Field Calculations for DICE THROW and 500-T TNT Tangent Sphere at 15 s . . . . .	43
3.3	Example of Particle Position Plots and Dust Density Contours for DICE THROW. . . . .	46
3.4	Geometry Used in Analytical Simulation of AFWL Ejecta- Injection Technique. . . . .	48
3.5	Comparison of AFWL Dusty and Analytic Density Distribution Along 60° Elevation. . . . .	49
3.6	Expected Height vs Time of DICE THROW Ejecta . . . . .	50
3.7	Integrated Dust Density Along Three Propagation Paths Using Analytical Ejecta Procedure. . . . .	51

4.1	Plan View of DICE THROW Microwave Transmission Experiment . . . . .	55
4.2	Elevation View of Lines of Sight in Plane of Ground Zero and Frequencies Employed . . . . .	56
4.3	DICE THROW Site Geometry . . . . .	57
4.4	Phase Retardation vs Dust Density for a 1-km Path with Uniform Dust Loading . . . . .	62
4.5	Fraction of Mass per Centimeter of Radius vs Radius for Two Particle-Size Distributions. . . . .	67
4.6	Cumulative Absorption Coefficient, $\alpha(a)$ , vs Radius, $a$ , for Two Particle-Size Distributions. . . . .	69
4.7	e-Folding Extinction Distance as a Function of Dust Density. . . . .	70
4.8	Diffraction Phenomena Produced by a Cylindrical Dust Cloud. . . . .	72
4.9	Yield-Scaled Photographs of PDT II-2 Showing Anticipated Intersection of Propagation Paths with DICE THROW Phenomena. . . . .	75
4.10	Predicted Attenuation and Phase Change vs Time--Path 1 . .	78
4.11	Predicted Attenuation and Phase Change vs Time--Path 2 . .	78
4.12	Predicted Attenuation and Phase Change vs Time--Path 3 . .	79
4.13	Predicted Attenuation and Phase Change vs Time--Path 4 . .	79
4.14	Predicted Attenuation and Phase Change vs Time--Path 5 . .	80
4.15	Early-Time Phase Path Variation for Three Propagation Paths. . . . .	81
A-1	Schematic Distribution of Dirt Utilizing AFWL Technique at 1 s . . . . .	92
A-2	Geometric Schematic of Dust Ejection . . . . .	94
C-1	Maximum Velocity in Grid vs Time for Two High-Explosive Situations . . . . .	104



## TABLES

2.1	Properties of Explosions Photographically Illustrated in Figures 2.6 through 2.13. . . . .	20
2.2	Measurements of Various Quantities as a Function of Time from PDT II-2 Photographs. . . . .	36
4.1	Particle-Size Distribution A . . . . .	66
4.2	Particle-Size Distribution B . . . . .	66
B-1	Total Mesh Size Versus Time. . . . .	98
B-2	Particle Radius Versus Fraction of Ejecta Mass . . . . .	99

#### ACKNOWLEDGMENTS

This report represents a cooperative effort between SRI and the Theoretical Group, Hydrodynamics Section, of the Air Force Weapons Laboratory. Major Gary Ganong, Dr. Charles Needham, and Mrs. Susan Check of the AFWL performed a great many calculations for us and were exceptionally responsive to our many requests. This work would not have been possible without their cooperation. We thank Dr. Robert Henny of the AFWL Shock Physics Section for providing guidance on cratering phenomena.

The photographs in Section 2 were furnished by various organizations. Dr. Walter Dudziak, of Information Sciences, Inc., very generously provided the three sets of nuclear photographs in Section 2. We are particularly grateful to him for permitting us to publish them at this time, even prior to publication of his own compilation of nuclear-detonation phenomenology.

The photographs of high-explosive tests in Section 2 were furnished by Dr. A. D. Thornbrough of Sandia Laboratories (Pre-DICE THROW II-1 and 2); and Drs. Colin McKivor and J. S. Watson of the Defense Research Establishment Suffield (Canadian 1969 ANFO Series and SNOWBALL).

We are also grateful to Drs. John Wisotski and William Snyder of the Denver Research Institute for their guidance at the outset of this effort and their assistance in locating photographs, and to Dr. Joseph Petes of the Naval Surface Weapons Center for sending additional photographs. We also wish to thank Captain Tom Edwards and Capt. Vicen Alvarez for their cooperation.

The authors also thank Mr. Walter Jaye of the Radio Physics Laboratory at SRI for numerous helpful suggestions concerning this work. Ms. Patricia

Crawley, also of SRI, was responsible for much of the work associated with measuring photographs and with detailed photographic layouts.

The efforts contained in this report were performed under Contract DNA001-76-C-0207; however, the contributions by one of the authors (WGC) were supported principally by Contract DNA001-76-C-0146.

## EXECUTIVE SUMMARY

The detonation of a nuclear weapon near the earth's surface causes the lofting of enormous quantities of soil to very great altitudes (above 20 to 25 km for megaton-class detonations). In the 1950s and early 1960s, nuclear-produced dust clouds were tracked by radar for many hours, attesting to the long residence time of large-size dust particles at very high altitudes. In recent years sophisticated military communication systems have placed an increasing reliance on maintaining phase coherence in order to improve overall performance. However, during a nuclear engagement the large quantities of dust and debris that will be present over widespread areas for long periods of time can produce serious degradation of the performance of phase-coherent systems. The magnitude of the expected degradation has never been experimentally determined. The effects of the dust and debris on a forward-propagating communication signal (to and from satellites, for example) cannot be deduced from radar backscatter data because radar clutter from dust clouds is produced primarily by the incoherent backscattering of energy by independent particles; the phase effects of concern here are produced by the coherent addition of this same scattered energy, but in the forward direction. The effects in the forward direction are also affected by turbulence, diffraction, and refraction at the very least.

An innovative microwave forward-transmission experiment using phase-coherent signals will be performed during the DICE THROW high-explosive simulation test scheduled for 6 October 1976 at the White Sands Missile Range. Measurements will be made of both phase and amplitude of signals transmitted through various portions of the dust cloud created by the explosion. The experiment, designed and executed by Stanford Research

Institute under the auspices of the Atmospheric Effects Division, Radiation Directorate, of the Defense Nuclear Agency, will provide the first empirical data on the performance degradation of phase-coherent communication systems in explosion-produced dust clouds. It is also expected to provide the first quantitative measure of dust loading at early times in the immediate vicinity of ground zero. More specifically, the phase data are expected to provide a direct and essentially unambiguous measure of the integrated dust density in various portions of the cloud on a time scale of milliseconds to minutes.

The objective of the research reported in this document has been to investigate means whereby the unique diagnostics provided by the transmission experiment can be used to improve theoretical models of nuclear and HE dust clouds. To this end, we have worked closely with the developers of the HULL/DUSTY code at the Air Force Weapons Laboratory (AFWL) to produce a model for DICE THROW that represents our combined best estimates of the configuration and mass loading of the ejecta cloud during the first 60 s after detonation. Using the mass density values predicted by HULL/DUSTY, we have made quantitative predictions of the phase and amplitude effects to be measured in the microwave experiment. This report presents the results of that analysis.

Several of the parameters used by the AFWL as inputs to these DUSTY computations were derived by SRI from photographs of the 120-ton Pre-DICE THROW II-2 test (referred to here as PDT II-2), with linear dimensions and time scaled up by the cube root of five in anticipation of the 600-ton DICE THROW event. The PDT II-2 dust cloud was chosen as the scale model for DICE THROW because, to our knowledge, it is the only example of a large detonation using the same explosive material (ammonium nitrate and fuel oil, commonly called ANFO) in a similar charge configuration (that of a cylinder with a hemispherical cap). After examining photographs of



several HE tests, we are convinced that the gross structure of the dust cloud is determined largely by the shape of the charge.

There was little evidence in PDT II-2 of the rising vortex ring and trailing stem that have characterized previous tests in which the charge was a TNT tangent sphere or hemisphere. Instead, the cloud was dominated by ejecta thrown out of the crater at relatively discrete elevation angles. In the absence of any other data, we have assumed that the DICE THROW cloud will have essentially these same features--despite the significant differences in geology between the two sites and the fact that most of the region around ground zero has been backfilled with fine blow sand to suppress large ejecta.

The experimental data will be gathered over six propagation paths, five of which are expected to intersect the early-time dust cloud. Three paths will intersect the cloud only 10 m above the ground, thereby yielding new diagnostic data on crater ejecta almost from the instant of detonation. One of these low-altitude paths passes directly above ground zero; the others are offset laterally by 40 and 120 m, respectively. The fourth path, directly above ground zero, will intersect the cloud when it reaches a height of 190 m. The two remaining paths also cross the normal plane through ground zero at the 190 m altitude but at lateral distances of 230 and 720 m; the latter is not expected to intersect the dust cloud. Data will be recorded at six harmonically related frequencies from UHF (~400 MHz) to X-band (~10 GHz), all phase-locked to a common reference to permit measurement of coherent phase shifts. (Not all frequencies will be used on all paths.)

Our best estimates of the RF effects that will be observed in the microwave experiment on DICE THROW are given in the report. They can be briefly summarized as follows:

- Measurable phase shifts will be observed at all implemented frequencies on four, and perhaps five, paths.



- Dust-induced phase shifts during the first second will exceed 50 rad at X-band on the two lower paths nearest to ground zero, and will exceed 10 to 15 rad for more than a minute. (These estimates assume 8 kT of crater ejecta and can be scaled linearly when the actual crater dimensions are known.)
- Signal attenuation is expected to be small--at most about 10 dB at X-band on the lower paths--and to become negligible within 10 to 15 s.

In view of the many uncertainties in the basic dust models and the fact that the hydrodynamic codes were not designed for this purpose, we do not expect these predictions to be very accurate. However, our goal was not so much to make accurate predictions for DICE THROW as to provide an avenue for better prediction in the future. The most important conclusion of this predictive effort is that quite large phase shifts will be produced, thereby providing the means for improving the dust-loading model. Furthermore, even if the crater size has been overestimated by as much as an order of magnitude, measurable phase shifts will still be observed. This report details each stage of the predictive process and calls attention to uncertainties and potential sources of error at each stage. We have stated not only the values of the parameters used in the model, but also the rationale for their selection.

The ultimate objective of a high explosive simulation test is to extrapolate the results to nuclear situations. Because of the paucity of relevant data on nuclear dust clouds, one must rely entirely on theoretical models such as HULL and DUSTY. We suggest, however, that existing photographic records of nuclear events contain a wealth of information that, to our knowledge, has not been exploited as a source of inputs to the theoretical codes. Though not a reliable indicator of dust density, the photographs clearly reveal the gross features of the cloud. In the development of the dust-cloud model for DICE THROW, the input parameters were derived from measurements of the visible features of the PDT II-2

cloud. Should this prove to be a valid technique in this instance, a similar analysis of the photographs of nuclear detonations would seem a logical means of enhancing present capabilities in the modeling of nuclear dust clouds.

Several sequences of nuclear and HE tests are displayed in Section 2 in a format that facilitates comparison at about the same times after burst. The phrase PHOTOGRAPH NOT AVAILABLE on the figures means that an appropriate photograph is not known to exist. The PDT II-2 cloud is most similar in appearance to the slightly buried nuclear events. On the basis of this photographic evidence we anticipate that the DICE THROW cloud will best simulate that of a slightly buried nuclear detonation.

## 1. INTRODUCTION

The detonation of a nuclear weapon near the earth's surface causes the lofting of enormous quantities of soil to very great altitudes (above 20 to 25 km for megaton-class detonations). In the 1950s and early 1960s, nuclear-produced dust clouds were tracked by radar for many hours, attesting to the long residence time of large-size dust particles at very high altitudes. In recent years sophisticated military communication systems have placed an increasing reliance on maintaining phase coherence in order to improve overall performance. However, during a nuclear engagement the large quantities of dust and debris that will be present over widespread areas for long periods of time can produce serious degradation of the performance of phase-coherent systems. The magnitude of the expected degradation has never been experimentally determined. The effects of the dust and debris on a forward-propagating communication signal (to and from satellites, for example) cannot be deduced from radar backscatter data because radar clutter from dust clouds is produced primarily by the incoherent backscattering of energy by independent particles; the phase effects of concern here are produced by the coherent addition of this same scattered energy, but in the forward direction. The effects in the forward direction are also affected by turbulence, diffraction, and refraction at the very least.

During October 1976 a 600-ton high-explosive charge (DICE THROW) composed of ammonium nitrate and fuel oil (ANFO) will be detonated at White Sands Missile Range in an attempt to simulate a wide variety of nuclear effects. A propagation experiment will be performed by SRI in conjunction with this test in which coherent microwave signals will propagate through various portions of the dust cloud caused by the

explosion. The amplitude and phase change will be measured at phase coherent frequencies ranging from 400 MHz (UHF) up to 10 GHz (X band). In addition to providing data of direct interest to communication problems, the experiment will provide a survivable diagnostic of the integrated dust density along each of several paths through the dust cloud. This will be the first time such phase coherent propagation measurements have been made on either a high explosive or nuclear test.

One of the important goals of the transmission experiment is to provide inputs to theoreticians engaged in modeling of nuclear dust clouds. These codes are the only means of generalization, and their reliability is limited by insufficient input data. Since extrapolation to the nuclear case can be done only through such theoretical codes, it is important to examine their ability to model the high-explosive dust environment, where some degree of verification is possible. Accordingly, we have worked closely with the developers of the HULL/DUSTY code at the Air Force Weapons Laboratory (AFWL) to produce a model for DICE THROW that represents our combined best estimates of the configuration and mass loading of the ejecta cloud during the first 60 s after detonation.

Using the theoretical mass-density values provided by HULL/DUSTY, we have made quantitative predictions of the phase shift and amplitude effects to be measured in the microwave experiment. This report presents the results of that analysis. After the experiment, these predictions can be compared with the analyzed experimental data to improve the theoretical definition of the dust environment.

The AFWL calculations require a model for injection of dust into their computer routines. The model that we have used is based on dimensions measured from photographs of the pre-DICE THROW, 120-ton ANFO detonation experiment that we consider to be a scale model for the DICE THROW event. Predictions of the dust and debris are dependent on a number of variables

such as the type, size, shape, and position of the explosive as well as the geology of the test site. Therefore these various phenomena have been studied and conclusions drawn.

There exists a large body of experimental and theoretical work on dust lofting that we have not used in our efforts. The primary reason for this apparent neglect is that we expect that the ejecta cloud will dominate the microwave propagation effects during DICE THROW. Successful prior experimental measurements of dust size distributions and mass densities have been performed very near the ground in the sweep-up regions or in the very high altitude, late-time dust cloud. The microwave experiment will probe the very high density dust in the extreme overpressure regions where prior experiments could not survive. Dust particle size distributions were measured by the Kaman Corp. following the PDT II-2 test which is our scale model for DICE THROW predictions. However, their closest sensor, though located near the ground at 150 m from ground zero, did not start to sample dust until 90 s following detonation, long after the time of principal concern in our predictions.

As stated previously, the theoretical predictions of the DICE THROW dust environment were made by the Air Force Weapons Laboratory. We are well aware of the existence of other predictive codes such as DICE, VORDUM, SCOUR, etc. However, within the constraints of time and funds, it was not possible for us to work with more than one organization. The SHELL and HULL hydrodynamic codes are widely used and highly respected in the nuclear community. Therefore, it was agreed by SRI and DNA representatives at the outset of this study that the AFWL should perform the dust calculations needed for the microwave predictive effort. The collaboration with the AFWL has been, from our point of view, very fruitful.



The report is organized as follows: Section 2 first presents a description of the phenomenology of the dust clouds produced by near surface explosions. Then, in order to determine the relationship between the DICE THROW and nuclear-produced dust clouds, a number of photographs are presented and studied. Finally, the cloud features of the pre-DICE THROW 120-ton ANFO test (PDT II-2) are measured for later use in making predictions for DICE THROW. Section 3 discusses the theoretical and computational techniques used by the AFWL in their generation of dust models for DICE THROW for our use in studying propagation. We also describe an analytical procedure based on an AFWL scheme that we use to scale ejecta densities during the ejecta deployment. Section 4 first presents a brief description of the microwave propagation experiment that will be performed during DICE THROW. This is followed by an outline of expected propagation effects to be produced by DICE THROW. Then equations for relating amplitude and phase changes to the characteristics of the dust environment are presented. These are used to compute dust effects on optical/IR and microwave signals for simple, generic situations in order to lay an intuitive foundation for the quantitative theoretical predictions that are presented at the end of Section 4. Section 5 presents the conclusions of our study and predictive effort.



## 2. PHENOMENOLOGICAL DESCRIPTION OF FEATURES EXPECTED FROM DICE THROW HIGH EXPLOSIVE DETONATION

In this section we describe the visible features of the dirt and dust lofted by high-explosive (HE) detonation on the surface of the earth. We also compare nuclear- and HE-produced dust phenomena. Generally the HE experiments are designed to simulate the effects of the shock wave produced by nuclear detonations in order to test survivability of complex military structures. The dust cloud of concern in this report has been considered an unwanted problem by these other experimenters. Some attempts have been made in the past to measure the properties of certain features of the dust/ejecta clouds in order to learn about reentry-vehicle erosion problems, for example; however, equipment for in-situ measurements that can survive the blast and projectile (missile) effects is nearly impossible to design.

The microwave links of the experiment of concern here probe and survive even the highest overpressure regions. Thus, all dust phenomena may be probed; it is therefore necessary to describe and name these various features for the reader whose background and concerns have been, as were ours, radio and microwave propagation. Should the reader feel well acquainted with the explosion phenomena, he should feel free to scan or even bypass Section 2.1, which describes the generic phenomena.

Of greatest concern to the microwave propagation experiment is the relationship between HE-produced and nuclear produced dust and its consequent effect on propagation. A variety of questions need to be answered: On the microscale, are the dust particles produced by high explosives similar or dissimilar to those produced by nuclear detonations over the same soil? The comparisons concern not only dust particle intrinsic

density, shape and size distribution, but also its dielectric properties. On the macroscale, is the mass loading of the various portions of the dust cloud similar, or scalable for the two kinds of explosives? Are the generic overall geometries of the clouds similar--including vorticity and turbulent mixing features? Finally, do surface HE detonations best simulate nuclear detonations on the surface, under the surface, or above the surface?

On the microscale, dust in some of the HE-produced cloud features should be similar to the nuclear-produced dust. Dust lofted by gust loading of surface dirt must fall into this category. On the other hand, dust from the craters could be very different for the two kinds of explosions because of thermal phenomena associated with nuclear detonations. We have not pursued this particular aspect very far.

So far as we know, little attention has been paid to the question of the relationships of the overall cloud geometries. In order to obtain a better perspective on this important point, we were fortunate to obtain series of photographs of various geometries of high explosives and three series of photos of nuclear detonations moderately deep, slightly buried, and slightly above surface. The comparisons, presented in Section 2.2, suggest that the geometries of the macroclouds produced by some surface detonations (e.g., PDT II-2) "look more like" buried nuclear detonations than air bursts. On the other hand, the photographs show that the HE cloud geometry differs for different geometries of the high explosives. Thus, we believe that there is no simple, clear-cut answer to the question of what nuclear dust phenomena are simulated by surface detonations of high explosives.

We first describe dust macrophenomenology produced by high explosives.

## 2.1 Overall Dust Cloud Morphology

We have found that differing terminology may be used to describe the same explosive phenomena. The reader may note that some of our names are at variance with his own usage. The description of generic explosive effects will be divided into time domains designated early, intermediate, and late. The domain divisions depend on yield, of course. The prominence of the various features we describe depends on many factors; our generic descriptions are therefore inaccurate for any specific case. As an example, the DICE THROW charge is a hemispherically capped cylinder of ANFO with a total weight of 600 tons. In our predictions for this event we have relied heavily on the cloud morphology of the pre-DICE THROW event II-2, a 120-ton scale-model ANFO test. We refer to this detonation as PDT II-2. This scale-model detonation did not produce the strongly characteristic features of the late-time domain of nuclear detonations such as an intense vortex ring trailing a stem. Nevertheless, we describe these as important late-time effects because they are the dominant late-time features of nuclear detonations that are either near-surface or subsurface detonations that vent substantial fireball material into the atmosphere. Our descriptions below apply mainly to HE phenomena produced by weights of explosives in the regime of hundreds of tons.

### 2.1.1 Early Time--Up to Five Seconds

At very early times (on the order of a millisecond from initial detonation) the shock conditions have been established at the boundaries between the explosive charge and air and also between the explosive charge and ground. The main determinants for the shock conditions are the size and shape of the charge, the type of explosive, and the position of the detonators. Of these three, experiment and computer simulation seem to show that the shape of the charge is most

critical in determining subsequent events such as ejecta cloud and fireball shape, vorticity, and rise velocity.

Still at early times--say, up to 5 s for our purposes--the ejecta spires have reached their peak altitude,  $H$ , and the surface surge has reached its maximum diameter,  $S_d$ . Figure 2.1 is a schematic representation of the environment at this time. The ejecta spires are believed to be jets of dirt that, because of air erosion, leave a wake of small particles behind on their upward bound trajectory. For the case of PDT II-2 the maximum altitude,  $H$ , of the spires was about 200 m, and the diameter,  $S_d$ , of the surface surge was on the order of 350 m. The spires have been launched at some minimum elevation angle,  $E$ , measured from the horizontal; this angle apparently is highly dependent on the shape of the charge and the geological condition of the ground in the blast area. There is some photographic evidence that a maximum ejection angle,  $E_m$ , also exists.

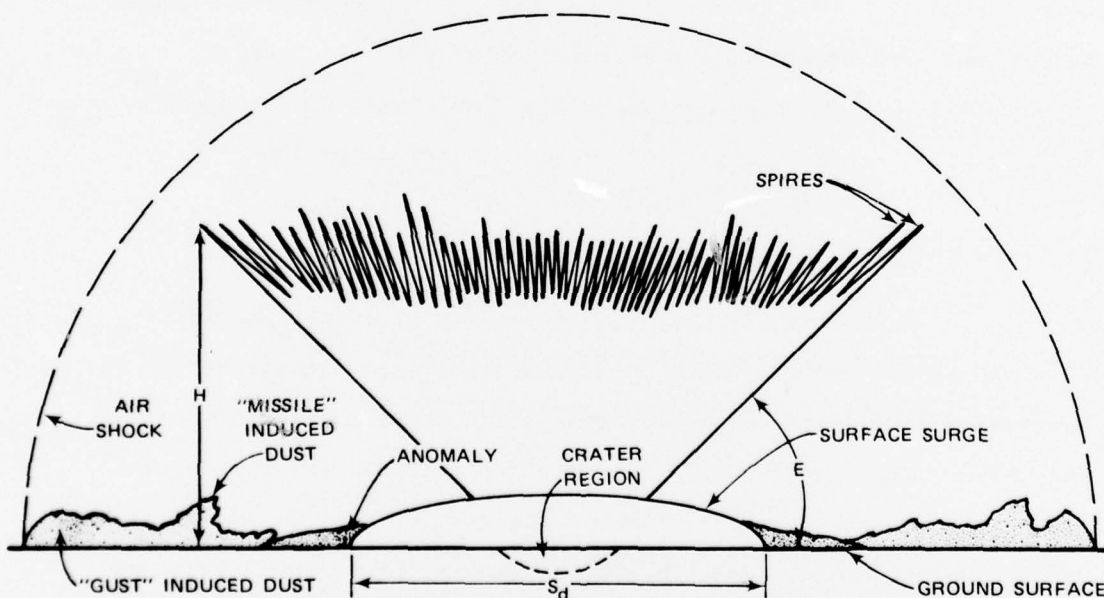


FIGURE 2.1 EARLY-TIME PHENOMENOLOGY



The very high pressures and velocities associated with the air shock wave lift substantial quantities of dust off the surface. Several mechanisms may play a role in generating this "gust-lofted" material. Aerodynamic drag (shear forces) in the surface boundary layer generates turbulence and lifting forces. During the intense positive-pressure phase of the shock, air flows into interstices in the ground, momentarily pressurizing the soil. During the negative (reduced-pressure) phase, as the air attempts to escape it may cause surface spalling or blow-off of soil upward into the reverse winds. Ground impact of large missiles ejected from the crater will raise finer dust particles up into the air. It is apparent that the amount of material that can be lofted by these processes taking place outside of the crater region is strongly dependent on the character of the ground in the detonation area. The maximum altitude,  $h$ , of this gust-lofted dust is on the order of 10 m at early time for HE charges in the range of hundreds of tons. The dust may be carried to greater heights and set into turbulent motion by high-velocity afterwinds.

On some past TNT tests, anomalies have been noted in the initial fireball such that one or more jets of hot, high-explosive material travel laterally outward past the surface surge. These jets are possibly caused by Rayleigh-Taylor instabilities in the region between the HE and the ground.

Nuclear events have a further lofting mechanism from X-rays, neutrons, and thermal radiation that deposit energy in the ground on very short time scales. This energy deposition can cause a change of state of the soil, and boiling of water constituents; these changes are thought to result in dust-lofting forces. This mechanism, sometimes called "popcorning," is not present in HE detonations. For purposes of this report all dust and debris not associated with the cratering process and ejecta will be called "sweep-up" material.

### 2.1.2 Cratering

The crater is discussed at this point because it is by far the largest source (at least 70%) of dust and debris for surface and shallow-buried nuclear and HE bursts. Figure 2.2 presents a schematic cross

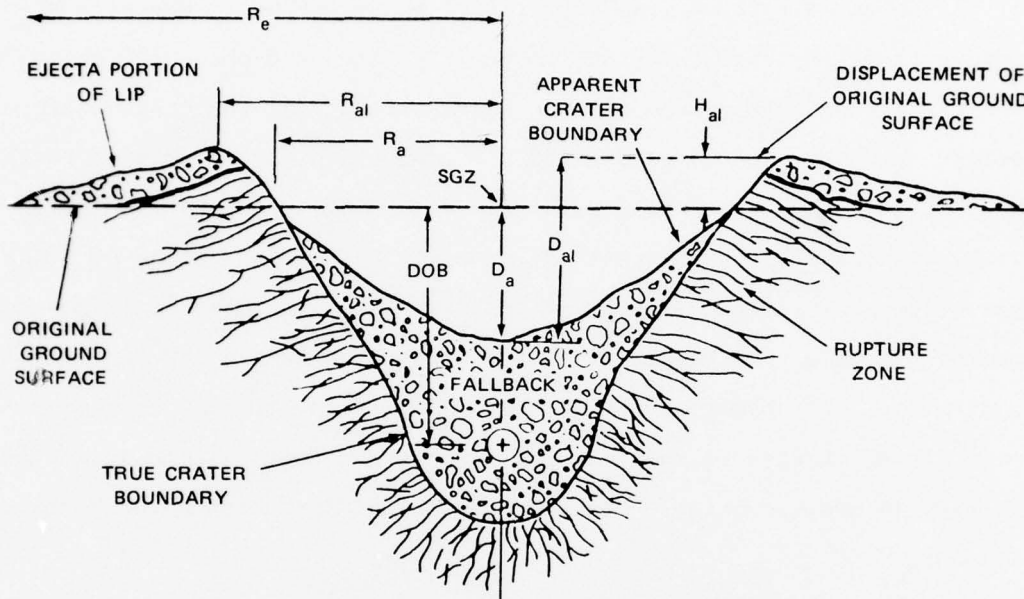


FIGURE 2.2 IDEALIZED CRATER PROFILE FROM A NEAR-SURFACE DETONATION

section of a crater produced by a near-surface detonation. A variety of terms pertaining to the crater are defined in this drawing. The subscript  $a$ , on various parameters, stands for apparent or visible crater dimension. The true crater boundary represents the limits to which earth has been permanently displaced; "fallback" is material that has fallen back into the true crater. Nuclear detonations that are even slightly off the surface do not seem to produce large craters; as a result, the sweep-up material is the major source of debris for bursts above about 10 ft scaled to 1 kT.



A very important difference between surface HE and surface nuclear tests is that high explosives have a much higher cratering efficiency\* and hence eject considerably more material into the air for the same yield. For instance, in the same geology, TNT surface detonations produce craters whose volume may range from seven to 20 times that of a surface nuclear burst of the same yield. If the nuclear device is even slightly buried, the nuclear cratering efficiency increases dramatically.

A possible reason for the large difference in cratering efficiency between nuclear and HE surface detonations is that the high explosive has a much larger surface area in contact with the soil. The large mass of the high explosive covering a larger surface area makes for efficient momentum coupling and thereby shock-wave initiation in the ground. The energy from a nuclear detonation is primarily emitted in the form of various kinds of radiation; the X-radiations from a near-surface detonation will cause heating of a thin surface layer of dirt leading to intense blow-off. We surmise, from experimental evidence, that the momentum of this blow-off is small compared with the momentum transferred by mass impact in the case of HE detonations. The very high-pressure nuclear fireball also will impart some momentum to the soil, but again, comparison of results suggests that the mass of the HE is much more efficient in coupling momentum to the soil.

Theoretical and empirical attempts to estimate the size of the crater and therefore the mass of material lofted into the air are often frustrated by the difficulties in predicting the material equation of state and constitutive properties for in situ geologic materials. However, two extreme cases are clear. A surface charge on hard rock, not

---

\* Cratering efficiency is defined as cubic feet of material permanently displaced from the crater region per ton of TNT yield.

surprisingly, yields a relatively small crater; the maximum size crater seems to occur in wet soil or in cases where the water table is near the surface. The PDT II-2 shot, done in preparation for the upcoming 600-ton DICE THROW shot, was an example of this latter case. This has led to a degree of uncertainty in attempting to extrapolate data pertaining to the crater size and, hence, quantity of ejecta material, from the smaller PDT II-2 test to the upcoming large DICE THROW test; the DICE THROW geologic setting is very different and has furthermore been extensively modified to reduce the number of large, solid chunks (rocks, for example) that are called missiles.

The AFWL estimate of cratering efficiency, with consideration of the layered geology at the DICE THROW site, is on the order of  $300 \text{ ft}^3/\text{ton}$  of TNT; for the 500-ton TNT equivalent DICE THROW detonation, this efficiency produces approximately  $1.5 \times 10^5 \text{ ft}^3$  of crater ejecta. The total mass of the DICE THROW crater is thereby estimated to be on the order of 9 kT of material based on a predetonation average density of  $1.92 \text{ g/gm}^3$  ( $120 \text{ lb/ft}^3$ ). The estimation of the amount of this crater material that is lofted into the air is very uncertain and therefore is a large source of uncertainty in radio propagation predictions. We shall use 8 kT in our later estimates.

#### 2.1.3 Intermediate Time--Five to Fifteen Seconds

At intermediate time of 5 to 15 s the overall shape of the cloud of residual dust and debris is similar to that of the initial explosion. Figure 2.3 presents a schematic representation of the dust cloud during this time interval. A layer of residual dust resulting from gust lofting, missile impacts, and surface surge is also present near the ground. A rising fireball may or may not be visible above the debris cloud. We shall see later that the presence or absence of a rapidly

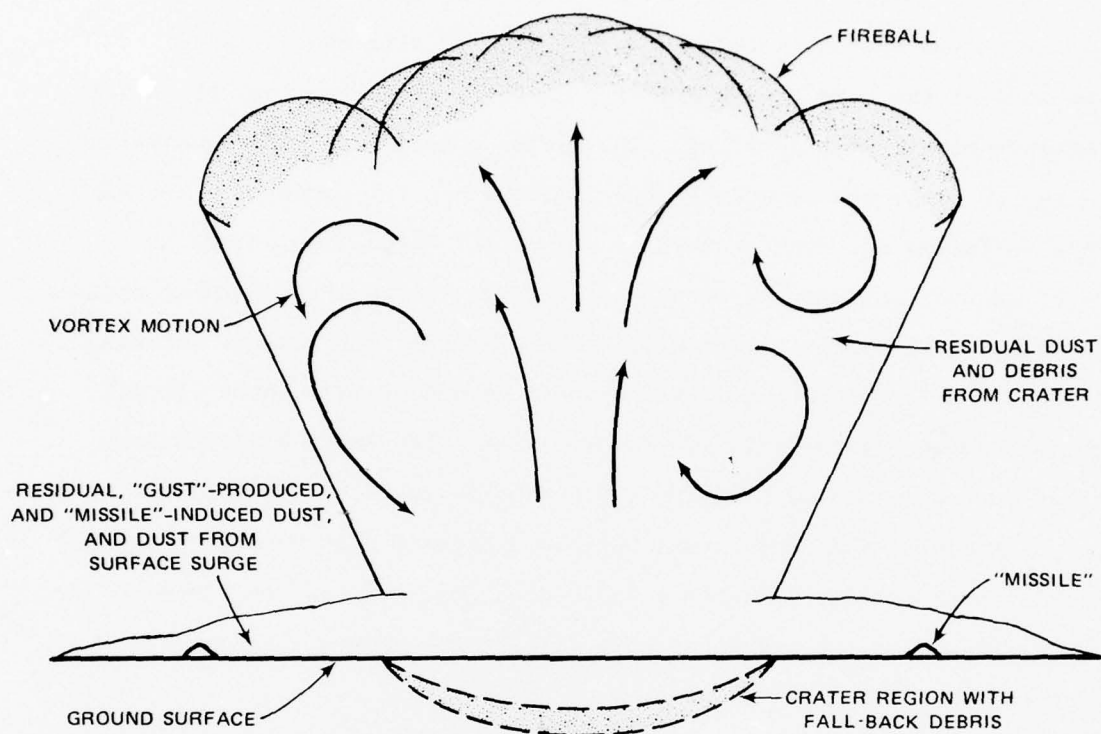


FIGURE 2.3 INTERMEDIATE-TIME PHENOMENOLOGY

rising and convecting fireball is probably determined in the high-explosive case by the initial charge shape and perhaps to a lesser extent by the combustion properties of the explosive material.

The air flow fields at intermediate time in the debris cloud are determined by the initial shock condition produced at very early times and by intrinsic buoyancy of the residual hot, gaseous products of the explosion. As we show later, calculations by AFWL, as well as experiment, suggest that the initial air shock depends most heavily on the shape of the explosive charge. The intermediate time flow fields within the debris cloud are in turn affected and, since they are the main factor in the spatial and temporal distribution of the cloud debris, the latter are also affected by charge shape.

Although the charge shape is thought to be the most important factor in the hydrodynamics, there may also be differences between TNT and ANFO of the same charge geometry in the fireball region; these differences may be associated with the "after burning" of large quantities of carbon compounds present in the TNT that are not present in the ANFO. Some estimates are that as much as 30% of TNT detonation energy is released over an interval of tens of seconds in the after burning process. The glowing fireball that results is very evident for several seconds following detonation in the photographic record of TNT shots; optical emissions cease very early after ANFO shots. The large difference in emission properties of ANFO and TNT fireballs suggests that the TNT after-burn introduces some additional buoyancy that may play some part in causing hydrodynamic behavioral differences between the two types of explosives. The questions raised here have not been quantitatively answered as far as we know.

In the case of slightly buried nuclear tests, there is a phenomenon termed "base surge" in which a cylindrical column of material is thrown upward from underground and exhibits some of the properties of an aerosol. Quantities of material fall in the immediate vicinity of ground zero because their density is greater than air, with the finer particles spreading radially outward along the ground to form a dust cloud. The shallower the detonation depth, the less favorable the conditions are for a significant base surge.

#### 2.1.4 Late-Time--After Fifteen Seconds

At late time, past 15 s or more, cool air rushes in to fill the void or low pressure region caused by the rising vortex ring. Figure 2.4 presents a schematic of the environment during this phase. The cool air that rushes inward and flows in a column upward behind the vortex ring picks up and carries along with it residual dust (sweep



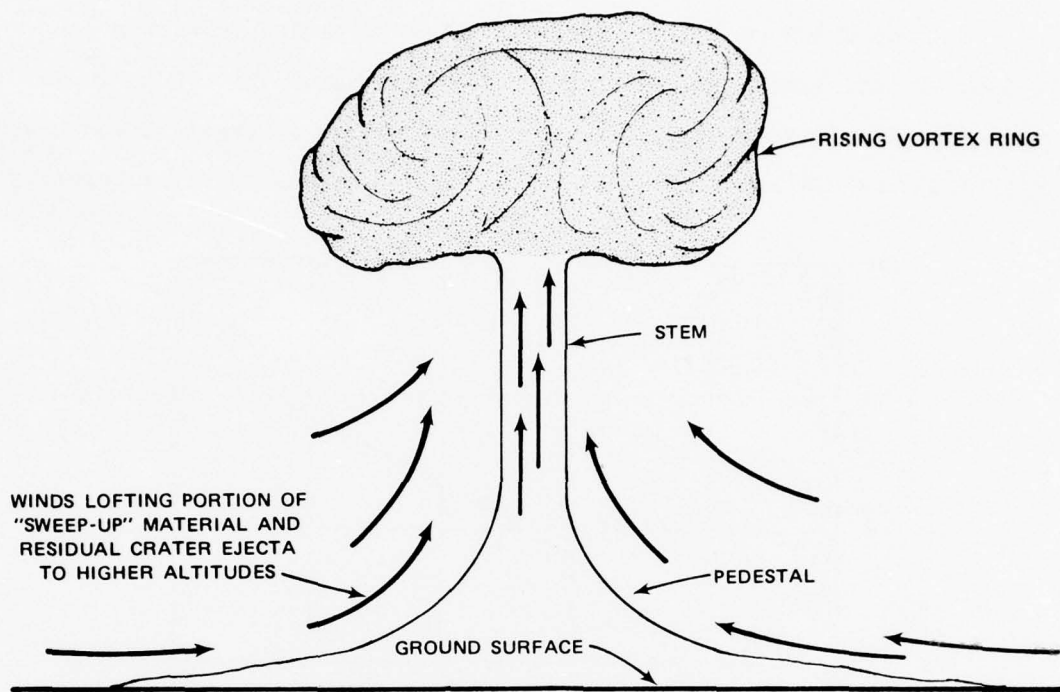


FIGURE 2.4 LATE-TIME DUST AND DEBRIS PHENOMENOLOGY

up pedestal) from all of the early-time sources discussed in previous subsections. The dust, carried up the "stem," often catches up and becomes entrained in the rising vortex ring. The dust that ends up in the rising vortex ring and stem will be called "entrained" dust. The maximum altitude attained by the vortex ring depends primarily on the explosive yield, the shape of the charge, and atmospheric conditions. When the vortex ring ceases to rise, the cloud is said to have stabilized. Stabilization altitudes vary from several kilometers for the DICE THROW size HE detonations to over 20 km and above for megaton nuclear detonations. Ambient winds will then dominate the dispersal of all debris.

There was little evidence of sweep-up winds, stem, or rising vortex ring in the case of the hemispherically capped cylinder of PDT II-2. The DICE THROW charge, because of its identical shape and type of explosive, is expected to exhibit similar behavior.



For a 500-ton burst, almost all the particles remaining entrained at late time are less than 1 cm in diameter. This is because the terminal velocity\* of larger, heavier particles is greater, and hence they "fall out" at earlier times. Figure 2.5 presents terminal velocity

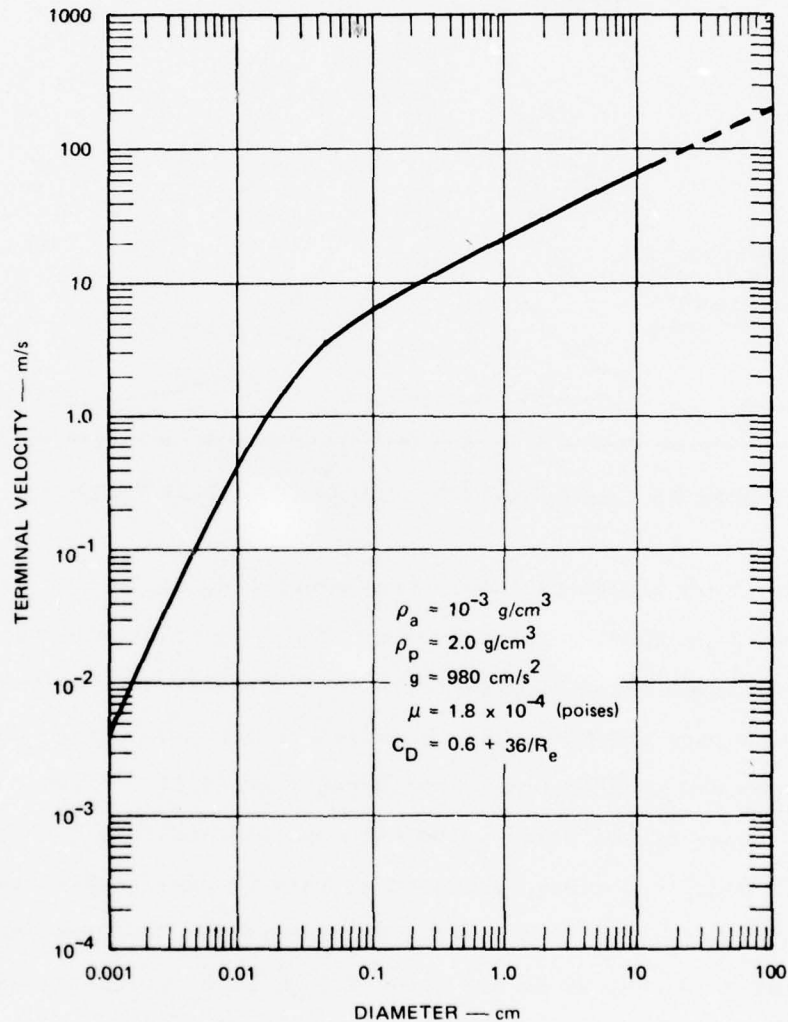


FIGURE 2.5 TERMINAL VELOCITY vs PARTICLE DIAMETER

\* The terminal velocity is the maximum velocity a particle of given size, mass, and shape can attain under free-fall conditions retarded by atmospheric drag.

versus diameter for spherical particles having a density of  $2 \text{ g/cm}^3$  (about that of desert alluvium). As an example, a 1-cm-diameter, sphere-shaped particle, initially lofted to a height of 200 m, would reach the ground in approximately 10 s at a terminal velocity of 22 m/s. Because effects of atmospheric drag are more important for smaller particles, their terminal velocities are lower. Thus, a particle 0.01 cm in diameter has a terminal velocity of only 40 cm/s so that, ignoring air-flow fields, it would take 500 s to fall to the ground from the same height.

A widely quoted "rule of thumb" for estimating the maximum total mass of dust in a nuclear cloud is "1 MT of dust per MT of yield." This is considered to be the hydrodynamic limit for megaton-class weapons; the rule is derived from AFWL calculations using the SHELL code, and applies at late times--say about 5 minutes for a 1-MT weapon detonated at sea level. Since only a small fraction of the material initially ejected will be entrained and suspended for several minutes, our estimate of 8 to 9 kT for the DICE THROW cloud at 1 s does not conflict with this hydrodynamic limit.

## 2.2 Photographic Geometry of HE and Nuclear Dust Clouds

The primary reason for performing the microwave experiment during DICE THROW is to provide data that are relevant to developing propagation models in nuclear produced dust. Since propagation effects are determined by detailed characteristics of the dust environments, it is important to attempt to determine the relationships between nuclear-produced and HE-produced dust clouds.

As indicated at the beginning of this section, we are interested in all characteristics from the very small (dust-particle size and shape distribution, and dielectric properties) through the very large (overall cloud morphology). Information about the microscopic characteristics of

the dust particles, though not sparse, is very complex and confusing, and undoubtedly varies with time and place within the cloud and depends on the type of explosive. We show in Section 4 that detailed cloud dust densities and particle size distribution within these regions probably cannot be accurately determined from photographic records. On the other hand, photographic records do provide excellent information concerning the spatial and temporal distribution of explosively produced dust clouds. On this basis, the photographic records should enable us to form some general conclusions regarding the similarities and differences between various explosions.

In this subsection we present and study a number of photographs of the dust clouds produced by various HE and nuclear detonations. The general overall characteristics of nuclear dust clouds will be shown to be very dependent on the height of burst (negative heights included) of nuclear detonations. We also find that the photographic dust cloud morphology of surface HE detonations depends on charge shape. We suppose, but have no records to prove, that the dust cloud details may be affected also by the kind of high explosive that is used.

The series of photographs we present here have provided us with a rather different overall view than we had previously held of the relationship between dust clouds from surface HE detonations and near surface nuclear detonations. Our general conclusion is that, based only upon the qualitative behavior of the photographically recorded dust clouds of the buried nuclear charges and the PDT II-2 ANFO hemispherically capped cylinder, the DICE THROW dust cloud will best simulate that from a slightly buried nuclear charge. This opinion does not carry over, though, to the comparison of particle size distribution; we do not yet know how to make a sensible comparison here.

We present a large number of photographs of a number of explosions covering the evolution of their dust clouds from early to late times. Table 2.1 lists the properties of the explosive tests that are photographically covered in this section.

In order to permit better comparison of cloud features, Figures 2.6 through 2.11 are presented side by side in columnar form. The first three of these are HE experiments using differing charge geometries but each with the same total energy. The last three are nuclear explosions performed at three depths: buried 17 ft, buried 2 ft, and 4 ft above the ground surface. The yields of the nuclear charges are greater than the HE charges; therefore, perhaps we should use "scaled times" for our comparisons, but we are uncertain as to how to choose such a scale change. Historically, for atmospheric detonations, one would scale times and lengths according to cube root of yield with perhaps an additional factor of two for shock effectiveness of HE compared with the nuclear. For scaling purposes from PDT II-2 to DICE THROW, we have used the cube root scaling. Again, we have used no yield scaling for Figures 2.6 through 2.13.

Figures 2.12(a) and 2.12(b) present photographic comparisons of two geometries of TNT showing important similarities and differences. Figure 2.13 carries the photographic coverage of Figure 2.12(b) to considerably later times to illustrate the classical vortex cloud followed by a stem that we associate with above-the-ground nuclear detonations.

Figures 2.6 through 2.8 present photographs of three HE charges of varying geometries. Figure 2.8 is a series of the PDT II-2 test whose geometric characteristics are expected to be like those from DICE THROW. Unlike the clouds of Figures 2.6 and 2.7, which are a TNT tangent sphere and an ANFO hemisphere respectively, the PDT II-2 test did not produce an intense vortex ring followed by the stem. Theoretical calculations

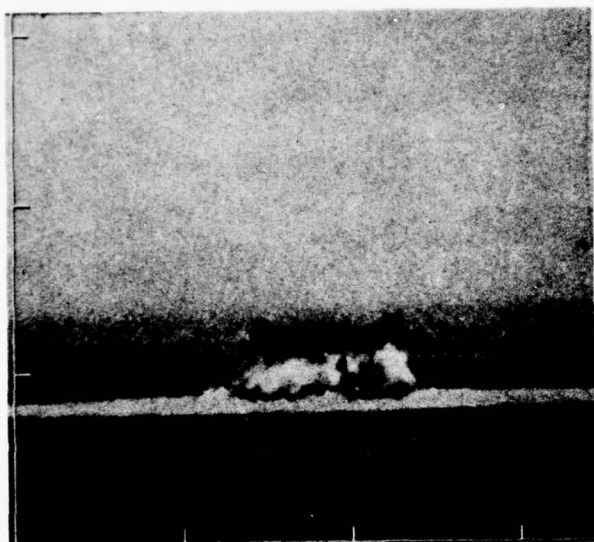
Table 2.1

PROPERTIES OF THE EXPLOSIONS PHOTOGRAPHICALLY ILLUSTRATED  
ON FIGURES 2.6 THROUGH 2.13

	Figure 2.6	Figure 2.7	Figure 2.8	Figure 2.9	Figure 2.10	Figure 2.11	Figure 2.12(a)	Figures 2.12(b) & 2.13
Code name	Pre-DICE THROW II-1	Canadian	Pre-DICE THROW II-2	Buster Jangle: Uncle	Johnny Boy	Buster Jangle: Sugar	Snowball	Mixed Company III
Explosive material	TNT	ANFO	ANFO	Nuclear	Nuclear	Nuclear	TNT	TNT
Yield	100 tons	100 tons Equiv. (120 tons actual weight)	120 tons	1.2 kT	0.5 kT	1.2 kT	500 tons	500 tons
Charge shape & position	Tangent sphere	Tangent hemisphere	Tangent hemispheri- cal capped cylinder (ratio of height of cylinder to diameter: 0.75)	-17 ft	-2 ft	+4 ft	Tangent hemisphere	Tangent sphere
Location	White Sands Missile Range, New Mexico	Watching Hill Test Range, Suffield, Canada	White Sands Missile Range, New Mexico	Nevada Test Site	Nevada Test Site	Nevada Test Site	Suffield Experi- mental Blast Range, Canada	Glade Park, Colorado
Date	8-12-75 1100 LT	8-28-69 1100 LT	9-22-75 1200 LT	11-29-51 1200 LT	7-11-62 0841 LT	11-19-51 0900 LT	Summer 1964	11-13-72 1140 LT

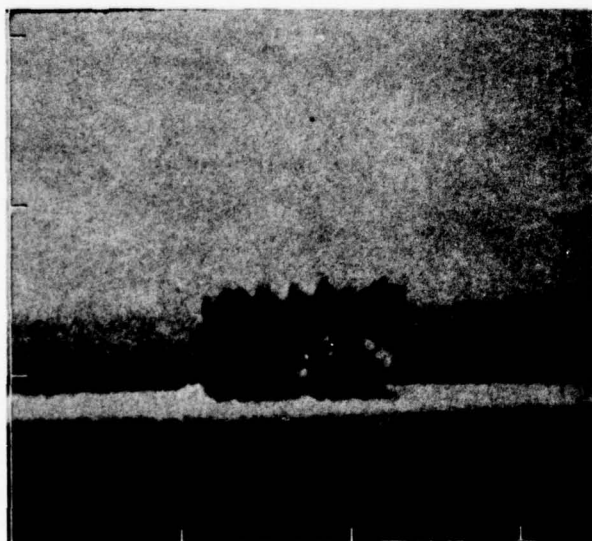


FIGURE 2.6 100-T TNT, PRE-DICE THROW II-1  
(photos courtesy of A. D. Thornbrough,  
Sandia Labs)



← 200 m →

(a) 1 SECOND



← 200 m →

(b) 2 SECONDS

FIGURE 2.7 100-T ANFO, CANADIAN 1969  
(photos courtesy of J. S. Watson,  
DRES, Canada)



← 100 m →

(a) 1 SECOND



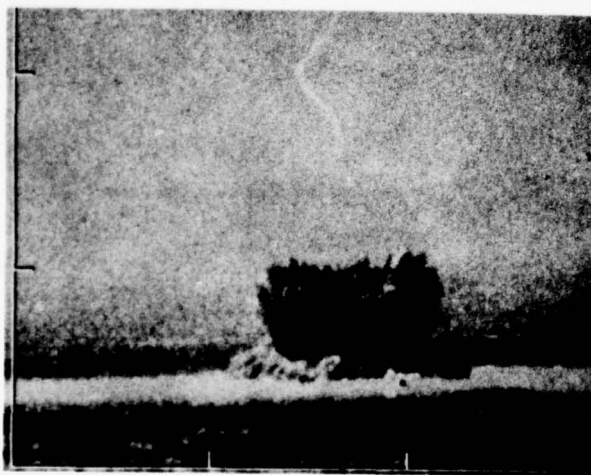
← 100 m →

(b) 2 SECONDS

FIGURE 2.8 120-T ANFO, PRE-DICE THROW II-2  
(photos courtesy of A. D. Thornbrough,  
Sandia Labs)



(a) 1 SECOND

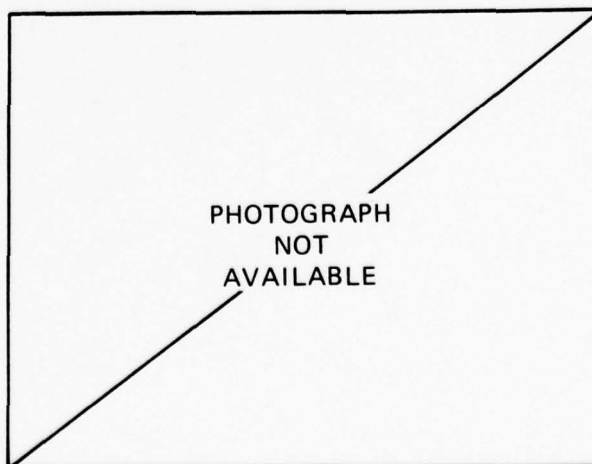


(b) 2 SECONDS

FIGURE 2.9 1.2-kT NUCLEAR AT -17 ft,  
BUSTER JANGLE: UNCLE, 1951  
(photos courtesy of W. Dudziak,  
Information Sciences, Inc.)



(a) 1 SECOND

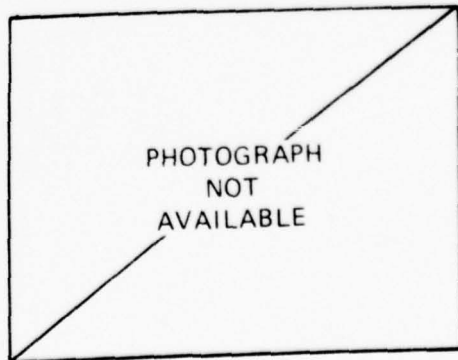
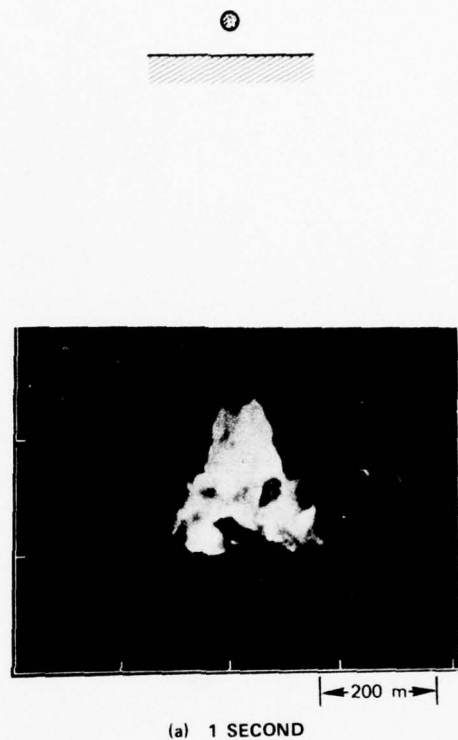


ft,  
E, 1951  
dziak,

FIGURE 2.10 0.5-kT NUCLEAR AT -2 ft,  
JOHNNY BOY, 1962  
(photos courtesy of W. Dudziak,  
Information Sciences, Inc.)

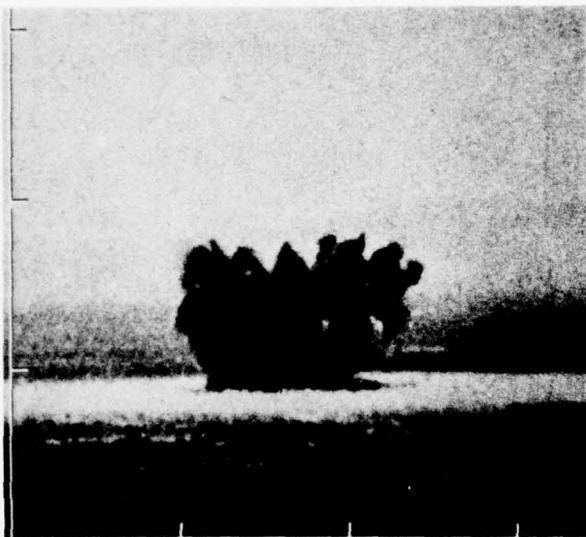


FIGURE 2.11 1.2-kT NUCLEAR AT +4 ft,  
BUSTER JANGLE: SUGAR, 1951  
(photos courtesy of W. Dudziak,  
Information Sciences, Inc.)



3

FIGURE 2.6 100-T TNT, PRE-DICE THROW II-1  
(photos courtesy of A. D. Thornbrough,  
Sandia Labs)



(c) 4 SECONDS

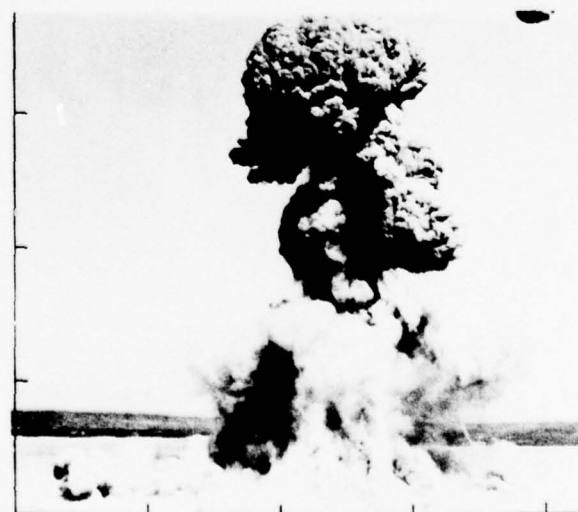
FIGURE 2.7 100-T ANFO, CANADIAN 1969  
(photos courtesy of J. S. Watson,  
DRES, Canada)



(c) 4 SECONDS



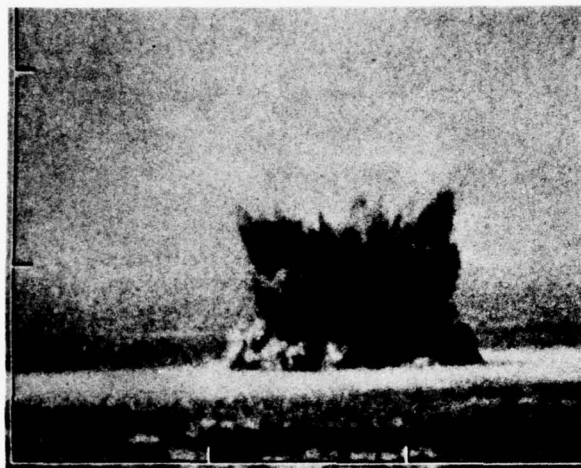
(d) 8 SECONDS



(d) 6 SECONDS



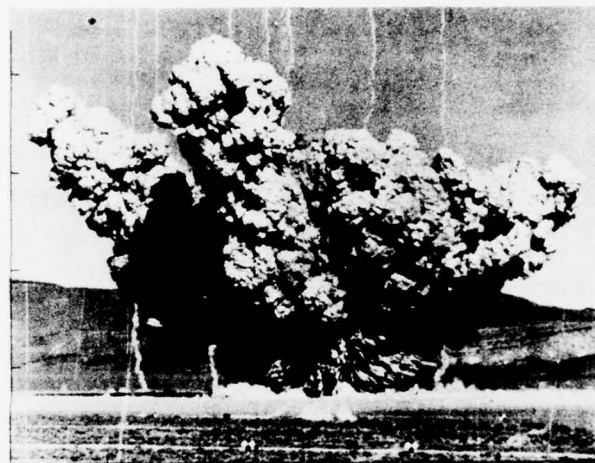
FIGURE 2.8 120-T ANFO, PRE-DICE THROW II-2  
(photos courtesy of A. D. Thornbrough,  
Sandia Labs)



(c) 4 SECONDS

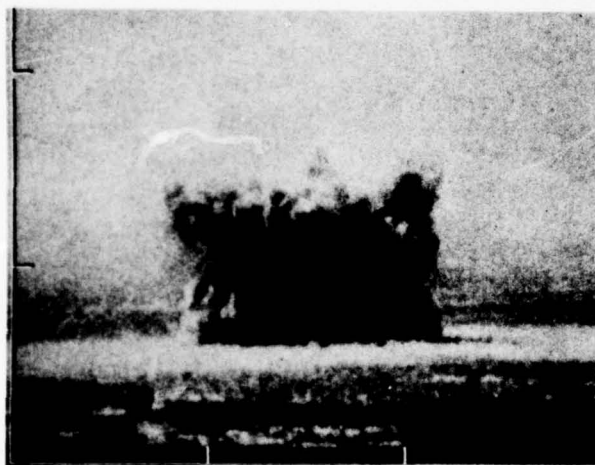
← 200 m →

FIGURE 2.9 1.2-kT NUCLEAR AT -17 ft,  
BUSTER JANGLE: UNCLE, 1951  
(photos courtesy of W. Dudziak,  
Information Sciences, Inc.)



(c) 4 SECONDS

← 200 m →



(d) 8 SECONDS

← 200 m →



(d) 8 SECONDS

← 200 m →



FIGURE 2.10 0.5-kT NUCLEAR AT -2 ft,  
JOHNNY BOY, 1962  
(photos courtesy of W. Dudziak,  
Information Sciences, Inc.)

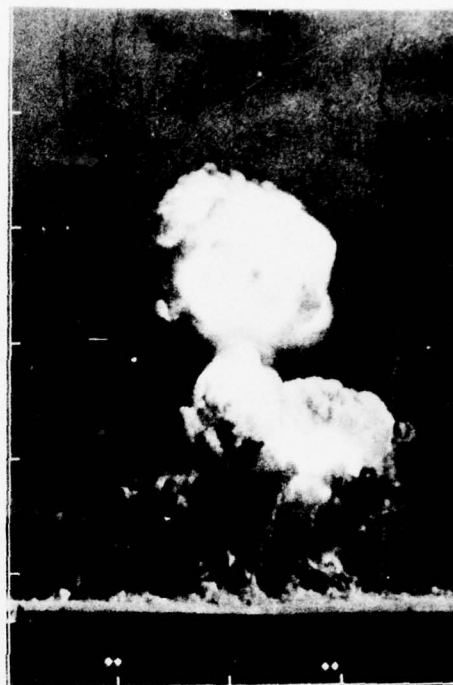


(c) 4 SECONDS



(d) 8 SECONDS

FIGURE 2.11 1.2-kT NUCLEAR AT +4 ft,  
BUSTER JANGLE: SUGAR, 1951  
(photos courtesy of W. Dudziak,  
Information Sciences, Inc.)



(c) 4 SECONDS



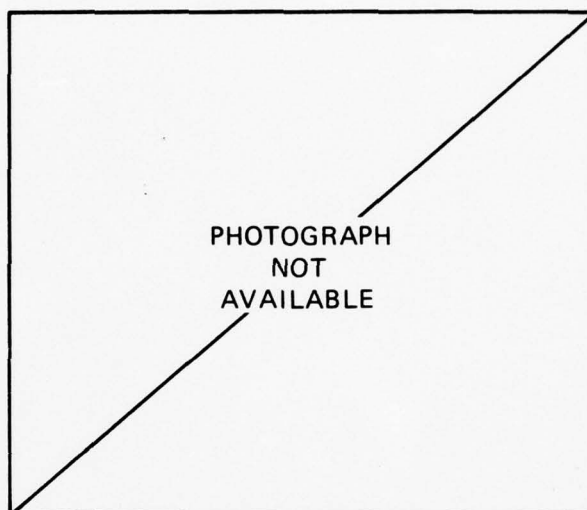
(d) 8 SECONDS

FIGURE 2.6 100-T TNT, PRE-DICE THROW II-1  
(photos courtesy of A. D. Thornbrough,  
Sandia Labs)



(e) 12 SECONDS

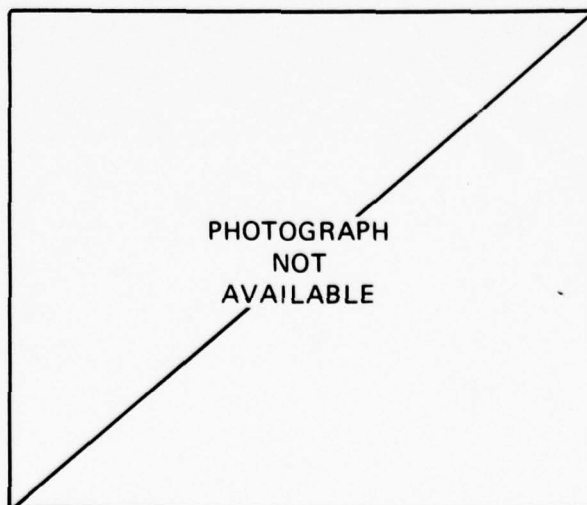
FIGURE 2.7 100-T ANFO, CANADIAN 1969  
(photos courtesy of J. S. Watson,  
DRES, Canada)



(e) 12 SECONDS

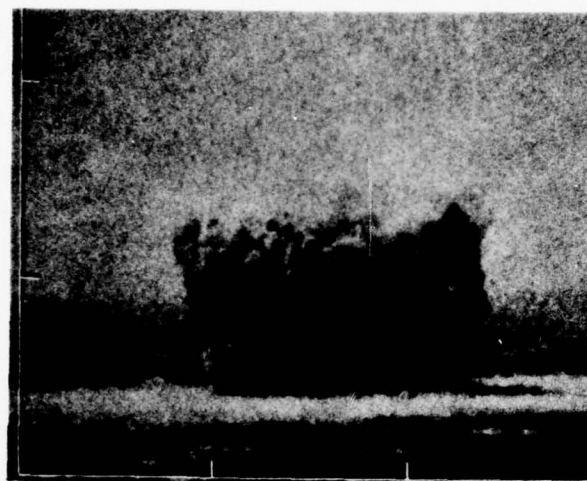


(f) 20 SECONDS

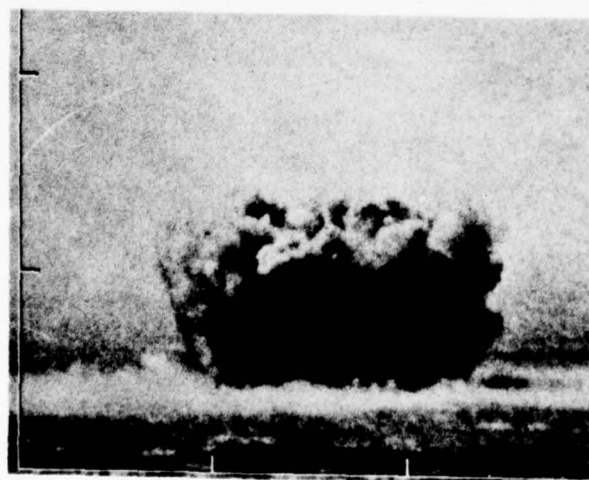


(f) 20 SECONDS

FIGURE 2.8 120-T ANFO, PRE-DICE THROW II-2  
(photos courtesy of A. D. Thornbrough,  
Sandia Labs)

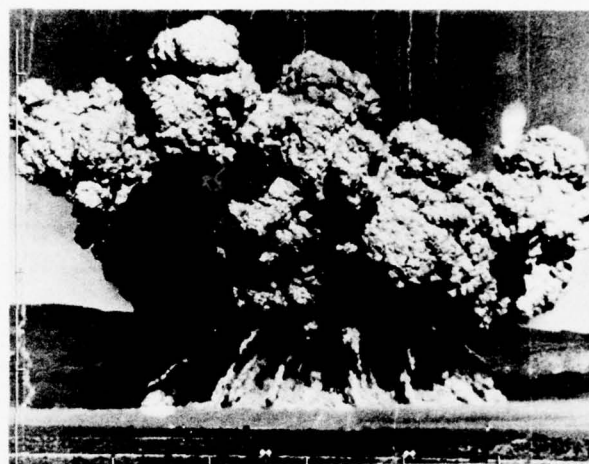


(e) 12 SECONDS

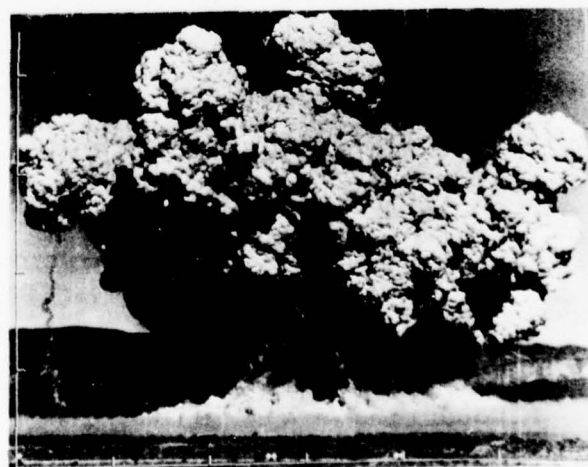


(f) 20 SECONDS

FIGURE 2.9 1.2-kT NUCLEAR AT -17 ft,  
BUSTER JANGLE: UNCLE, 1951  
(photos courtesy of W. Dudziak,  
Information Sciences, Inc.)



(e) 12 SECONDS



(f) 20 SECONDS

7 ft,  
LE, 1951  
Dudziak,

FIGURE 2.10 0.5-kT NUCLEAR AT -2 ft,  
JOHNNY BOY, 1962  
(photos courtesy of W. Dudziak,  
Information Sciences, Inc.)

FIGURE 2.11 1.2-kT NUCLEAR AT +4 ft,  
BUSTER JANGLE: SUGAR, 1951  
(photos courtesy of W. Dudziak,  
Information Sciences, Inc.)



(e) 12 SECONDS

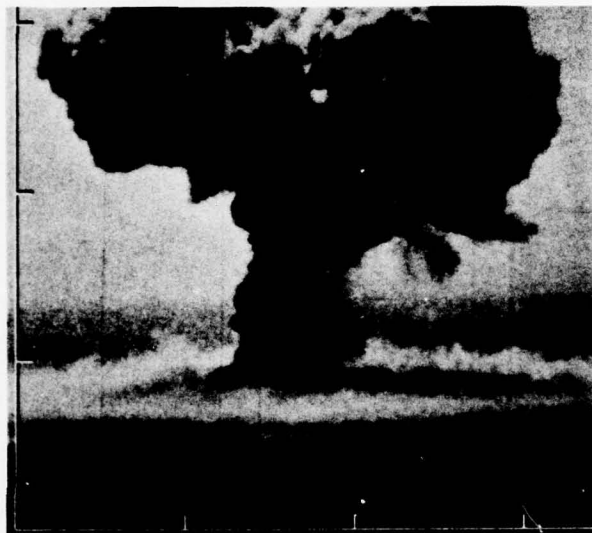
(e) 12 SECONDS



(f) 20 SECONDS

(f) 20 SECONDS

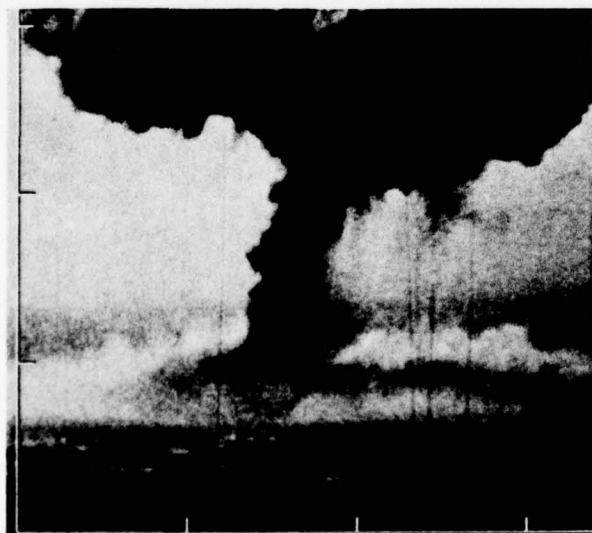
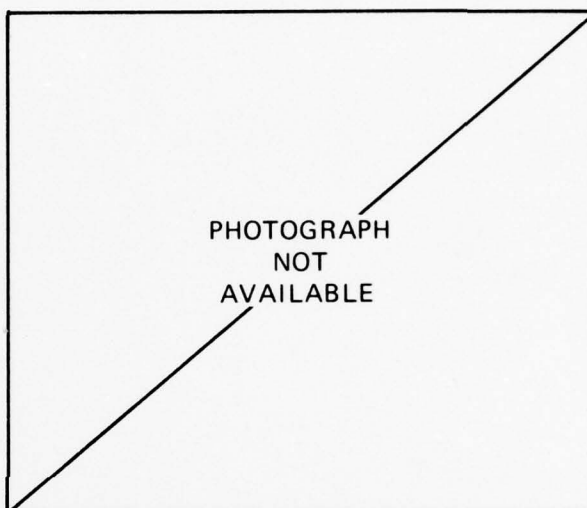
FIGURE 2.6 100-T TNT, PRE-DICE THROW II-1  
(photos courtesy of A. D. Thornbrough,  
Sandia Labs)



← 200 m →

(g) 30 SECONDS

FIGURE 2.7 100-T ANFO, CANADIAN 1969  
(photos courtesy of J. S. Watson,  
DRES, Canada)



← 200 m →

(h) 40 SECONDS

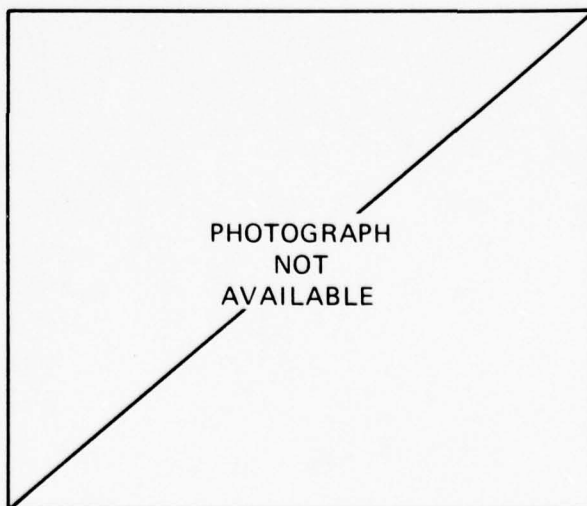
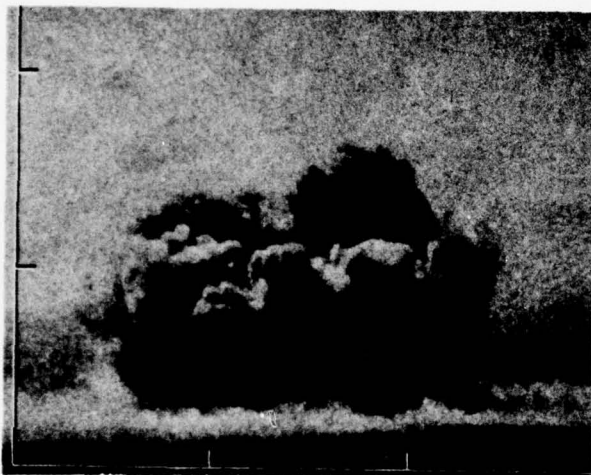




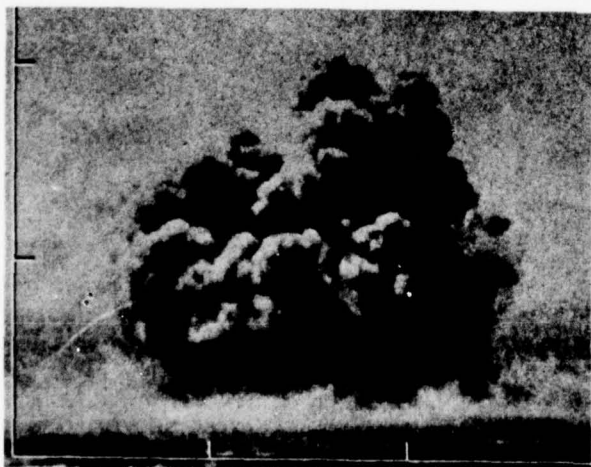
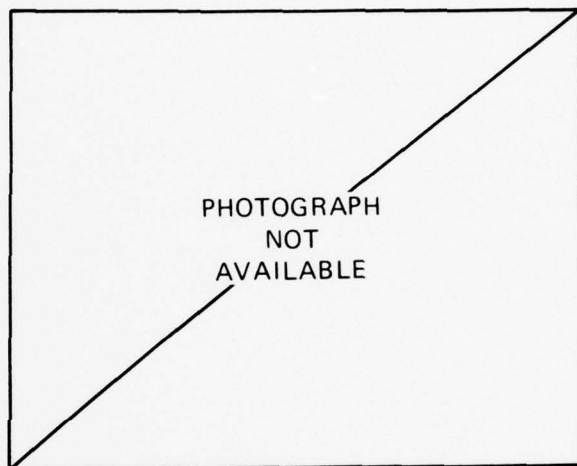
FIGURE 2.8 120-T ANFO, PRE-DICE THROW II-2  
(photos courtesy of A. D. Thornbrough,  
Sandia Labs)



← 200 m →

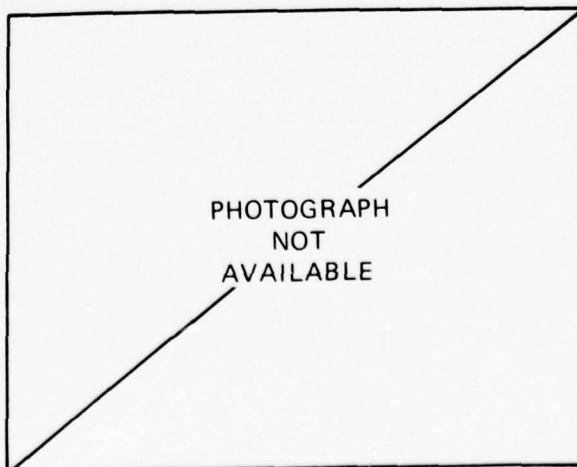
(g) 30 SECONDS

FIGURE 2.9 1.2-kT NUCLEAR AT -17 ft,  
BUSTER JANGLE: UNCLE, 1951  
(photos courtesy of W. Dudziak,  
Information Sciences, Inc.)



← 200 m →

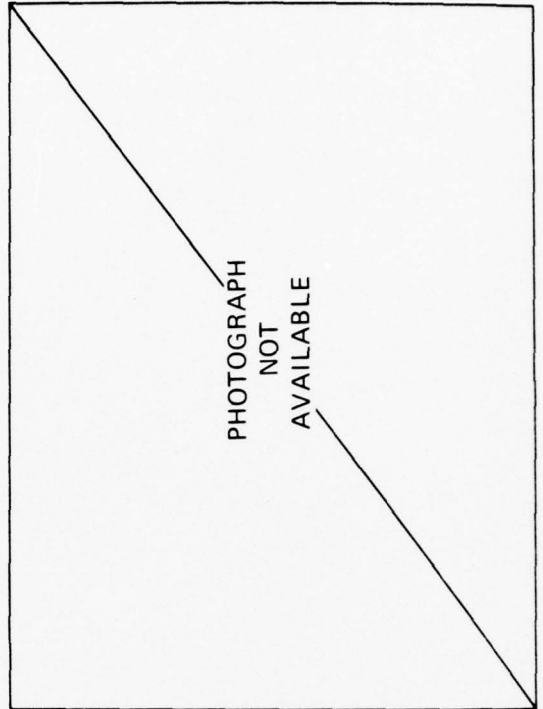
(h) 40 SECONDS



(a) CANADIAN "SNOWBALL," 1964 (photos courtesy of J. S. Watson, DRES, Canada)



(b) MIXED COMPANY III, 1972 (photos from DNA Documentary Motion Picture)



PHOTOGRAPH  
NOT  
AVAILABLE



FIGURE 2.12 COMPARISON OF THE DIFFERENT CHARGE CONFIGURATIONS OF 500 T, TNT



FIGURE 2.13 PHOTOGRAPHS OF MIXED COMPANY III AT LATE TIMES (TNT 500-T tangent sphere)  
(from DNA Documentary Motion Picture)

performed by the AFWL and presented in Section 3 for a tangent sphere and a hemispherically capped cylinder demonstrate, when compared, very different flow field characteristics in the ground zero region that seem quite consistent with these photographic results. We conclude that the DICE THROW cloud will not look much like previous TNT detonations that used spherical and hemispherical geometries.

Figures 2.9 through 2.11 present a time series of photographs of three nuclear detonations at depths of 17 ft and 2 ft, and also at a height of 4 ft above the surface.\* Not surprisingly, the generic characteristics of the dust clouds change very much with the changes in detonation position with respect to the ground surface.

We believe that the PDT II-2 explosion represents the best scale model for the effects that we should observe following DICE THROW. The photographic comparisons of Figure 2.8 with Figures 2.9 through 2.11 lead us to suggest that the DICE THROW cloud geometry will be more like that of a slightly buried nuclear charge--a charge that was buried more than 2 ft (for the yields involved) but perhaps not as deep as 17 ft.

The other surprising result that we derive from these photographic comparisons is that the fireball geometries and dust cloud behaviors following HE detonations are very dependent on the geometry of the HE charge. For example, Figure 2.7 presents cloud evolution following a hemispherically shaped ANFO charge detonation. By 6 s (the latest time photograph that was available to us), a very intensely convecting, rapidly rising fireball was observed. The tangent sphere detonation of Figure 2.6 does not produce such an intensely convecting fireball by 8 s even though it eventually will produce (after our last frame) a "classical"

---

\* The nuclear photographs were graciously provided by Dr. Walter Dudziak, of Information Science, Inc., Santa Barbara, California.



late-time cloud with stem. The hemispherically capped cylinder produced practically no vorticity--as inferred by the photographic behavior of the dust cloud.

Figure 2.12 presents a comparison of dust clouds following TNT detonations of equal yield but different charge configuration--a hemisphere and a tangent sphere. Thus, here geometry differences were produced by charge geometry, not by charge type. We may compare Figure 2.12(a) with Figure 2.7 to see the effect of the same comparative geometries but different charge materials (and yields). As with Figures 2.6 and 2.7, these photographs show that the 500-ton TNT hemisphere (SNOWBALL) detonation produced a much more pronounced vortex ring that rose at a more rapid rate than did the fireball produced by the 500-ton TNT tangent sphere (MIXED COMPANY) detonation. These four sets of figures [Figures 2.6, 2.7, 2.12(a), and 2.12(b)] add support for, but do not prove, the hypothesis that charge shape, not charge type, is most important in generating the generic features of HE fireballs and dust clouds.

On the basis of these photographic data, we anticipate that the DICE THROW dust cloud will not develop a rapidly rising and convecting vortex ring trailing behind it a narrow stem at late-time. We believe that the photographic comparisons show that an intense cloud of ejecta will characterize the early period (to 5 or 10 s) following DICE THROW. Results of AFWL calculations and Figure 2.8 suggest that no intense vortex ring will be formed so that the dust in the ejecta cloud will then rise slowly. As a result the rising winds will loft only the very small dust particles, with diameters less than a few millimeters. Had a hemispherical charge been used, an ejecta cloud would still form, but much of that dust and larger dirt particles would have been lofted by the rising fireball. Furthermore, it is our intuitive estimation that the more intense flow fields produced by a hemispherical geometry would better simulate the

intense afterwinds that are responsible in the atmospheric nuclear case for the pedestal and stem.

### 2.3 Measurements of Dimensions from PDT II-2 Photographs

In order to make estimates of microwave propagation phenomena to be produced by the DICE THROW experiment, it is necessary to have a model of the dust environment at all times following detonation. Ejecta cloud geometries are not currently estimated by theory; in fact, to our knowledge, no theory of dust deployment due to the rising ejecta exists. The AFWL calculations to be discussed in Section 3 use ejecta-spire dimensions based on measurements of ejecta geometries of earlier high explosive experiments.

We have made what we believe to be relevant measurements of PDT II-2 ejecta cloud geometry for use by the AFWL in preparing dust cloud densities to use in our propagation estimates. We have measured three quantities. These are height of ejecta spires, apparent angle of ejecta cloud edge, and internal angle of ejecta cloud (the ejecta cloud seems to have a hole in its center), all as a function of time.

Figure 2.14 presents averaged measurements of ejecta height versus time, from detonation to 10 s. At later times the photographs show that the cloud "boils" upward in a rather amorphous manner. Though not used in our planning estimates, these data are also included in Figure 2.14.

The ejecta seem to be emitted from the crater within a narrow band of elevation angles. However, dust from the lower portion of the spires seems to expand turbulently outward so that the edge of the ejecta-produced dust cloud is oriented at a steeper elevation angle than the angle of flight of original ejecta material.

Table 2.2 presents dimensions measured from photographs of the PDT II-2 detonation taken from the ground. The "inner" ejecta angle

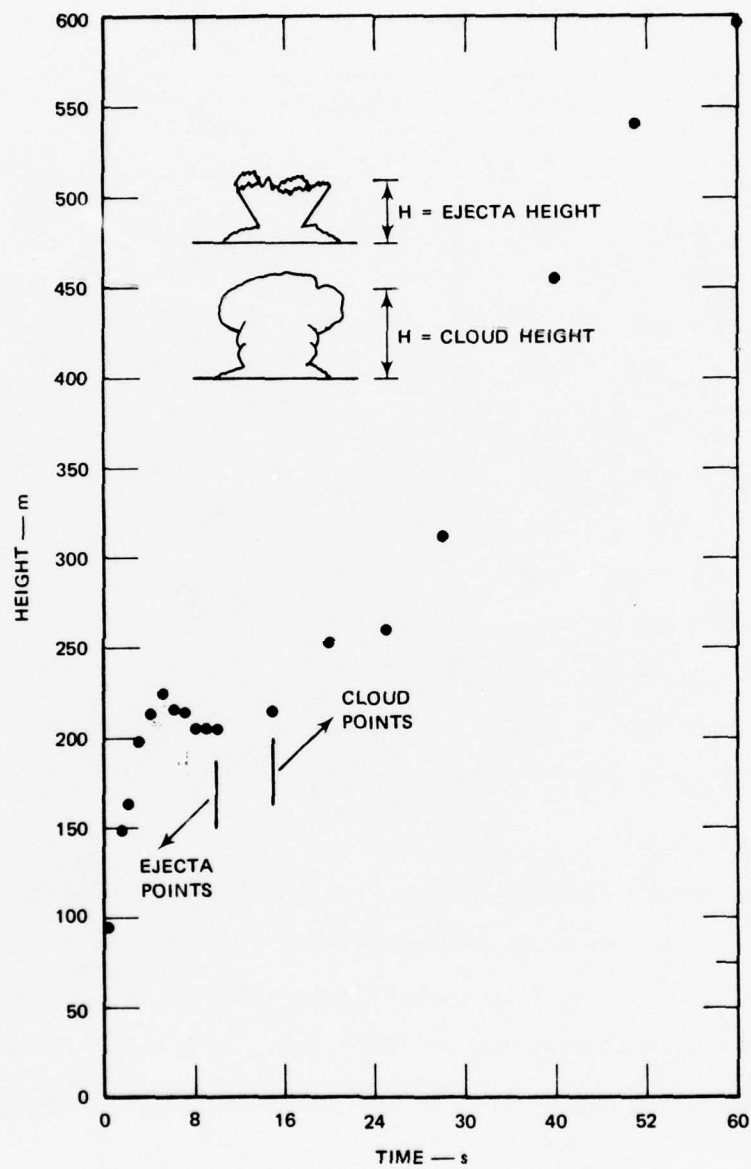


FIGURE 2.14 MEASURED EJECTA AND CLOUD HEIGHT vs TIME FOR PDT II-2

Table 2.2

MEASUREMENTS OF VARIOUS QUANTITIES AS A FUNCTION  
OF TIME FROM PDT II-2 PHOTOGRAPHS

Time (s)	Average Ejecta Angles		Outer Base Radius (m)
	Inner (deg)	Outer (deg)	
0.333	79	46	39
0.500	70	52	46
0.667	76	47	52
0.833	57	41	52
1.00	71	54	62
1.167	62	53.5	59
1.333	59	56	65
1.500	66	42	52
1.667	60	50.2	62
1.833	65	54	68
2.000	62.7	54	65

was a very subjective interpretation. On the basis of photographs of the detonation taken from an aircraft flying overhead, we have chosen for our later modeling work an inner ejecta angle of  $75^\circ$ , more appropriate to the early time values of Table 2.2. For an outer ejecta angle we use  $50^\circ$  elevation angle for our DICE THROW estimates.

#### 2.4 Summary

In this section we have described, as we understand it, the generic dust phenomena produced by surface HE and nuclear detonations. From comparison of HE and nuclear photographs, we are of the opinion that

the general dust-cloud morphology following DICE THROW will best simulate that to be expected following a slightly buried nuclear detonation. We have also discovered that the overall dust cloud morphology is very dependent on HE charge shape. We have not resolved whether the nature of the HE charge (ANFO or TNT) plays a significant role in the overall cloud morphology.

The PDT II-2 photographs have been measured to give us a guide for providing the AFWL with a dust ejecta geometry and initial velocity for use by them in the DUSTY code (see Section 3.3).

We conclude in Section 4 that we cannot use photographs for reliable estimates of dust densities or particle size distributions. Thus, we cannot draw conclusions from the photographs presented here as to the total amount of dust, or dust densities, to use in our propagation estimates.



### 3. THEORETICAL PREDICTIONS OF THE DICE THROW DUST ENVIRONMENT

The estimation of the effects of dust on microwave propagation requires knowledge of the spatial and temporal distribution of the dust. In our work we shall assume that, for practical purposes, the dust particles are sufficiently small that, in forward scatter, they are in the Rayleigh regime. Arguments on this point are presented in Section 4. If this assumption is used, then the microwave phase perturbation effects depend only on the mass density of the lofted dust. For a number of years the AFWL has been a leader in the research in this latter area. Furthermore, they have been taking a leading role in the estimation of blast-wave conditions for the 600-ton ANFO DICE THROW experiment. We have used their results, presented in terms of dust density concentration, for making preliminary estimates of phase effects on microwave signals. In this section we present a brief summary of their techniques as they pertain to our needs. Though the AFWL has a large number of computational codes that might be used in estimating effects, we restrict our attention to those they used in the estimates received by us.

The AFWL employs three steps to obtain the information we need for propagation estimates. First, they compute the propagation and intensification of the detonation wave as it moves through the high explosive. When the calculation shows that the wave reaches the surface of the explosive this calculation is stopped. The results are then used as input to the second stage of the calculation, which is AFWL's two-dimensional hydrodynamic code HULL. This code follows the shock wave, fireball, and air motion produced by the detonation. The third step in their determination of dust loading is performed by a code called DUSTY.

This code takes the HULL-computed hydrodynamic flow fields and a chosen initial distribution of dust, and then computes the effects of gravity and air drag on the dust distribution as time proceeds.

In this section we discuss these various procedures and display computational results that bear upon the prediction and interpretation of the DICE THROW microwave experiment.

### 3.1 High Explosive Burn

The first step in the AFWL calculations is to establish the initial shock conditions at the surface of the explosion following high explosive burn. For spherically symmetric TNT detonations, the AFWL uses an analytic solution using the LSZK equation of state for the TNT.\* The high explosive burning of the hemispherically capped cylinder of ANFO is performed by HULL using the JWL equation of state. We are informed that the validity of these techniques can be checked against known results using the SAP code, which is a one-dimensional Lagrangian hydrodynamic code. The final conditions of shock intensity, temperature and density distributions are then available as initial conditions in HULL.

### 3.2 Flow-Field Calculations in the Atmosphere

The HULL code is a one-fluid, two-dimensional Eulerian, finite-difference hydrodynamic code that computes and displays the flow fields in the air outside the explosive charge. The HULL code simultaneously solves the equation of state of air and the equations governing conservation of mass, momentum, and kinetic energy. HULL solves these equations by dividing the region occupied by the fluid--in this case, air--into a

---

\* Dr. Charles Needham of the AFWL should be consulted for an in-depth discussion of these techniques.

mesh of cells in the R-Z plane (cylindrical symmetry). Mesh size can be made to vary in a number of ways to optimize accuracy in regions of particular interest. The computer time, and thereby cost, for HULL runs depends on the number of mesh points used in the calculations.

The flow calculations that the AFWL has used in estimates of dust distribution to be shown later were originally performed with the mesh chosen to include and well-represent the shock wave at all times. To keep costs within reasonable limits, the number of mesh points was restricted, thereby leading to only a "coarse" representation of the region near the detonation center at late times. For example, the mesh size near the origin at 15 s is on the order of  $50 \times 40$  m; at 60 s it has expanded to over  $100 \times 100$  m. This means that at 60 s the 300-by-300-m region around the detonation point, of greatest interest in our microwave estimates, is represented by only nine mesh cells.

Examples of the HULL output for the DICE THROW shot are reproduced in Figures 3.1 and 3.2; the corresponding flow fields for a 500-ton TNT tangent sphere are also shown. The two sets of results are presented to show the very different nature of the computed flow fields produced by an ANFO cylinder and a TNT tangent sphere. Velocity vectors are represented by arrows, the lengths of which are proportional to the logarithm of the fluid velocity. The maximum velocity anywhere within the calculational grid is given. This velocity is found to change with time, and increases, for the TNT sphere, reaching a maximum at several tens of seconds.

Several important differences in the flow conditions are evident in the two figures: First, the maximum velocities attained for TNT are significantly greater than for ANFO--in fact, by more than an order of magnitude at 15 s; second, the sizes of the major vortices are quite different; and finally, at 7 s there is an updraft over the detonation

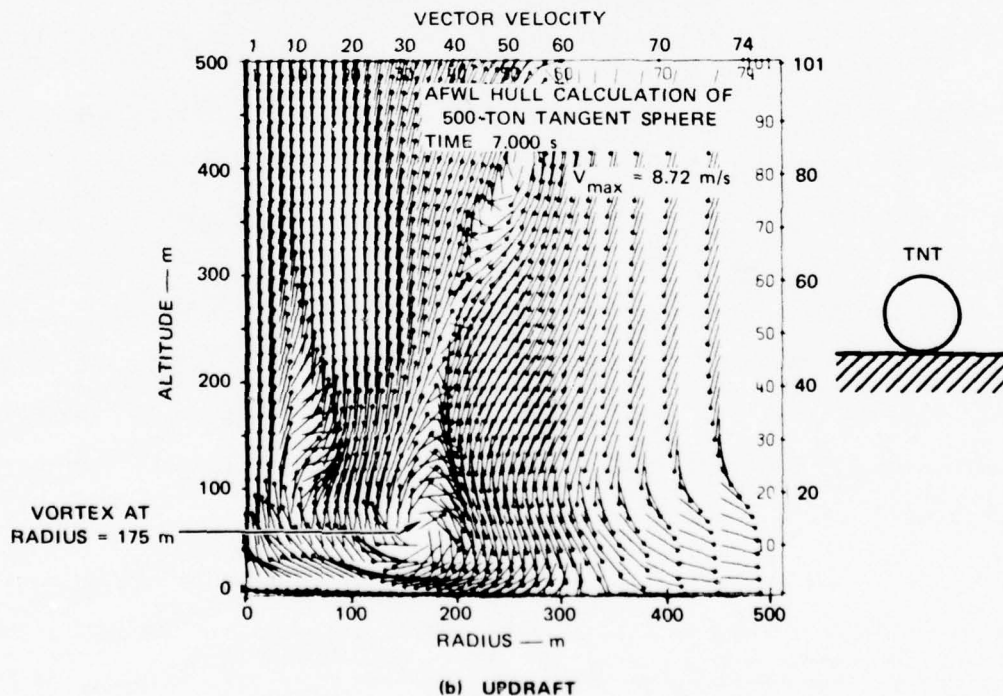
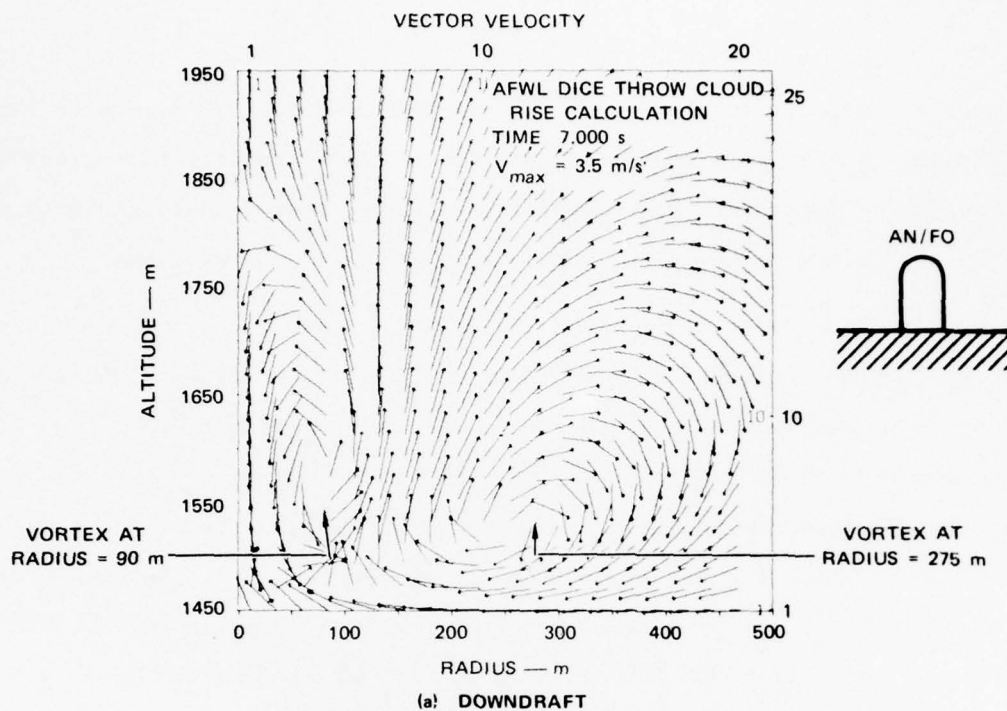


FIGURE 3.1 AFWL FLOW-FIELD CALCULATIONS FOR DICE THROW AND 500-T TNT TANGENT SPHERE AT 7 SECONDS. Arrow lengths are proportional to the logarithm of air velocity.



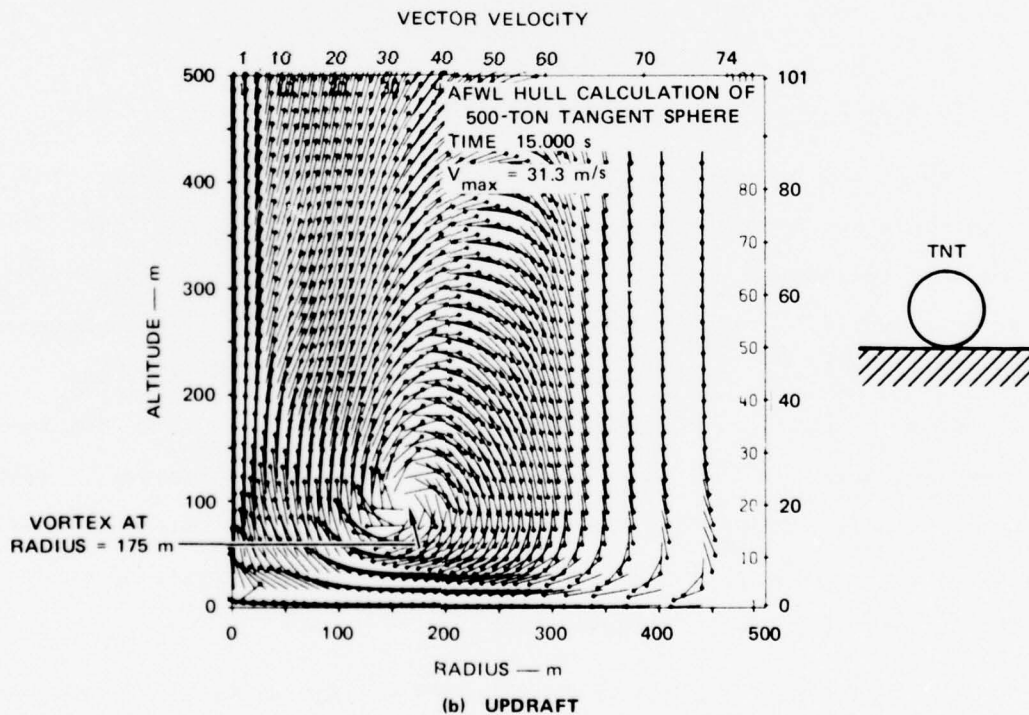
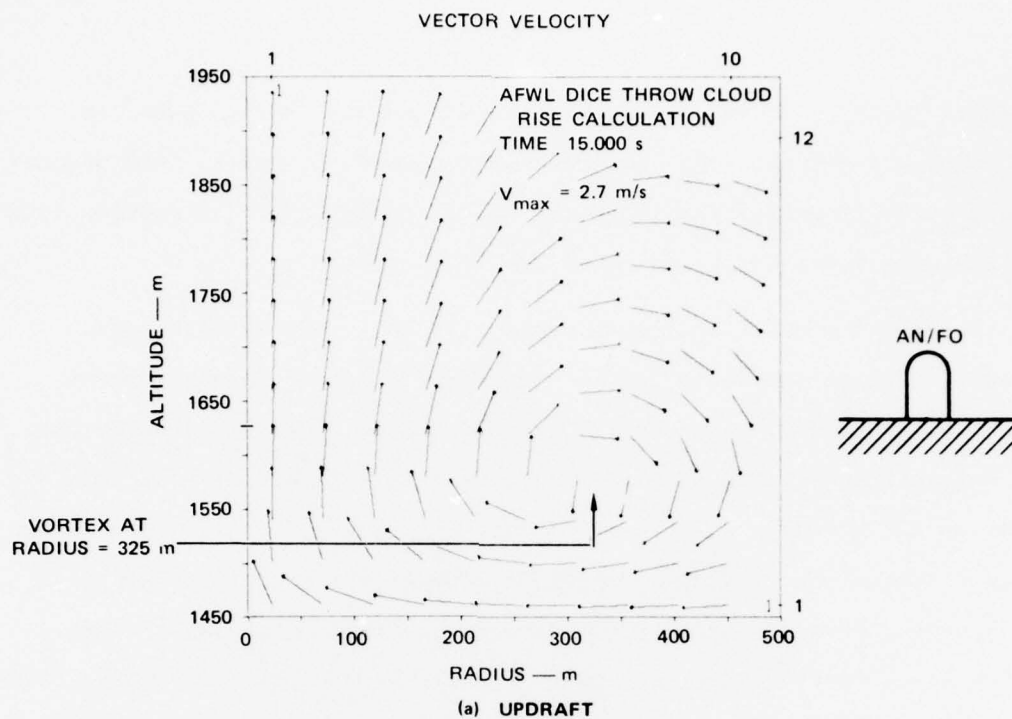


FIGURE 3.2 AFWL FLOW FIELD CALCULATIONS FOR DICE THROW AND 500-T TNT TANGENT SPHERE AT 15 SECONDS. Arrow lengths are proportional to the logarithm of air velocity.



point in the case of TNT, while a downdraft exists for the ANFO case (a "reverse" vortex). The "reverse" vortex produced by the ANFO detonation changes direction and is in the "classically proper" direction (that is, the same direction as computed for TNT) by 10 s.

By 15 s the maximum flow velocity will be in the central region corresponding to the "stem" of the "classical" late-time environment (see Section 2.1.4). The updraft velocity of 31.3 m/s produced by the TNT detonations will be much more effective in lofting material than will the 2.7 m/s maximum velocity produced by the ANFO cylinder. On the basis of these calculations, one might expect very different late-time dust environments produced by these two different geometries of high explosives. Despite the large mesh size in the region of interest, these differences tend to be verified by the photographs we presented in Section 2.2.

### 3.3 Calculation of Dust Density Distribution

The calculation of the distribution of dust as a function of time is accomplished by the AFWL through use of a code named DUSTY. The code uses the atmospheric flow fields precomputed by HULL as a driving field for dust particles. Dust particles are introduced by an ad hoc procedure and are then treated as a "passive additive," meaning that the dust particles are blown by the HULL winds (as well as falling under the influence of gravity), but they do not affect the HULL flow fields. Interactive calculations whereby the dust can affect the flow fields by mass loading are also possible with HULL/DUSTY, but at the expense of an order of magnitude increase in computer time.

The following five parameters are used as inputs for DUSTY code runs:

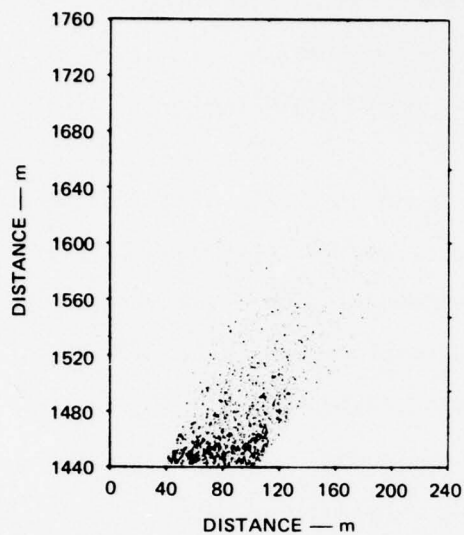
- (1) Total amount of dirt injected.
- (2) Particle size distribution and intrinsic density.

- (3) Inner and outer radii from ground zero from which particles come (assumed to come from an annulus).
- (4) Maximum and minimum ejection velocities.
- (5) Maximum and minimum angles of particle initial trajectories.

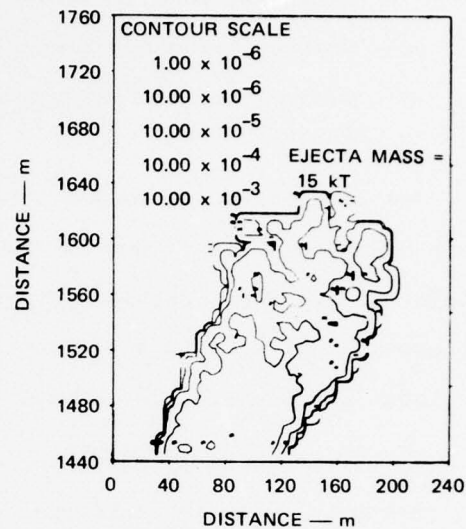
The parameters are chosen partially on the basis of crater measurements or expectations (Item 1) and photographs of previous HE tests (Items 3, 4, and 5), partially on measurement of particle sizes from shovels full of soil in the expected detonation area (Item 2), and partially on intuitive guesses as to what might actually occur.

A finite number of particles are chosen (in practice, between 2000 and 10,000), and their individual characteristics are determined by Monte Carlo means within the limits established in Items 2 through 5 above. The expectation distributions are uniform for Items 3 through 5. Particles move as in a vacuum, under the influence of gravity only, from their start time to one second. The particle start times are equally spaced between 0.05 s and 1.0 s. At one second they are then placed in the precomputed HULL flow field where suddenly air drag is introduced in addition to gravity. The drag formula considers the particles to be spherical. The DUSTY code keeps track of all particles as they fall under gravity and are blown by HULL winds.

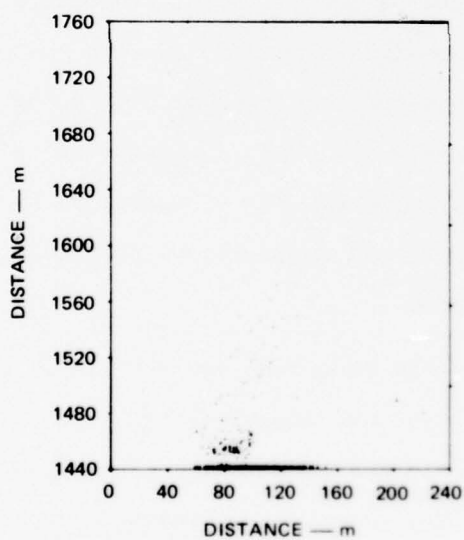
The results of the DUSTY code outputs have been made available to us by the AFWL in three formats. We have been supplied with printouts from which we can draw numbers for use in our propagation calculations. The two other formats are graphical. Representative results in these graphical forms are presented in Figure 3.3. They illustrate the qualitative and quantitative behavior of the AFWL-DUSTY computations. We display their results at the time of initial injection (1 s) and at 30 s afterwards. The initial conditions for these particular calculations were as follows: Injection elevation angles were between  $50^{\circ}$  and  $75^{\circ}$ ,



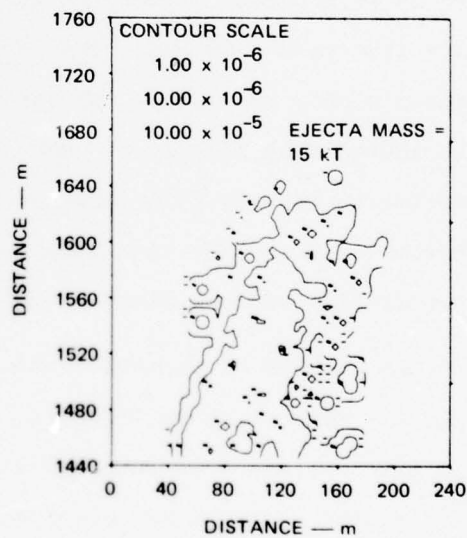
(a) PARTICLE DISTRIBUTION  
AT 1 s



(b) DUST DENSITY CONTOUR  
AT 1 s



(c) PARTICLE DISTRIBUTION  
AT 30 s



(d) DUST DENSITY CONTOUR  
AT 30 s

FIGURE 3.3 EXAMPLE OF PARTICLE POSITION PLOTS AND DUST DENSITY CONTOURS  
FOR DICE THROW

initial radii were between 39 and 106 m, and initial velocities were between 10 and 220 m/s. Each dot on the particle distribution figures [Figures 3.3(a) and (c)] represents the position of one of 2000 particles injected into the flow fields calculated by the AFWL/HULL program. In Figure 3.3(c) the heavy concentration of particles along the surface between 60 and 150 m illustrates those particles that have fallen back to the earth's surface. Each particle has an assigned value of mass. The total mass of particles within a given computational cell is converted into mass loading density. The mass loading density is then plotted; examples of these density plots at 1 and 30 s are also presented as Figures 3.3(b) and (d).

The only source of dust used by the AFWL in their DICE THROW prediction was debris from the crater. All of this material was deployed during the first second. The ejecta spires from PDT II-2 continued their upward rise for approximately 3 s. Employing the traditional cube-root-of-yield scaling, we anticipate that the DICE THROW ejecta cloud will take 5 s to become fully deployed. In order to accommodate this longer deployment interval and yet approximately simulate the AFWL deployment scheme for our early-time estimates, we have developed the following analytical expression for dust density as a function of location and time.\*

$$\rho[r, S_{\max}(t)] = \frac{M_T}{2\pi S_{\max}(t)} \frac{\ln \left[ \frac{S_{\max}}{r - r_o} \right]}{r^2 (\varphi_0 - \varphi_1)} \cdot \frac{1}{\sin \varphi} \quad (3-1)$$

Figure 3.4 helps define terms.  $M_T$  is the total mass of dirt assigned to the ejecta;  $S_{\max}(t)$  is the maximum slant range from the ground to the

---

\* The expression is derived in Appendix A.

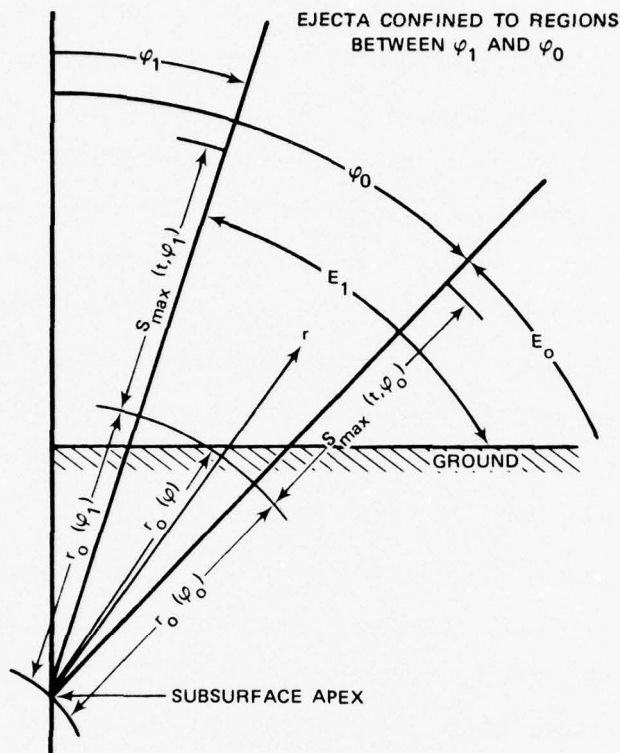


FIGURE 3.4 GEOMETRY USED IN ANALYTICAL SIMULATION OF AFWL EJECTA-INJECTION TECHNIQUE

tip of the ejecta at a particular time  $t$ ;  $r$  is the range from the sub-surface (below ground) apex used as the pseudo-center for ejecta emission, and  $r_0$  is the distance from this apex to some average point on the ground. For advance predictions the quantity  $S_{\max}(t)$  is taken to be the measured slant range to the ejecta tips for the 120-ton ANFO PDT II-2, scaled up by a factor of  $(5)^{1/3}$  in time and range in anticipation of the 600-ton DICE THROW ANFO detonation. The quantity  $r$  is allowed to vary between  $r_0$  and  $[r_0 + S_{\max}(t)]$ . For our propagation calculations, the dust density at a constant propagation height,  $h$ , over the ground is simulated by evaluating Eq. (3-1) with  $r = r_0 + h$ .

Figure 3.5 presents a comparison of the DUSTY density at one second along a  $60^\circ$  elevation with our analytical procedure expressed by Eq. (3-1).



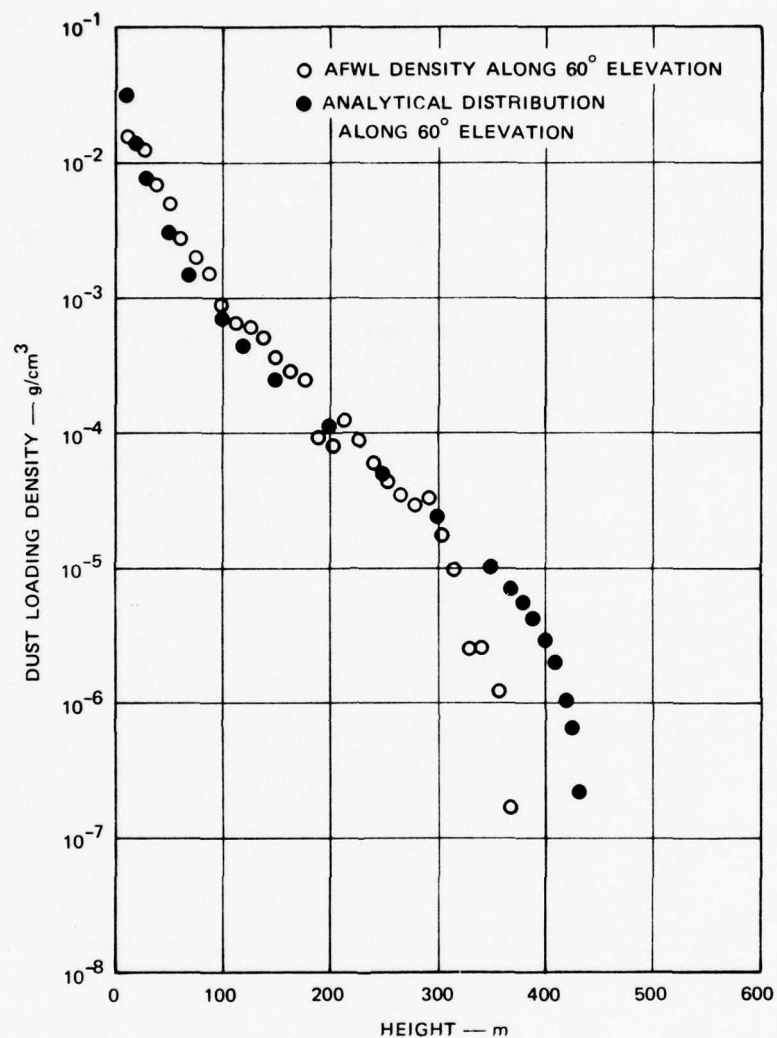


FIGURE 3.5 COMPARISON OF AFWL DUSTY AND ANALYTIC DENSITY DISTRIBUTION ALONG 60° ELEVATION

For this comparison,  $\varphi_1$  was  $0^\circ$  ( $E_1 = 90^\circ$ ) and  $\varphi_0$  was  $60^\circ$  ( $E_0 = 30^\circ$ ). The comparisons seem adequate except at the very highest altitude.

#### 3.4 Examples of Dust Density Calculations for Early-Time Ejecta

In this subsection we present early-time estimates of the integrated dust density through the ejecta cloud for several propagation paths to

be probed during DICE THROW. Most propagation effects depend on this integral. The estimates presented here are derived using our analytical ejecta model.

Figure 3.6 shows the expected height of the DICE THROW ejecta spires as a function of time. These values are based on our measurements of

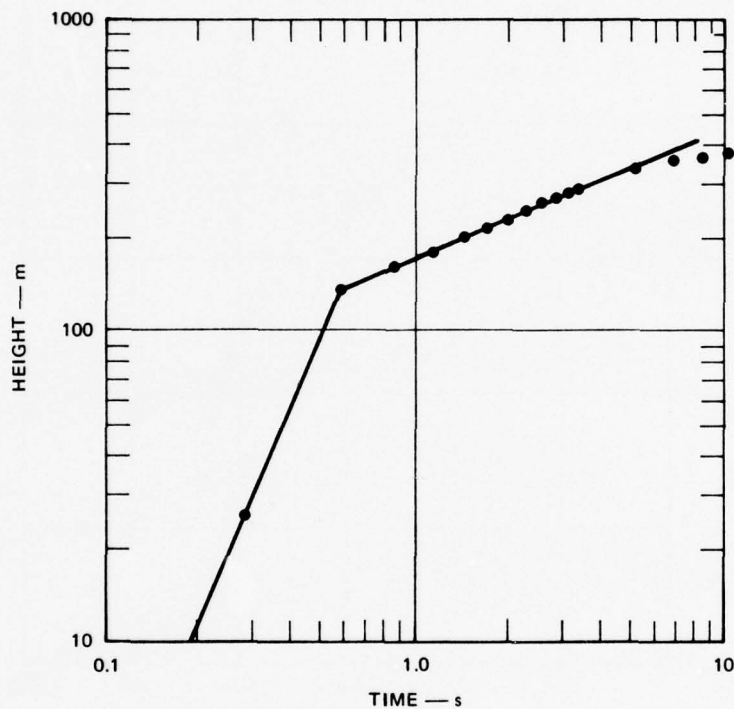


FIGURE 3.6 EXPECTED HEIGHT vs TIME OF DICE THROW EJECTA (time and distances cube-root scaled from PDT II-2)

the height of the PDT II-2 ejecta spires, scaled up using the  $(5)^{1/3}$  yield scaling law for linear dimensions and time. For ease of computation we have drawn straight lines through the data points, and we compute dust densities according to these time lines.

The integral of dust density along three of six propagation paths as computed by the analytical procedure is presented in Figure 3.7. The

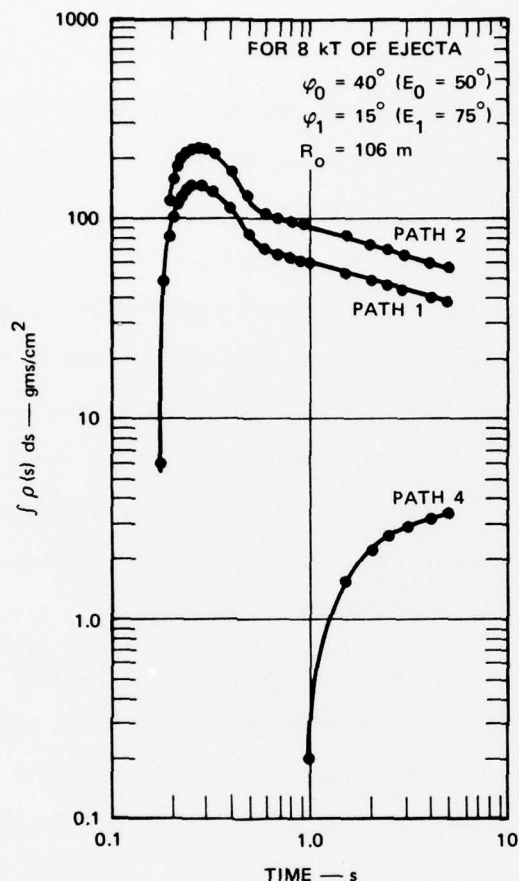


FIGURE 3.7 INTEGRATED DUST DENSITY ALONG THREE PROPAGATION PATHS USING ANALYTICAL EJECTA PROCEDURE

total mass deployed was 8 kT. Ejecta originated from within a radius of 106 m of ground zero and were confined between elevation angles of  $50^\circ$ . Details concerning these three propagation paths are given in Section 4.2; briefly the paths probe the cloud at 10 m directly above ground zero (Path 1), 10 m above the ground and 40 m to the right of ground zero (Path 2), and at an altitude of 190 m directly over ground zero (Path 4).

In our model, the early time behavior of Paths 1 and 2 results from the intersection of those lines of sight at about 0.2 s by the leading edge of the rising debris. The subsequent decrease in integrated dust

density with time results from the geometric spreading of the dust in the rising spires.

The onset of occultation of the upper path at one second corresponds, as before, to the time of flight of the spires to the 190 m level of this path. Here the density does not start to decrease during the first 5 s because the geometric spreading of dust as it reaches this high path is very slow compared with the influx of higher density material from lower altitude. Inasmuch as our analytical model is based on an artificial ejection scheme rather than on real physical processes, it will be rather surprising if the actual phase measurements show this temporal behavior. Furthermore, we have included in our estimates only dust in the ejecta cloud. The magnitude of the error introduced by neglecting dust in the surface surge and sweep-up cloud is not known.

Later time estimates of the integral of the dust density along propagation paths are accomplished by reading data from the AFWL supplied DUSTY printout into our own computers that then numerically integrates along the various propagation paths. Unfortunately, this integral from DUSTY data is not available for display here, but equivalent comparisons between DUSTY and our analytical procedure are presented in Section 4.3.

#### 4. MICROWAVE PROPAGATION AND PREDICTIONS FOR DICE THROW

In this section we study several effects on microwave propagation that will be produced by the DICE THROW 600-ton ANFO high explosive detonation. An experiment is planned that will quantitatively measure the phenomena that we discuss. Though we do attempt predictions of phase shifts and attenuations expected due to the ejecta on the basis of ejecta models pieced together by AFWL and ourselves, we are of the growing opinion that not enough is currently known to make accurate predictions. In fact, the greatest value of the microwave experiment may be its ability to diagnose dust density integrated through the ejecta, ground surge, and pedestal regions.

We also discuss several other phenomena that may be important but that have not yet been subjected to quantitative estimation in terms of the DICE THROW experiment. For background, we briefly describe the experimental parameters of the microwave experiment. We then describe the various phenomena and the theory used to estimate anticipated effects. Finally, we present some quantitative estimates of phase and attenuation based on four ejecta models.

##### 4.1 Description of Microwave Propagation Experiment

The microwave propagation experiment to be performed during the DICE THROW experiment involves transmitting phase-stable microwave signals through various parts of the dust cloud. The paths that will be probed are not necessarily optimum from a conceptual point of view. This is because the geography of the detonation area and the equipment associated with other experiments place rather severe constraints on the location of our transmitting and receiving sites.



Figure 4.1 presents a plan view of the experimental geometry. The drawing is not to scale. There are two transmitting and three receiving sites, leading to six propagation paths, as indicated on the figure. Distances between various sites are indicated in either meters (receiver separation) or kilometers (all other distances). The main transmitter is located as close to the ground zero as is practicable in order to keep Fresnel zones as small as feasible. Its raypaths pass about 10 m above the ground near ground zero. The second transmitter site is located on top of North Oscuro peak. This transmitter site leads to paths that probe higher regions of the dust cloud (190 m altitude). The prime receiver (receiver number 1), ground zero, the main transmitter, and the transmitter on North Oscuro peak have all been carefully aligned.

Figure 4.2 is an elevation view (not drawn to scale) of the intersection of the six propagation paths with the normal plane at ground zero. The figure also lists the frequencies to be used along each path. The transmitter signals are all generated from a common local oscillator, thereby leading to frequency/phase coherent measurement capability. The 424-MHz signal along Paths 4, 5, and 6 is time shared between the three receiver sites with percentage dwell times indicated in the figure. The cycle time through the three receivers is two seconds.

The phase and amplitude of each signal will be recorded for later interpretation. Phase variations, measured with an accuracy on the order of  $1^\circ$  to  $3^\circ$ , are expected to provide an indication of the integrated change in dielectric properties along the propagation path. Signal extinction due to particulate scattering may also be observed.

The DICE THROW site geometry, as we presently understand it, is shown in Figure 4.3. An important feature is the large area that has been excavated around the detonation point and then refilled with blow sand. The "fill" area was constructed to prevent the production of large

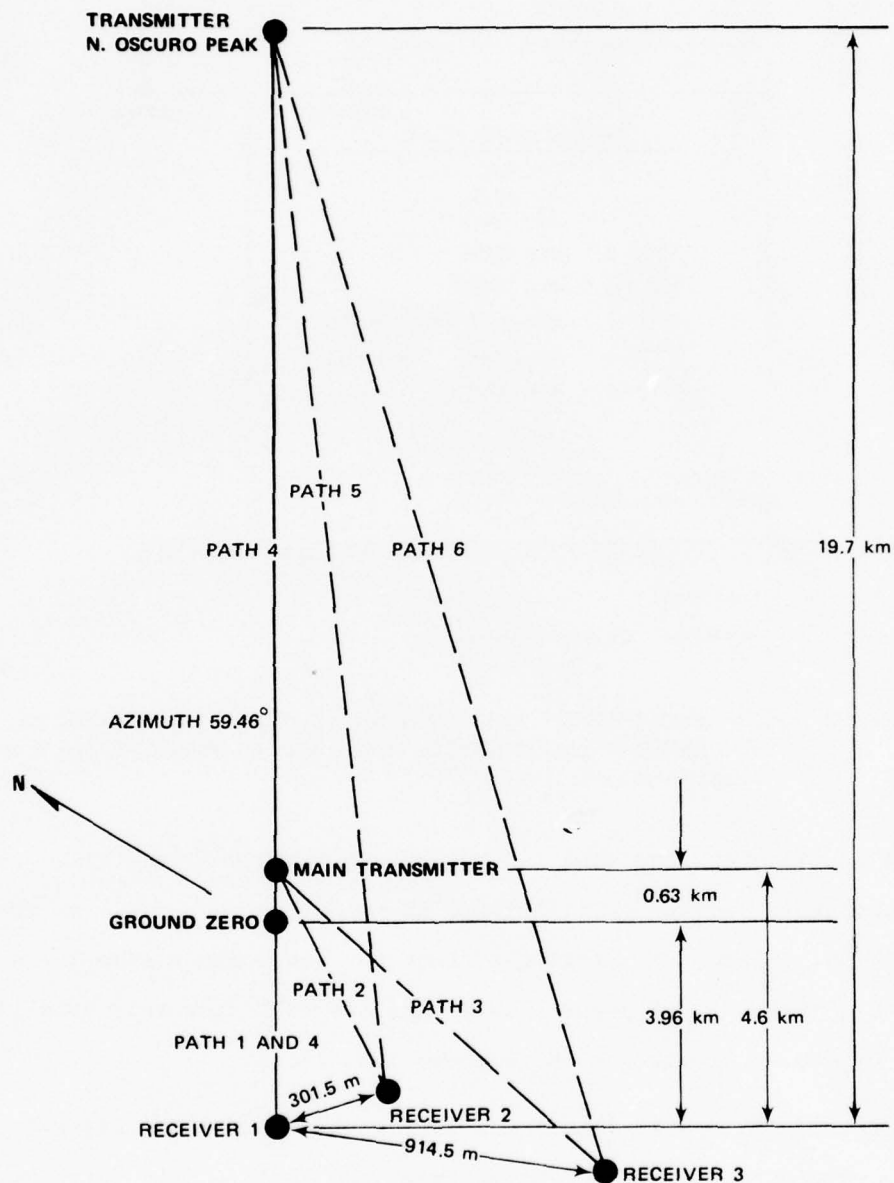


FIGURE 4.1 PLAN VIEW OF DICE THROW MICROWAVE TRANSMISSION EXPERIMENT  
(not drawn to scale)

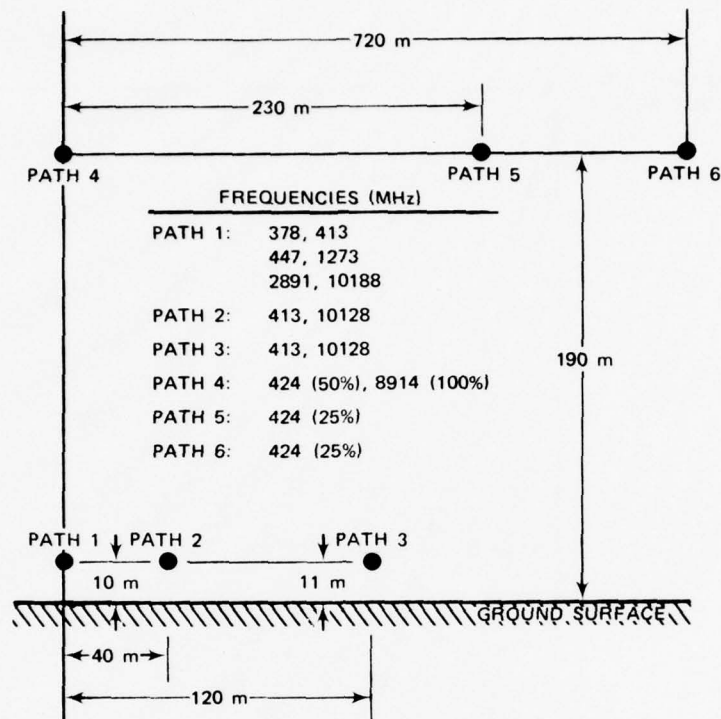


FIGURE 4.2 ELEVATION VIEW OF LINES-OF-SIGHT IN PLANE OF GROUND ZERO, AND FREQUENCIES EMPLOYED. Dwell times for Paths 4, 5, and 6 are indicated in percent.

missile ejecta. We have been led to believe that the fine "fill" sand is well represented by the particle size distribution used in later computations. (As will be seen, that distribution does contain some large particles, though.) It seems likely that the fill sand will constitute the major source of all debris injected into the air.

A second feature in Figure 4.3 is the strongly bonded layer of caliche occurring at depths ranging from 5 to 10 ft. This layer can influence the cratering process in that it may cause the crater to "bottom out." On the other hand, the layer may break up and thereby be a source of large pieces of ejecta.

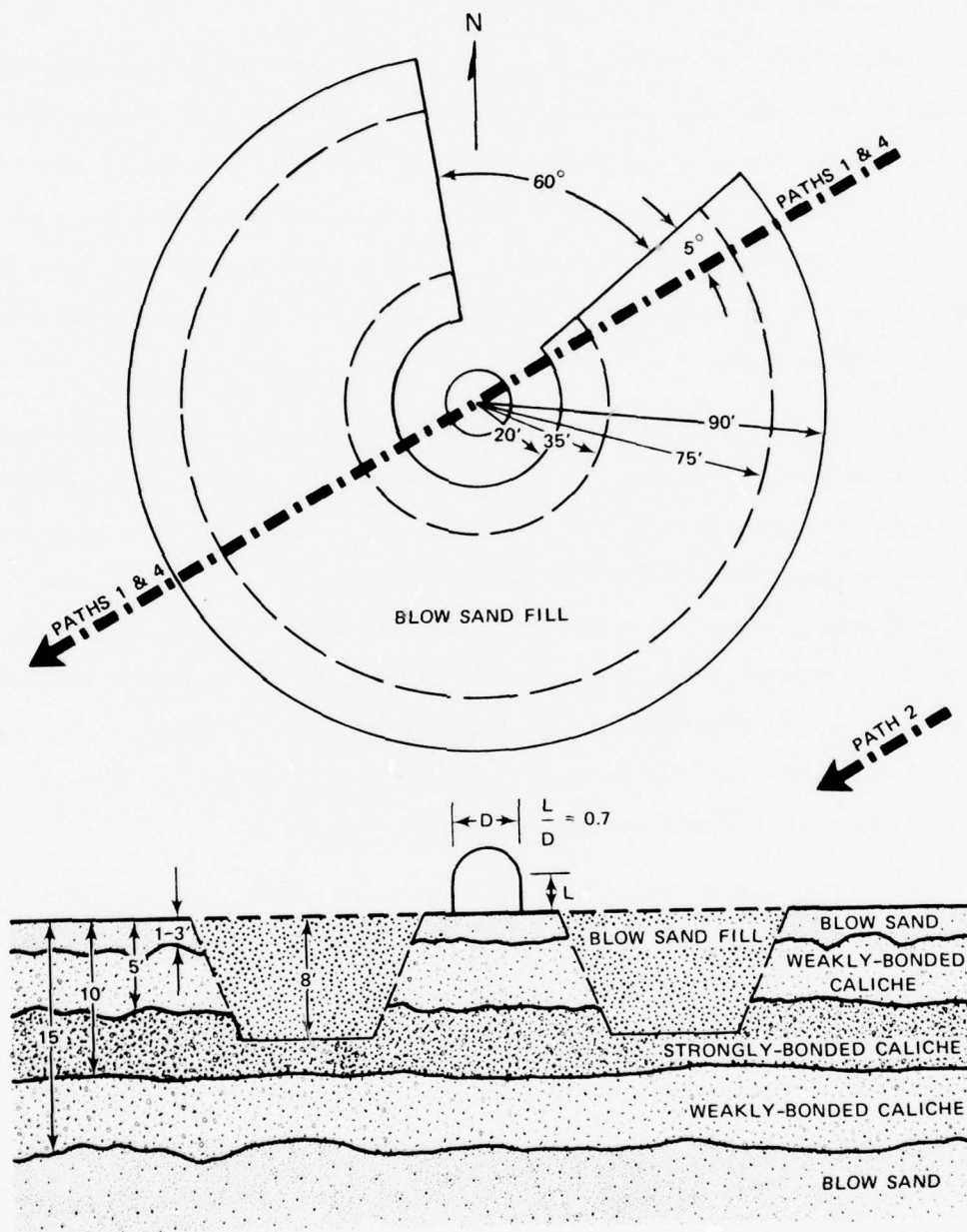


FIGURE 4.3 DICE THROW SITE GEOMETRY

#### 4.2 Description of Various Effects on Microwave Propagation Expected from the DICE THROW Detonation

A variety of effects may be observed that will be produced by the HE explosion. Probably the first observable effect will be passage of the shock wave through the line of sight. The time of arrival should correlate well with optical measurements of shock wave position. We have not attempted to estimate the phase and amplitude fluctuations produced by the shock wave. We expect a high degree of coherence associated with the phenomenon.

The hot air and detonation products in the "fireball" reduce the index of refraction compared with the ambient air. This reduction leads to diffraction phenomena and a phase advance. Estimates of these effects rely on accurate estimates of fireball temperatures. Since the mesh size in the fireball region from the HULL calculations provided by AFWL is too large for accurate prediction to be made, we have not included thermal effects in our calculations. The heated air region is sufficiently small that it might only affect paths directly over ground zero; these effects are expected to be small and of a transient nature.

The ejecta cloud containing dust particles increases the index of refraction above that of the ambient air. This increase leads to phase retardation. The ejecta cloud dimensions (and abrupt edge) may lead to diffraction effects. It is not feasible to compute expected two-dimensional diffraction patterns produced by the cloud; a one-dimensional example will be presented later for illustrative purposes. Though diffractive effects may affect communication system operation, our prime interest here is whether diffractive phenomena will affect the validity of the data interpretation based on slow phase and amplitude changes. Turbulent mixing of dust-laden and clean air will lead to phase fluctuations (and diffraction effects). There are no known techniques for



reliable theoretical predictions to be made of these effects. Indeed, the experimental measurements of these effects were part of the motivation for performing these experiments.

Refraction (ray bending) may be an important effect for high density dust regions. Estimates of the effect of ray bending are most pertinent in terms of validating the interpretation of the experiment results. In order to estimate these effects, one needs to know, accurately, the gradients in dielectric index. These cannot be well predicted in advance.

It is expected that the main effects to be observed will be slower phase and amplitude variations associated with the intersection of the overall dust cloud with the various lines of sight. These effects should depend on the average properties of the dust. Within the accuracy of prediction of the dust densities in the cloud, these effects on the microwave signals ought to be estimable. Or, reversing the procedure, the experiment is capable of measuring the properties of the dust environment as a function of time. For this reason, we have pursued the estimation of these effects on the basis of the ejecta/dust provided by the AFWL through the DUSTY code. We briefly outline here the theory of the interaction of the electromagnetic signals with the dust cloud in preparation for estimates to be made later.

#### 4.2.1 Phase Variations Produced by Dust

An electromagnetic wave interacting with a small dust particle induces a dipole moment in the particle. The displacement currents associated with this induced dipole lag the incident wave by nearly  $90^\circ$  (for a perfect dielectric). If the dielectric constant contains an imaginary part, then a real current (in-phase component) is also induced; this current leads to particle heating and energy extraction from the beam. The induced displacement (and real) currents also reradiate out

of phase with the incident wave. In the forward direction, these reradiated signals from all dust particles add coherently; the resulting wave adds coherently but out of phase with the incident wave leading to a phase retarded wave. From a macroscopic point of view, we say that therefore the medium has dielectric properties with an index of refraction that differs from that of a vacuum. Because the energy scattered in directions other than forward add incoherently (dust particle distribution is random), some energy is lost, not only by heating the particles, but by scattering. The total loss we call extinction. We study this scattering loss in the next subsection.

The total phase shift due to dust relative to the vacuum--or undisturbed air--is given as follows:

$$\varphi = \frac{2\pi}{\lambda} \int n(s) ds \quad (4-1)$$

where

$\lambda$  = Wavelength

$n(s)$  = Refractive index at position  $s$

$s$  = Raypath.

This equation should be integrated along the actual raypath. As a practical matter we ignore the (probably small) angular changes in the raypath as it proceeds through the dust cloud.

The refractive index of the dust-laden air is related to the properties of the dust particles through the Lorentz-Lorenz (Clausius-Mossetti) formula.

$$n(s) = 1 + \frac{3}{2} \frac{\rho_c(s)}{\rho_d} \left( \frac{\epsilon - 1}{\epsilon + 2} \right) \quad (4-2)$$

where

$\epsilon$  = Dielectric constant of dirt

$\rho_d$  = Particle density in  $\text{g/cm}^3$

$\rho_c(s)$  = Density of the dust cloud in  $\text{g/cm}^3$ .

This equation is valid if the particle sizes are small compared with a wavelength. As a practical matter, the particles probably act as "small particles" if their Rayleigh cross section in forward scatter is smaller than their geometric cross section. For 400 MHz, this criterion leads to requiring only particles with diameters less than 21  $\mu\text{m}$ , which is probably not very restrictive. The X-band, 10,000 MHz frequency leads to the restriction that the equation is valid only for particles with diameters less than about 0.85  $\mu\text{m}$ , which is clearly a more restrictive condition than that applied at 400 MHz. In view of the terminal velocity for this size particle, we expect that X-band measurements will not suffer in interpretation after 10 to 15 s. At earlier times there will be a greater uncertainty in interpretation. Because we are interested in RF change-of-phase relative to that of dust-free air\* we combine Eqs. (4-1) and (4-2) and also subtract the undisturbed path length to obtain the phase difference,  $\Delta\phi$ :

$$\Delta\phi = \frac{2\pi}{\lambda} \int [n(s) - 1] ds = \frac{2\pi}{\lambda} \frac{3}{2} \frac{\left(\frac{\epsilon - 1}{\epsilon + 2}\right)}{\rho_d} \int \rho_c(s) ds \quad (4-3)$$

From this equation it can be seen that the length of the raypath in the cloud and the density of the dust cloud along the path are the determining factors.

In order to give an intuitive feeling of the magnitude of this dielectric phenomenon, we present in Figure 4.4 the effective increase

---

\* For convenience the index refraction of air is taken here to be 1.0

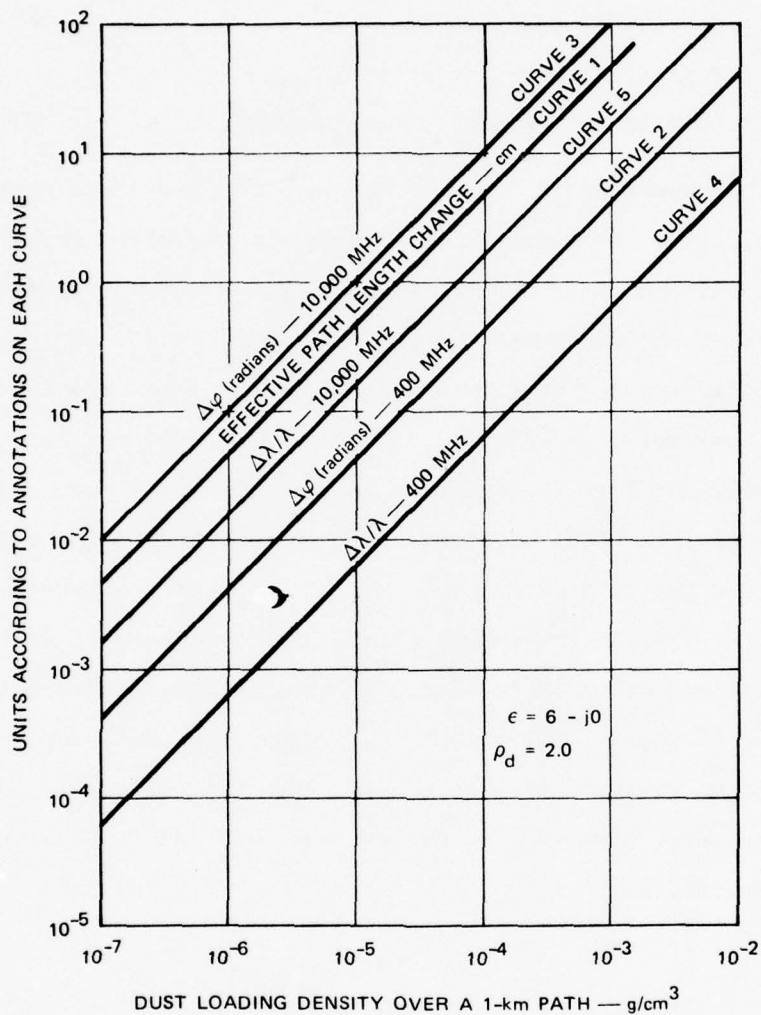


FIGURE 4.4 PHASE RETARDATION vs DUST DENSITY FOR A ONE-KILOMETER PATH OF UNIFORM DUST LOADING

in phase path length over a 1 km path for a uniform dust density. The data in this figure are presented in several ways. Curve 1 presents the effective increase in phase path length in centimeters. Curves 2 and 3 present the phase shift in radians for 400 MHz and 10,000 MHz, respectively. Curves 4 and 5 present the phase path change in terms of fraction of wavelength,  $\Delta\lambda/\lambda$ , at 400 MHz and 10,000 MHz respectively. With a resolution of  $2.5^\circ$  phase shift (approximately that of the X-band equipment to

to be used during DICE THROW), dust densities on the order of five times  $10^{-7}$  g/cm<sup>3</sup> over a 1-km path ought to be measurable.

#### 4.2.2 Attenuation (Extinction) by Dust Particles

As indicated earlier, the dust particles may extract energy from a microwave beam by at least two processes. These are scattering, and absorption through particle heating. We first discuss absorption due to heating.

A nonzero imaginary part of the dielectric index of the dust particles means that energy from the incident wave is lost by resistive heating in the particle. In the Rayleigh region (small particles compared with wavelength), this resistive loss varies as the cube of the particle radius,  $a$ , whereas the energy scattered by the particle depends on the sixth power of the particle radius. Both processes contribute to the loss of energy from the incident beam. Because of their differing dependencies on radius, it is evident that very small, partially conducting particles may extract more energy by resistive loss than through scattering. Inasmuch as we have no information concerning the imaginary parts of the dielectric constant of the dust particles, we necessarily have to ignore possible resistive losses. Since scattering losses for very small particles will be shown to be negligible, we assume that resistive losses are also miniscule. All of our extinction losses therefore are derived from scattering alone.

Customarily one computes losses in terms of dB along the path. The attenuation in dB has been calculated as follows:

$$\gamma = 4.34 \int \alpha \, ds \text{ (dB)} \quad (4-4)$$

where

$$\alpha = \int_0^{\infty} n(a) Q(a, \lambda) \, da \text{ (cm}^{-1}\text{)}$$



$a$  = Radius of particle (cm)

$n(a)$  = Number of dust particles per unit volume having  
radius size between  $a$  and  $a + \Delta a$  ( $\text{cm}^{-4}$ )

$Q(a, \lambda)$  = Scattering cross section for wavelength  $\lambda$  of  
particles having radius  $a$  ( $\text{cm}^2$ ).

The "e-folding" extinction length in centimeters equals  $1/\alpha$ .

If the particle size is very small compared with wavelength,  
then

$$Q(a, \lambda) = \frac{2}{3} \frac{\pi^5}{\lambda^4} (2a)^6 \left| \frac{\epsilon - 1}{\epsilon + 2} \right|^2 \quad (\text{Rayleigh scattering}) \quad (4-5)$$

For large particles we have used the particle cross section  $Q(a, \lambda) = \pi a^2$ . \* For spherical particles in the region  $2\pi/\lambda \approx 1$ , one would normally use Mie scattering theory. However, we believe that it is unlikely that the particles in the dust cloud will be spherical; if they are nonspherical, the "resonant" phenomena of Mie scattering is not important and a more practical value for the scattering cross section in this region will be  $Q(a, \lambda) = \pi a^2$ . The dividing line is taken as the radius at which the two cross sections, Rayleigh and geometric, are equal.

If the particle size distribution is assumed to be independent of both position in the cloud and dust density, then the number density of particles with radius  $a$  at point  $s$  may be found by

---

\* There are arguments that for computation of extinction we should use  $2 \times Q(a, \lambda)$ --i.e., twice the geometric cross section for the large particle regime. More thought will be given to this question in the future. But for the present planning estimates the factor of two is insignificant compared with accuracy of knowledge of the environmental properties.

$$n(a,s) = \frac{g(a) \rho_c(s)}{\rho_d \frac{4}{3}\pi a^3} \quad (4-6)$$

where  $g(a)$  is the initial fraction of total mass in particles with radius between  $a$  and  $a + \Delta a$ .<sup>\*</sup> The equation for attenuation in dB may then be written

$$\gamma = \frac{4.34}{\rho_d} \int \frac{g(a) Q(a,\lambda)}{\frac{4}{3}\pi a^3} da \int \rho_c(s) ds \quad (4-7)$$

where the first integral is calculated using the appropriate cross section  $Q(a,\lambda)$  for each particle size and frequency. Thus, according to Eq. (4-7) attenuation depends on the same integral of density as does the phase (second integral), and, in addition, it depends on the distribution of particle sizes (first integral).

The particle size distribution that has been used in our attenuation calculations was thought to be representative of the DICE THROW site. This distribution is presented in Table 4.1.

For illustrative purposes in this section, we also compute attenuation characteristics produced by a second particle size distribution, which is given in Table 4.2. This distribution is not representative of a particular ejecta-dust type but is used here to illustrate effects on the electromagnetic properties of the size distribution.

Figure 4.5 presents a plot of  $g(a)$  versus  $a$  for these two distributions. The distributions are very different in their characteristics,

---

\* Note that  $g(a)$  will be space- and time-dependent as  $g(a,s,t)$  for real situations as well as those internal to the HULL/DUSTY calculations. This detail from HULL/DUSTY is not available to us, so we have been forced to use the  $g(a)$  according to the size distribution at injection.

Table 4.1

## PARTICLE-SIZE DISTRIBUTION A

Particle Radius (cm)	Fraction of Ejecta Mass	g(a) (fraction per centimeter)
0.007 - 0.0075	0.083	166
0.0075 - 0.013	0.077	14
0.013 - 0.0205	0.073	9.73
0.0205 - 0.0325	0.067	5.58
0.0325 - 0.175	0.033	0.232
0.175 - 0.5	0.029	0.0892
0.5 - 5.0	0.153	0.0340
5.0 - 50	0.483	0.0107

Table 4.2

## PARTICLE-SIZE DISTRIBUTION B

Particle Radius (cm)	Fraction of Total Mass	g(a) (fraction per centimeter)
0.00 - 0.01	$3.7 \times 10^{-5}$	$3.68 \cdot 10^{-3}$
0.01 - 0.016	$8.1 \times 10^{-5}$	$1.34 \cdot 10^{-2}$
0.016 - 0.025	$2.37 \times 10^{-4}$	$2.62 \cdot 10^{-2}$
0.025 - 0.040	$8.66 \times 10^{-4}$	$5.77 \cdot 10^{-2}$
0.040 - 0.063	$3.99 \times 10^{-3}$	$1.73 \cdot 10^{-1}$
0.063 - 0.100	$1.30 \times 10^{-2}$	$3.51 \cdot 10^{-1}$
0.100 - 0.160	$5.11 \times 10^{-2}$	$8.51 \cdot 10^{-1}$
0.160 - 0.25	$1.75 \times 10^{-1}$	$1.94 \cdot 10^0$
0.25 - 0.50	$7.56 \times 10^{-1}$	$3.02 \cdot 10^0$

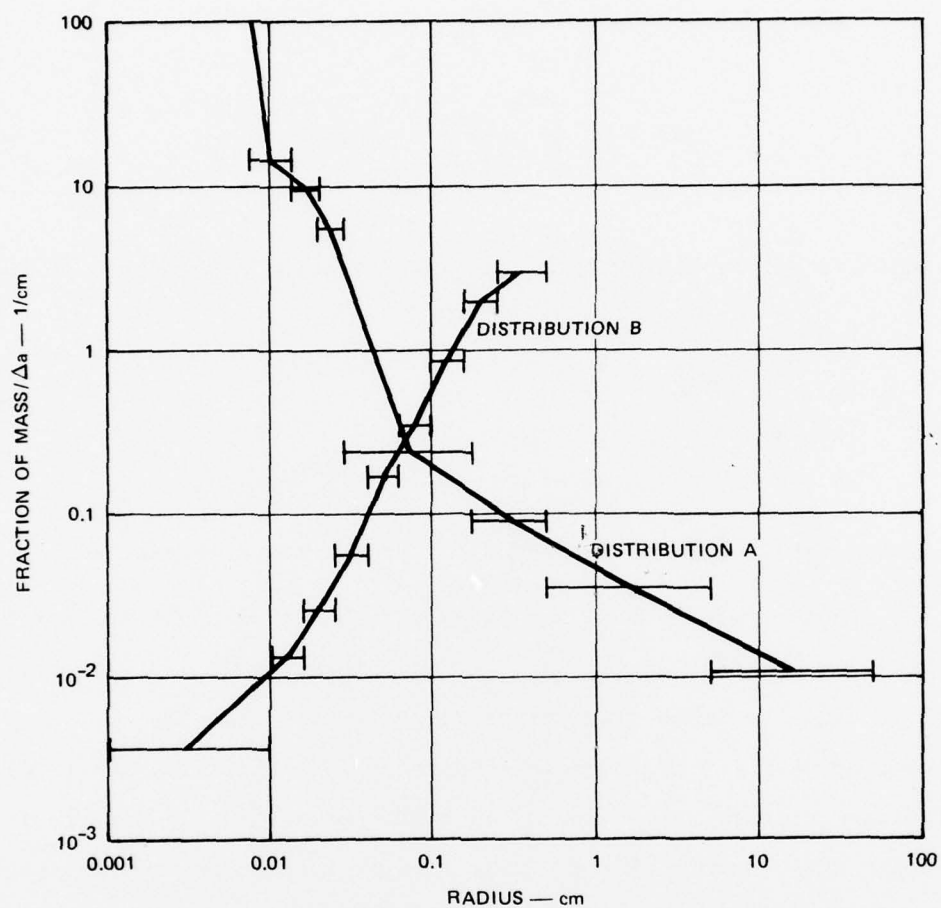


FIGURE 4.5 FRACTION OF MASS PER CENTIMETER OF RADIUS vs RADIUS FOR TWO PARTICLE-SIZE DISTRIBUTIONS

and these differences are reflected somewhat in the microwave and optical absorbing properties of the two distributions. Distribution A contains a major fraction of its mass in a few particles with radii between 5 and 50 cm; Distribution B has no such large particles.

Figure 4.6 presents a plot of the quantity

$$\alpha(a) = \rho_c \int_0^a \frac{g(a)}{\frac{4\pi}{3} a^3 \rho_d} Q(a, \lambda) da \quad (4-8)$$

as a function of the upper limit,  $a$ . The following parameters were used:

$$\begin{aligned} \rho_c &= 1 \text{ g/cm}^3 \\ \rho_d &= 2 \text{ g/cm}^3 \\ \epsilon &= 6 + j 0 \\ \lambda &= 3 \text{ cm, } 75 \text{ cm, very small (optical and IR).} \end{aligned}$$

(The unreasonably large choice for  $\rho_c$  is simply for convenience.)

Plots are presented for both Distribution A and B and for UHF (400 MHz,  $\lambda = 75$ ), X band ( $\lambda = 3$  cm), and optical/IR ( $\lambda < 0.001$  cm). The plots show the value  $\alpha(a)$  versus  $a$ , and reveal that the very large particles of Distribution A are needed to produce significant attenuation of microwave signals when compared with the optical loss. Note that the scattering cross section for the 3-cm wavelength changes from Rayleigh to geometric at about 1 cm for Distribution A.

These data help us emphasize several important considerations. Attenuation by dust, whether optical or microwave, is very dependent on the particle size distribution. This is not thought to be the case for the change in RF phase. Distribution A contains nearly 65% of the mass in particles with radii above 0.5 cm. We expect, as discussed in earlier sections, that these larger particles will rapidly fall out of the way. As a result, to estimate the expected microwave loss, not only is the cloud density  $\rho_c$  needed, but the detailed particle size distributions as a function of time and position in the cloud are also required.



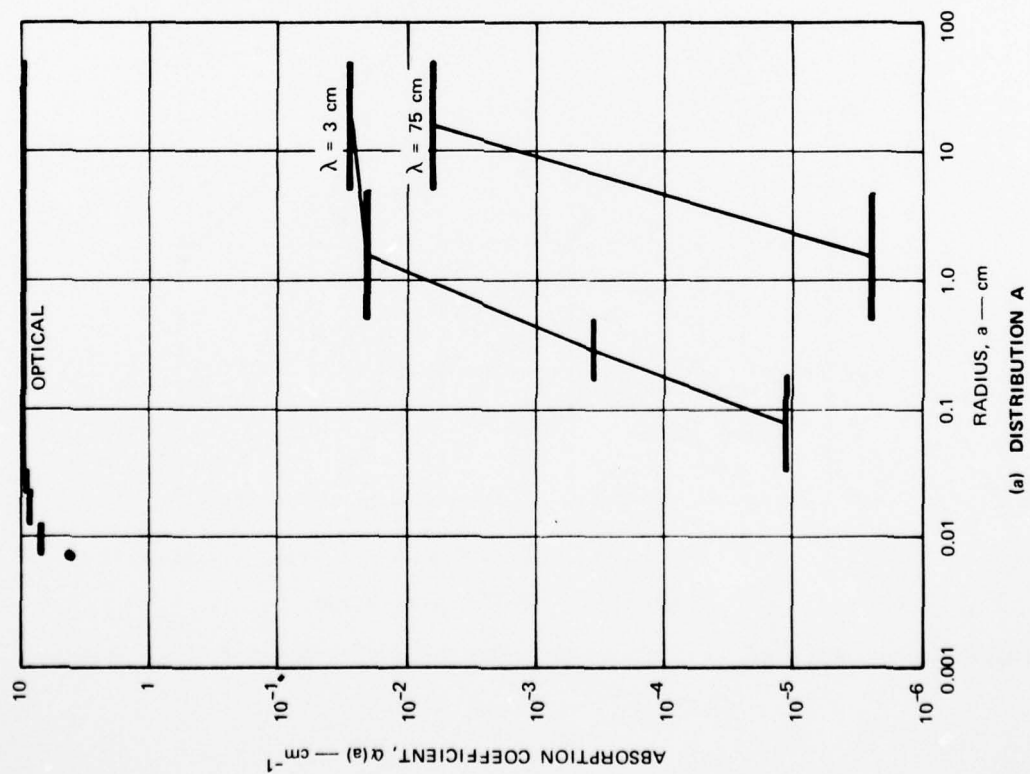
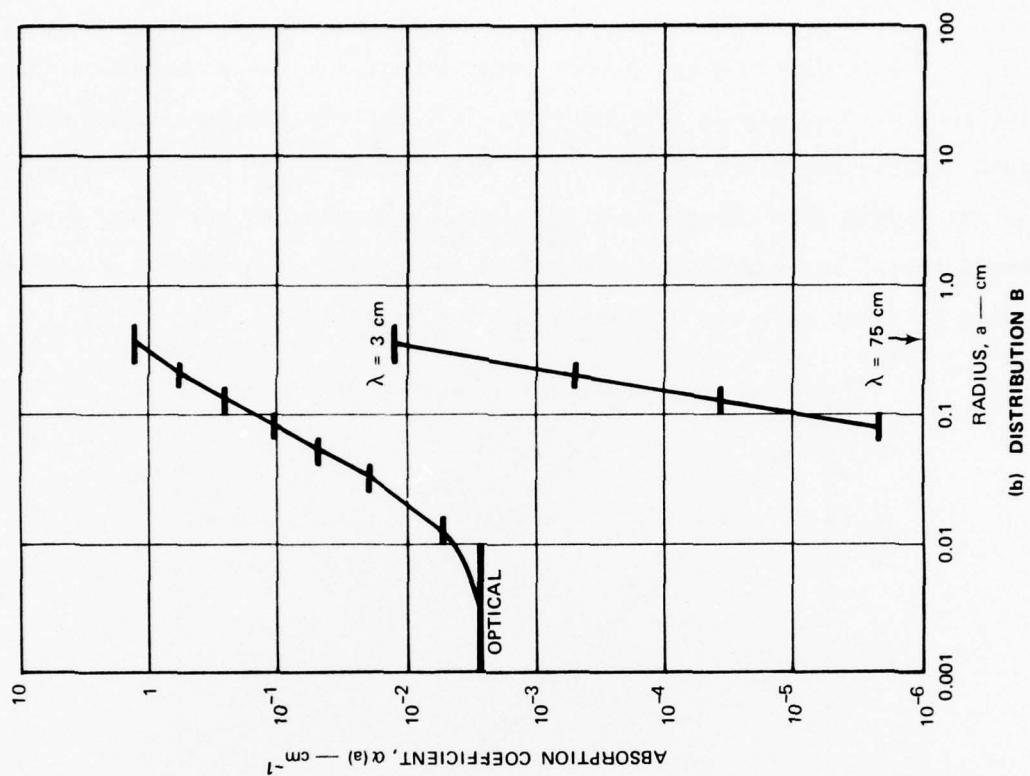


FIGURE 4.6 CUMULATIVE ABSORPTION COEFFICIENT,  $\alpha$  (a) VERSUS RADIUS,  $a$ , FOR TWO PARTICLE-SIZE DISTRIBUTIONS

In order to develop more intuitive insight into these attenuation problems, we present graphs of "e-folding" extinction lengths versus cloud density for Distributions A and B in Figure 4.7. Data are plotted for all wavelengths except that the extinction distance for 75-cm wavelength signal in dust with a density of  $10^{-2} \text{ g/cm}^3$  is 3000 km for Distribution B; these data are therefore off the figure.

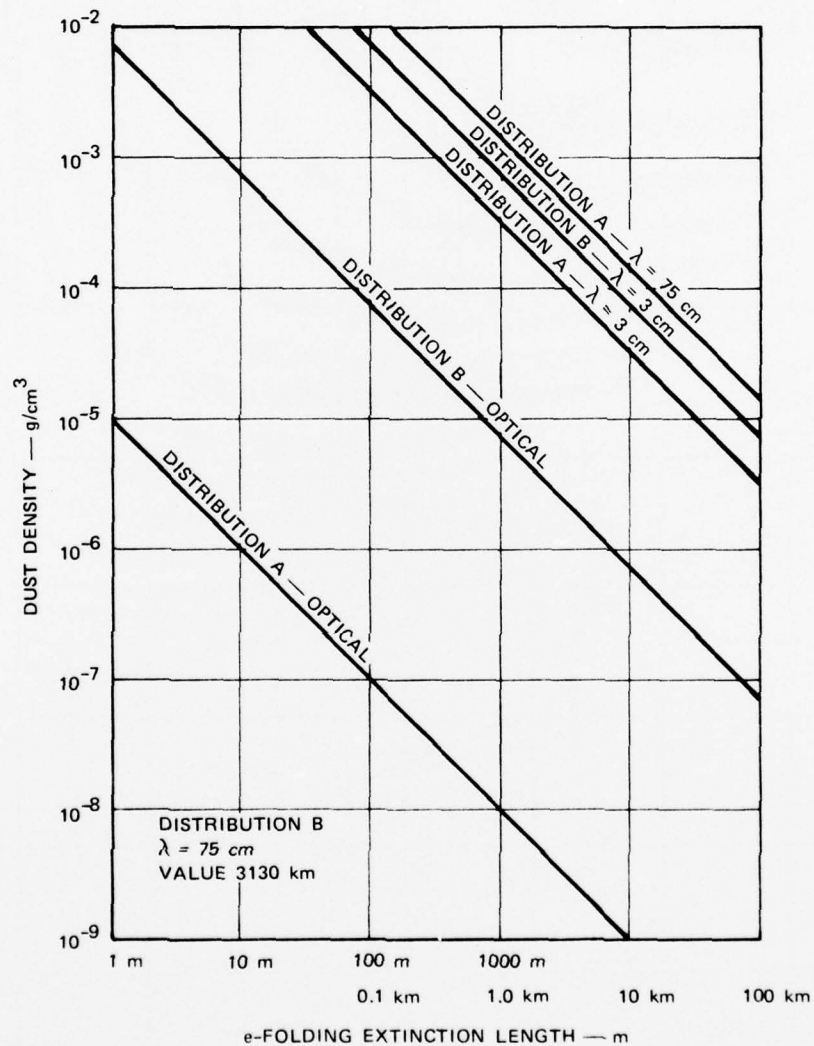


FIGURE 4.7 e-FOLDING EXTINCTION DISTANCE AS A FUNCTION OF DUST DENSITY

The figure shows that the optical e-folding length differs by a factor of 500 between Distributions A and B. Photographs therefore are not a reliable indicator of dust density. The fact that the extinction lengths for Distributions A and B are similar for a wavelength of 3 cm is purely accidental. The finite absorption length for Distribution A and  $\lambda = 75$  is produced by the few-in-number large particles that constitute a large fraction of the mass.

Estimates of attenuation to be presented in Section 4.3 are made using Distribution A.

#### 4.2.3 Diffraction and Refraction Phenomena

The dust-laden cloud leads to spatial variations in index of refraction. These variations can lead to ray bending at large dust loading densities and to diffraction at lesser densities. Because the transmitters and receivers are fixed in space, there are no means for us to probe the spatial features produced by these phenomena. However, severe diffraction may lead to amplitude fluctuations that could interfere with the data interpretation. Burns<sup>\*</sup> has investigated a few cases of diffraction caused by dust clouds. One example is presented in Figure 4.8. In this example, the dust cloud was in the form of a cylinder (of infinite length) that was 450 m in diameter. The transmitter was at infinity; the signal patterns at a plane 3.7 km on the other side of the cloud were computed for two frequencies and several dust densities. Figure 4.8 presents the significant results for two frequencies--425 MHz and 8915 MHz. These calculations are for a dust cloud with very sharp edges, and therefore represent an extreme case. Data for several dust densities are given; curves are shifted by 10 dB to minimize confusion.

---

\* Alan Burns, private communication. We are indebted to Dr. Burns for permitting the results of his calculations to be displayed here.

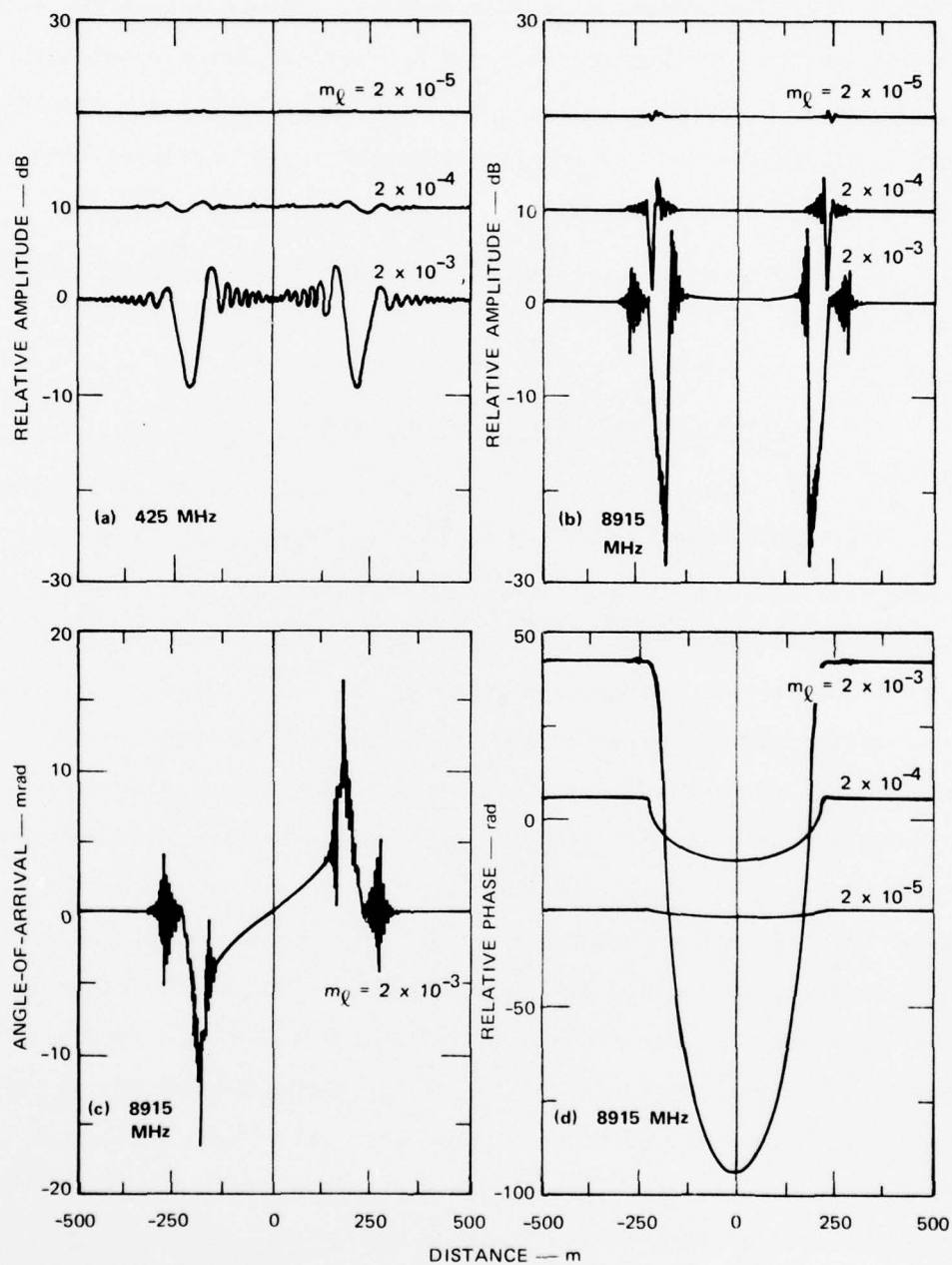


FIGURE 4.8 DIFFRACTION PHENOMENA PRODUCED BY A CYLINDRICAL DUST CLOUD (curves for differing dust loading densities have been shifted by 10 dB). (See text for dimensions.)

The concern with these data is that similar phenomena may affect interpretation of the field experiment results. For example, should a receiver be located in a region of rapid spatial amplitude fluctuation, then slight motion of the cloud by the wind would translate these spatial fluctuations into temporal fluctuations in the receiver. They might then be interpreted as resulting from the effects produced by turbulent mixing. We note with some satisfaction that the expected spatial variation in phase does not seem severely altered by diffractive effects. Thus we would expect that the phase measurements should be reliably interpretable.

There are two other factors that we believe reduce the hazards in data interpretation that might result from diffraction. The first factor applies to the lower paths. The transmitter for those paths was purposely placed as close as possible to the detonation in order to cause the first Fresnel zone to be as small as possible. The first zone, which is indicative of the magnitude of diffraction effects, is more than 2.5 times smaller for the DICE THROW experiment than it is for the calculation of Figure 4.8.

The second factor applies to the upper lines of sight. For these paths the first Fresnel zone is comparable to that of the calculation. However, photographs of the PDT II-2 cloud suggest that at an altitude of 190 m the features of the cloud are soft, suggesting gradual boundaries between the dust and the surrounding air. "Soft" edges are very favorable for the suppression of diffraction.

Ray bending due to refraction could produce some effects. However, effects of small angle refraction in the cloud upon amplitude at the receiver are automatically computed in a diffraction calculation. Thus, they are included in the results of Figure 4.8.



Scintillation effects due to turbulent mixing of clean and dirty air are likely to be observed. They should be detectable in both the phase and amplitude data.

#### 4.3 Prediction for Microwave Propagation Experiment on DICE THROW

Figure 4.9 presents five photographs of the PDT II-2 detonation at various times. We have scaled time and linear dimensions in these photographs according to the cube root of yield in order to simulate the larger DICE THROW explosion. Plotted on the photographs are the position of the six propagation paths of the microwave experiment. The first panel provides a legend to the frequencies to be employed in the experiment. In the following paragraphs we shall assume that the yield scaling procedure that we used is accurate. We shall also assume that the different soil conditions at the DICE THROW site (blow sand back-fill) do not change the phenomena. Both assumptions could be poor.

Figure 4.9 reveals that the propagation Paths 1 and 2 will be occulted not only by the ejecta spires, but also by the ground surge considerably before the 1.7 s scaled time of Figure 4.9(b). We do not know the nature of the material in the ground surge and therefore have no model to employ for prediction purposes. We believe its effects will be additive to those of the ejecta cloud. It appears that Path 3 could provide a direct measure through the ground surge only and thereby aid in determining its nature and in removing its effects from the data obtained along Paths 1 and 2.

According to Figure 4.9(b), by 1.7 s the ejecta spires have exceeded the height of Path 4, but PDT II-2 ejecta spires were apparently not circularly symmetric so that Path 4 in this particular case would have been occulted later than according to our model. Presumably a path (Path 4') oriented at  $90^\circ$  in azimuth compared with Path 4 would have been well occulted by the time of this photograph.

1: 378, 413, 447, 1273, 2891, 10188 MHz

2: 413, 10128 MHz

3: 413, 10128 MHz

4: 424, 8914 MHz

5: 424 MHz

6: 424 MHz

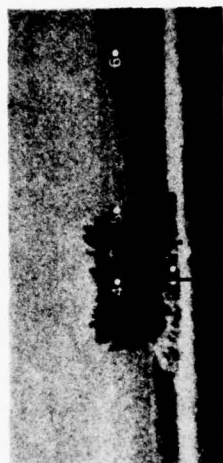
4• 5• 6•

$1\frac{1}{2} \times 2 \times 3$

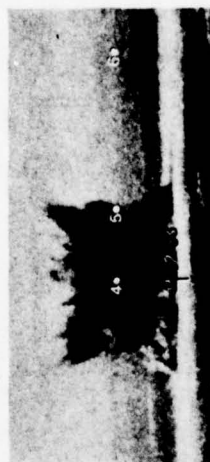
(a) RAY-PATH CONFIGURATION



(b) 1.71 SECONDS



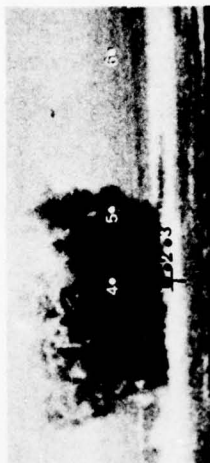
(c) 3.42 SECONDS



(d) 6.84 SECONDS



(e) 18.68 SECONDS



(f) 25.65 SECONDS

FIGURE 4.9 YIELD-SCALED PHOTOGRAPHS OF PDT II-2 SHOWING ANTICIPATED INTERSECTION OF PROPAGATION PATHS WITH DICE THROW PHENOMENA: DIMENSIONS AND TIME SCALED AS  $\sqrt[3]{t}$  (photos courtesy of A. D. Thornbrough, Sandia Labs)

These photographs and our scaling indicate that Path 5 will not be directly occulted by the spires. However, by 6.8 s [Figure 4.9(d)], dust from the spires will have occulted this path by turbulent transport from the spires. We assume that the material in the spires produces a turbulent wake, seeded with dust eroded from the surface of ejecta clods that turbulently expands outward. The geometry used for ejecta in DUSTY does place material in the way of this path so that we have some predictions. Path 6 is not expected to be affected by dust unless winds transport material into that path. If that happens, it will probably do so after passage of several minutes or more.

We now present our best estimates of phase and amplitude variations as functions of time for the imminent DICE THROW transmission experiment. These estimates are based on two models: (1) DUSTY calculations using inputs specified by us from measurements of PDT II-2 photographs, and (2) our analytic model of the rising ejecta cloud for the first 5 s interval.

The input parameters specified for use in DUSTY were as follows:

Amount of dust injected	8 kT
Radius of ejection zone	39 to 106 m
Initial velocity of ejecta	10 to 300 m/s
Ejection angles	50 to 75°
Particle-size distribution	A (see Section 4.2)

The AFWL performed three additional sets of DUSTY calculations for us that clarified the effects of variations in the above input parameters. Although we present here only the set of results that best represents our expectations for DICE THROW, the remaining sets would be useful in an after-the-fact parametric study directed toward improving prediction capabilities.

For each of the five transmission paths (Path 6 is not expected to intersect the cloud) and for each of the frequencies to be used on the path, we have calculated phase and amplitude variations during the first 60 s. The results are summarized in Figures 4.10 through 4.14. These results were derived from the DUSTY mass-density calculations. Predictions of phase change during the first 5 s based on our analytic simulation, are presented in Figure 4.15. Because the most important data for modeling purposes are the phase measurements, we discuss their predicted temporal variations for all paths before commenting on the amplitude effects.

The most important conclusion to be drawn from Figures 4.10 through 4.15 is that measurable phase changes are to be expected on all paths and for all implemented frequencies. With the exception of the UHF link on Path 5, the phase effects should remain at a significant level for most of the 60 s interval covered by the predictions; Path 5 approaches the sensitivity limits of the equipment after 10 to 15 s. Thus, unless the model is grossly in error, the experiment should provide meaningful diagnostics for future theoretical modeling. Notice that the X-band phase shift on Paths 1 through 4 would still remain easily measurable even if our estimate of 8 kT of injected dust were to be too large by an order of magnitude. Moreover, because the model parameters were derived initially from yield-scaled photographs, the experiment will test the validity of this approach.

We first consider the phase-shift predictions for Paths 1 and 2 as summarized in Figures 4.10 and 4.11 for DUSTY and in 4.15 for our analytic model. According to the DUSTY model, the phase shift for a wavelength of  $\sim 3$  cm drops from over 40 rad at 1 s to about 15 rad at 5 s decreasing very slowly thereafter. In the analytic model (Figure 4.15) the phase shift on Path 2 drops from 80 rad at 1 s to  $\sim 50$  rad at 5 s. Inasmuch as



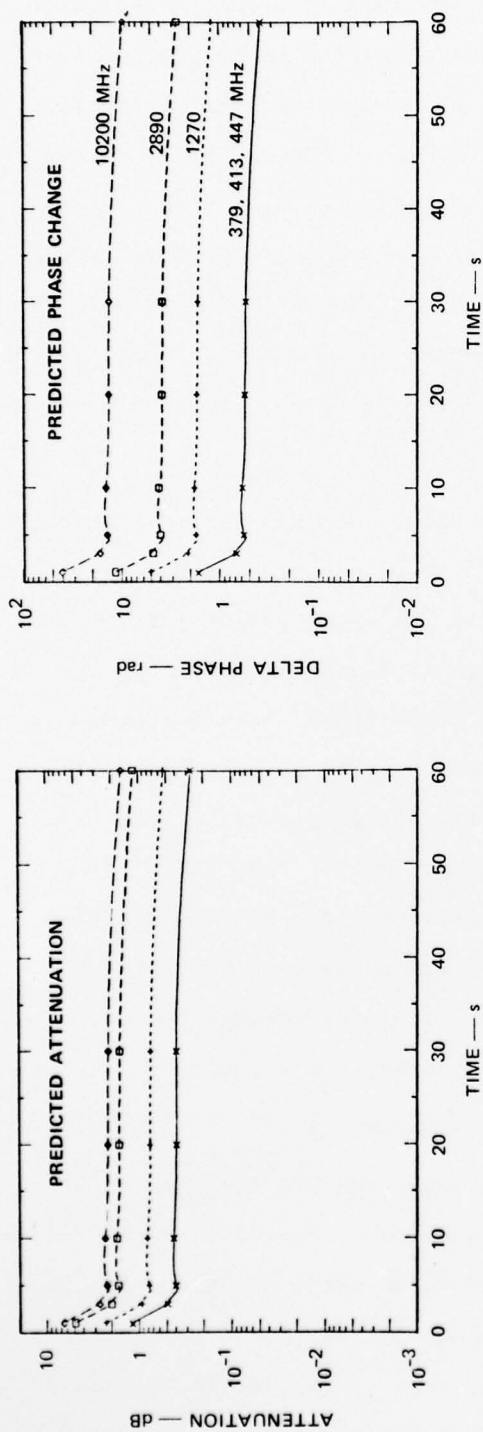


FIGURE 4.10 PREDICTED ATTENUATION AND PHASE CHANGE vs TIME — PATH 1

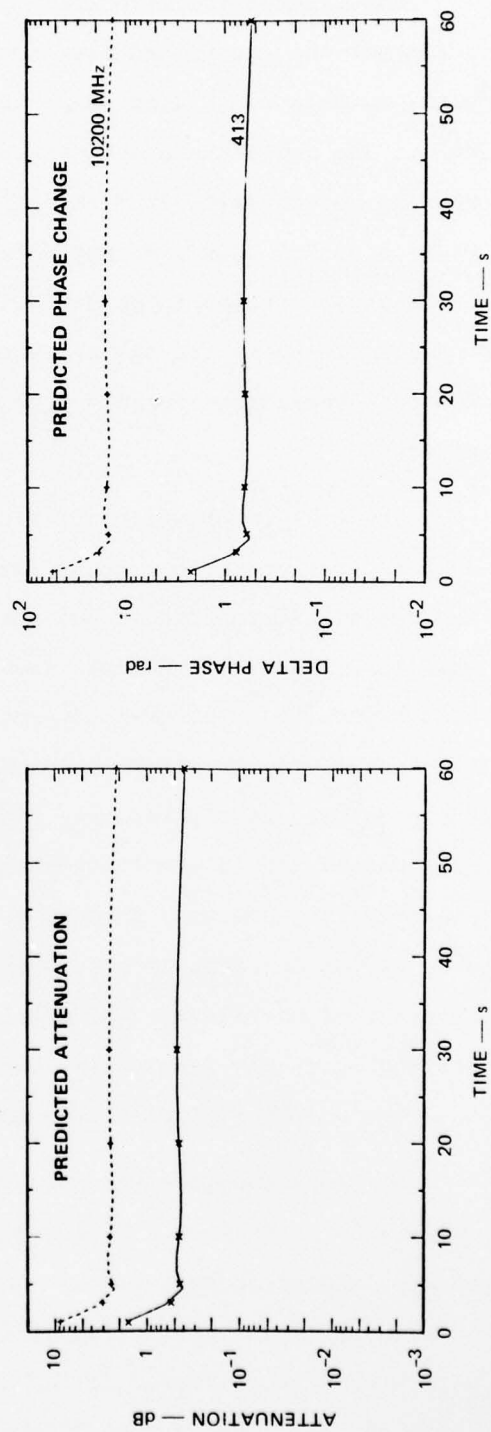


FIGURE 4.11 PREDICTED ATTENUATION AND PHASE CHANGE vs TIME — PATH 2



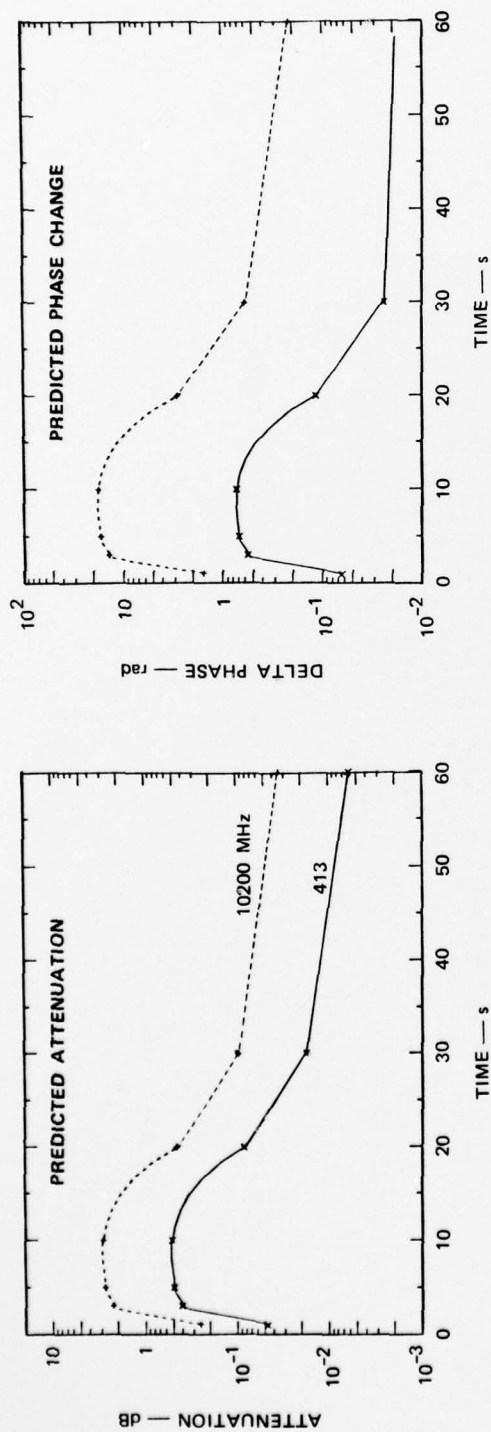


FIGURE 4.12 PREDICTED ATTENUATION AND PHASE CHANGE vs TIME — PATH 3

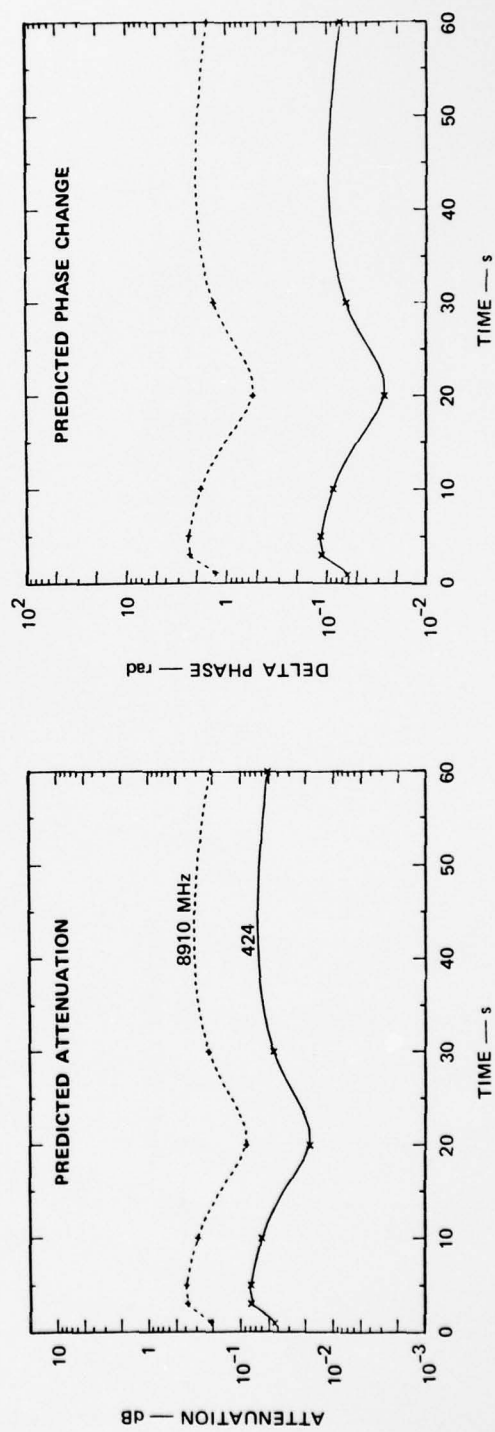


FIGURE 4.13 PREDICTED ATTENUATION AND PHASE CHANGE vs TIME — PATH 4

AD-A040 907

STANFORD RESEARCH INST MENLO PARK CALIF  
PREDICTIONS OF EFFECTS PRODUCED BY THE DICE THROW DETONATION ON--ETC(U)  
SEP 76 R L BOLLEN, V E HATFIELD, W G CHESNUT DNA001-76-C-0207  
DNA-4183T NL

UNCLASSIFIED

2 OF 2

AD  
A040907



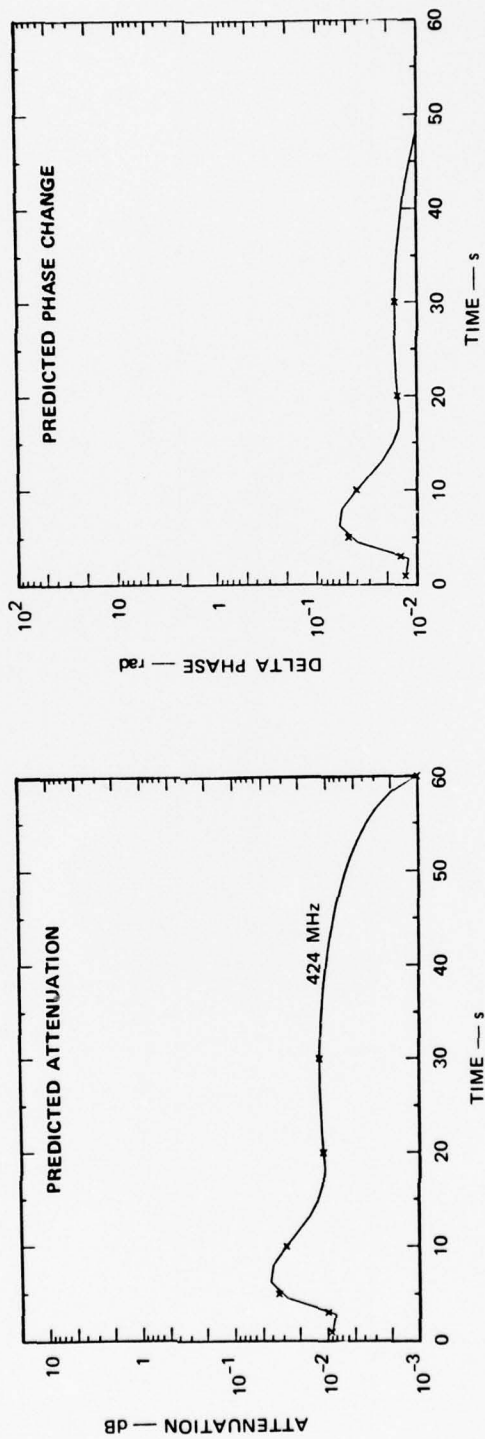


FIGURE 4.14 PREDICTED ATTENUATION AND PHASE CHANGE vs TIME — PATH 5

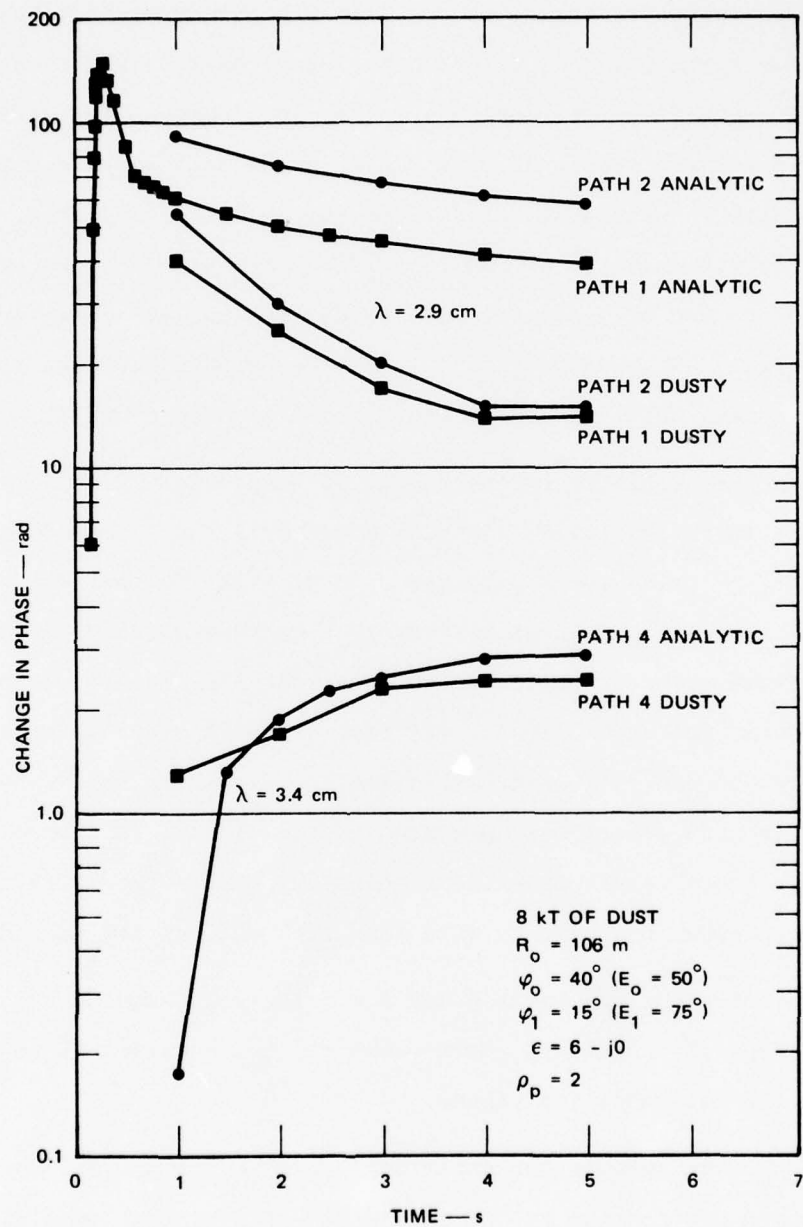


FIGURE 4.15 EARLY-TIME PHASE PATH VARIATION FOR THREE PROPAGATION PATHS

the AFWL technique uses an initial velocity of 300 m/s, while our analytical model takes 4.5 s to reach that altitude, the proper comparison to be made between the technique is our 4 to 5 s values against DUSTY 1 s values. For Paths 1 and 2, this comparison reveals nearly identical phase shifts. The DUSTY ejecta continues to spread geometrically after 1 s, so that the integrated amount of dust continues to decline past this time. The very heaviest particles (up to 1 m) suffer little air drag, so we suspect that within a few seconds all of these particles (representing perhaps 60% to 80% of the mass) have moved past the microwave propagation lines of sight. We surmise that this is the principal reason for the decline in phase shift between 1 and 5 s as computed by DUSTY.

The generic behavior of the change of phase along Path 1 as presented in Figure 4.15 is physically reasonable; after a short time delay (less than 0.1 s), material moves into the line of sight so that the integrated density increases for a short period, then decreases. As indicated in earlier sections, we suspect that our analytical procedure may not well mimic nature. The actual ejecta may rise as solid clods of dirt with their surfaces eroding away, thus creating smaller particles that then expand outward in the turbulent wake produced by the clods. In this case the Path 1 signal may be extinguished completely, then return with a phase shift that changes only slowly with time in the first few seconds.

The predictions for Paths 3 and 5 are the most uncertain. Being near the edges of the cloud, these paths are quite sensitive to details of the artificial injection scheme.

A comparison between our analytical technique and DUSTY for Path 4 should equate our results at 5 s with DUSTY at 1 s; this comparison is not as favorable as were the results for the low-elevation Paths 1 and 2. We do not have a reasonable explanation for this apparent difference of a factor of 2 (2.8 rad for our analytical technique versus 1.3 rad



according to DUSTY). Despite this difference, we feel that the Path 4 behavior presented in Figure 4.15 has greater temporal validity than our early-time predictions. Dust-produced phase shifts will onset gradually after about 1 s of delay, reaching a maximum value at about 5 s.

Figures 4.10 through 4.14 also show attenuation predictions for each frequency employed on the given path. These attenuation predictions are based on the DUSTY mass loading density under the assumption of an unchanging particle size distribution. Note that even with the presence of very large particles, the attenuation is not very large for any path.

There are several known imperfections in these propagation estimates. First, it is quite clear that if any large particles were initially present in the ejecta, they would most likely have fallen back to earth after a few seconds. However, as shown earlier (Section 4.2), these largest particles are primarily responsible for producing attenuation. If they were removed, the attenuation coefficient for UHF and X-band signal would become vanishingly small. Therefore, we believe the attenuation in Figures 4.10 through 4.14 is very greatly overestimated for times later than a few seconds. On the other hand, the phase-change results of Figures 4.10 through 4.15 are not seriously affected by expected changes in the particle size distribution.\*

Another possible imperfection in these predictions results from the fact that the DUSTY-predicted dust cloud remains nearly static in shape after about 10 s so that phase path variations change only very slowly. (Note that Path 3, whose phase characteristics continue to change past 10 s may be affected not by hydrodynamic motions moving dust about but

---

\* If the ejecta cloud contains only the blow sand and no large particles, then we estimate that the later time phase shifts in Figures 4.10 through 4.14 will be about three times that given in the figures. Likewise, we believe attenuation would probably be negligible.

by dust particles falling under the influence of gravity from the ejecta cloud.) Photographs of PDT II-2 show a rising dust cloud that DUSTY/HULL does not seem to mimic well. The AFWL has informed us that the late-time HULL results for the DICE THROW fireball regions used in these estimates are so coarsely meshed, because of the requirement to expend mesh points to well cover the shock region, that the results probably poorly represent the real fireball region. It is for this reason that the AFWL terminated their calculations at 60 s. At this writing we understand that efforts are underway by the AFWL to produce what they believe will be far superior estimates of the fireball regions.

## 5. SUMMARY AND CONCLUSIONS

This report is a compilation of work performed by SRI using a considerable number of inputs, particularly from the AFWL, in an attempt to predict effects to be measured by the microwave propagation experiment during the upcoming DICE THROW simulation test. The end product of this work is a series of estimates of phase path variation and attenuation as a function of time produced by explosion-lofted dust. The primary diagnostic for each propagation path is phase shift versus time. These phase data will provide a measure of integrated dust density in portions of a high-explosive dust cloud for which there are, at present, no experimental data whatsoever.

The most important conclusion of the theoretical analysis presented in this report is that the experiment will indeed yield very useful diagnostics. Although we have little confidence in the details of our predictions (for reasons to be discussed shortly), the very large X-band phase shifts predicted for four of the paths lead us to believe that valuable quantitative data will be obtained even if our predictions prove to be in error by an order of magnitude.

The artificial scheme for ejecta deployment was devised to model the features of the PDT II-2 dust cloud (yield-scaled in time and linear dimensions to DICE THROW), as deduced from photographic evidence. The ejecta scheme was not based on the physical mechanisms of the cratering process, but merely on the visible features that resulted from these mechanisms. Should this prove to be a valid technique in the case of DICE THROW, a similar analysis of photographic data from nuclear tests would seem a logical means of enhancing present capabilities in the area of nuclear dust cloud modeling.

We believe that the unique photographic sequences of HE- and nuclear-produced dust clouds presented in Section 2 show that the gross features of the DICE THROW dust cloud will be similar to those expected from slightly buried nuclear charges. The photographs seem unambiguous in showing that DICE THROW dust geometries will not be similar to those produced by a nuclear detonation slightly above the ground.

Our attempts to compute phase path changes and signal attenuation for the microwave propagation paths depend on a number of factors that are not well known or not currently calculated with high confidence, or that have not been well measured. However, this exercise has been useful in that it provides an avenue for comparison between data and predictions that should ensure more accurate prediction in the future.

We briefly review the uncertainties that currently dominate our opinion of the accuracy of our estimates:

- (1) Based on advice from the AFWL we have used the amount of material from the expected apparent crater as the total mass of the ejecta cloud. Neither we nor the AFWL personnel are very confident that this is an accurate estimate. The experiment may improve our estimates for future experiments.
- (2) Motion of the PDT II-2 late-time dust cloud (past 10 s) is not well reproduced by the HULL/DUSTY data currently provided by the AFWL. The late-time photographs show the dust cloud rising; HULL/DUSTY calculations using dust injected even vertically (an example run by the AFWL with ejecta elevation angles between  $30^\circ$  and  $90^\circ$ ) do not show this behavior. The failure of HULL/DUSTY to produce this later rise, we understand, is related to large mesh size forced by other constraints onto the calculational data on hand. From our point of view, the problem is that the AFWL has been asked in the past to provide accurate shock wave estimates. We have been using HULL results from those calculations. The simultaneous generation of accurate fireball and shock wave representations is, we understand, prohibitively expensive. The AFWL informs us that they are currently performing more finely meshed



fireball calculations, preliminary results of which seem far more promising. We believe that the HULL code can and will produce considerably more accurate flow fields in the fireball region in the future.

- (3) The injection of dust into the DUSTY code is performed by a rather clever scheme devised by the AFWL. However, no one currently knows the accuracy of simulation of the ejecta cloud characteristics based on this scheme. We expect that the propagation experiment will provide the first direct experimental data that will be useful in verifying or revising the ejecta procedures.
- (4) Microwave attenuation estimates depend critically on particle size estimates. We believe that there is considerable uncertainty about the particle size distribution in the ejecta cloud. Finite absorption that we estimate in Section 4 is quite small; however, that it even exists in the calculational results is due only to the presence of large particles, considerably larger than a centimeter in diameter, in the ejecta cloud. We believe that the terminal velocity of fall for such particles is large enough so that after a few seconds they will no longer be a factor in dust effects. Furthermore, the DICE THROW experiment will take place in a region that is backfilled with fine-grained dust to suppress large ejecta. From a practical systems point of view, any link outage on DICE THROW due to attenuation by particles will have a duration of only a few seconds.
- (5) The estimates presented here take into account only dirt in the ejecta cloud. We have made no predictions for the surface surge and sweep-up contribution. These additional sources of dust are expected to increase the predicted phase shifts on the three lower paths, but the relative magnitude of these effects is not known by us at present.
- (6) An important goal of this study was to gain insight into the relationship between dust effects produced by the HE experiment and dust effects produced by nuclear explosions. One important part of such a comparison is the microscopic characteristics of the dust particle cloud such as particle size distribution, dielectric properties, shape, etc. We have not pursued this question in any detail. For ejecta clouds of the type that we suspect will dominate DICE THROW dust phenomena, we guess on physical grounds



not discussed herein that the dust particle distribution and other characteristics will be quite similar to the characteristics of ejecta clouds produced by slightly buried nuclear charges.

We close by again expressing our sincere appreciation to Major Gary Ganong, Dr. Charles Needham, Mrs. Susan Check, and Dr. Robert Henny of the Air Force Weapons Laboratory for their continuous support and very rapid response to our needs. Almost all of the dust environment data included here were generated by these individuals and their co-workers at our request.

Appendix A

ANALYTICAL EJECTA MODEL

## Appendix A

### ANALYTICAL EJECTA MODEL

This analytical ejecta model was developed in order to follow the ejecta deployment at early times that are not handled by the AFWL/DUSTY code. The model was devised in such a way that when ejecta stops (expected at about detonation plus 5 s for the 600-ton ANFO detonation), the dust density is similar to that provided by the AFWL. (DUSTY always assumes this stopping distribution to be appropriate to about one second despite the larger deployment times that we measure from photographs.) For this reason we give a brief summary of the AFWL ejecta deployment scheme.

The AFWL group considers  $n$  particles leaving sequentially at equal intervals between 0.05 s and 1.0 s; each particle travels until one second as in a vacuum but still under the influence of gravity. Each particle has, in expectation, the same mass as all others even though each particle's mass, chosen by the Monte Carlo method, is different than this average. The particle's velocity is, in expectation, uniformly distributed between a minimum and maximum velocity. Figure A-1 schematically shows the distribution of dust at one second according to an approximation to the AFWL technique. If one ignores gravitational slow-down, then at any instant of time during deployment the mass per unit distance from the starting point may appear as in the figure. We have illustrated eight particles for clarity rather than the very large number of particles as used by AFWL. AFWL considers the particles to have a minimum velocity; in our derivation here we shall assume that minimum is zero. In our theory it is a very easy task to include the

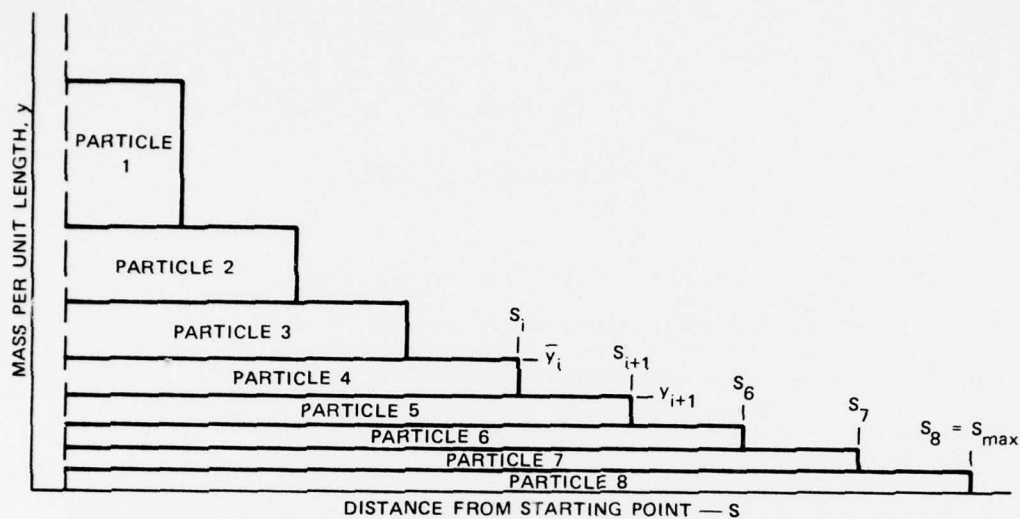


FIGURE A-1 SCHEMATIC DISTRIBUTION OF DIRT UTILIZING AFWL TECHNIQUE AT 1 SECOND

effects of the minimum velocity, but for reasons of clarity we shall not do so. The following relations are apparent from the figure if we assume a minimum velocity of zero:

$$y_j = \sum_{i=j}^N \Delta y_i \quad (A-1)$$

$$\Delta y_i \cdot S_i = \text{constant} = m \text{ (expectation or average mass per particle)} \quad (A-2)$$

$$N \cdot m = M_T \text{ (total mass)} \quad (A-3)$$

Thus,

$$y_j = \sum_{i=j}^N \frac{m}{S_i} = \sum_{i=j}^N \frac{m}{S_i} \Delta i \quad (A-4)$$

Note that  $\Delta i \equiv 1$ .

We use the relation

$$\frac{S_{\max}}{\Delta S} = \frac{N}{\Delta i} \quad (\text{A-5})$$

to convert Eq. (A-4) from a summation over  $i$  to an integral over  $S$  to obtain

$$y(S) = mN \sum_j^N \frac{1}{S_i} \frac{\Delta S}{S_{\max}} \cong \frac{M_T}{S_{\max}} \int_S^{S_{\max}} \frac{dS}{S} \quad (\text{A-6})$$

The integration gives the following

$$y(S) = \frac{M_T}{S_{\max}} \ln \left( \frac{S_{\max}}{S} \right) \quad (\text{A-7})$$

where  $y(S)$  is the mass per unit distance.

For convenience in studying geometric spreading, we shall assume that the dust is ejected as illustrated in Figure A-2. Actually, much more complicated expressions can be written in which the dirt comes from the ground surface meaning that  $r_o$  is a function of the angle  $\phi$ . For simplicity we let the dust emanate from a constant radius,  $r_o$ . We accept this approximation here because we are most interested in times when  $S_{\max}$ , which increases with time, is significantly larger than  $r_o$ . Also,  $\phi_o$  is taken to be  $30^\circ$  or larger so that the error is minimized.

Accepting these approximations, we can show that

$$\rho(r) = \frac{M_T \ln \left[ \frac{S_{\max}}{r - r_o} \right]}{2\pi S_{\max} r^2 (\phi_o - \phi_1)} \cdot \frac{1}{\sin \phi} \quad (\text{A-8})$$



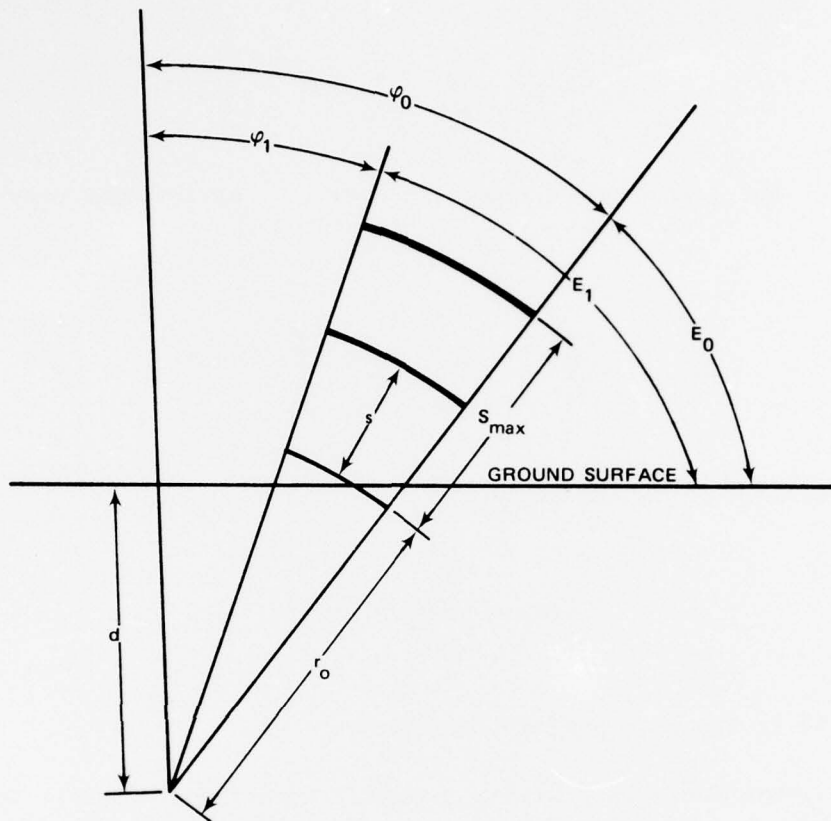


FIGURE A-2 GEOMETRIC SCHEMATIC OF DUST EJECTION

This expression results if one assumes that the amount of material ejected is not a function of angle of ejection.

Figure 3.5 in the main text shows a comparison between our expression (A-8) and AFWL/DUSTY results at one second. The comparison is made along a line of  $60^\circ$  elevation. In both models,  $M_T = 15$  kT. The AFWL data points result from our averaging the density in five horizontal cells about the  $60^\circ$  elevation angle. The dust is assumed in both calculations to be distributed between  $\varphi_0 = 0^\circ$  and  $\varphi_1 = 60^\circ$  [ $E_1 = 90^\circ$  and  $E_0 = 30^\circ$ ]. The value of  $r_o$  was chosen by us to correspond to dust lofting from radii out to about 30 m, the maximum radius used by AFWL.

Appendix B

BRIEF DESCRIPTION OF HULL/DUSTY ANFO CALCULATIONS  
AS PROVIDED BY THE AFWL

## Appendix B

### BRIEF DESCRIPTION OF HULL/DUSTY ANFO CALCULATIONS AS PROVIDED BY THE AFWL

The AFWL prepared for our use a brief memorandum describing the HULL/DUSTY calculations as used in the body of this report. The memorandum, which follows, was written by Major Gary Ganong of the AFWL and reviewed by Dr. Charles Needham and others at the AFWL. The memorandum was received on 13 September 1976.

#### HULL/DUSTY ANFO CALCULATIONS

The Air Force Weapons Laboratory performed calculations of the DICE THROW dust cloud with the HULL hydrocode and the DUSTY particle trajectory code. The HULL code (see AFWL-TR-76-183) is an Eulerian, finite difference, time marching code, which in this case was run with cylindrical coordinates. The assumption of axial symmetry (no winds) reduces the problem to two dimensions, radius (x) and altitude (y). The DUSTY code flew dust particles through the HULL calculated environments assuming that air drag and gravity acted on the dust, but ignoring dust effects on the air.

Two thousand representative dust particles were ejected from the crater. Their initial conditions were randomly chosen:

- Particle radius: from 0.007 cm to 50 cm
- Initial velocity: from 10 to 220 m/s
- Initial ground range: from 39 to 106 m
- Initial angle: from  $50^{\circ}$  to  $75^{\circ}$
- Ejection time: from 0.05 to 1 second after detonation.

Air drag was considered starting at 1 second after detonation. From the ejection time until 1 second, only gravity affected the particle trajectories. After 1 second, air drag was included using the results of the HULL calculations. The HULL environments were contained in a finite difference mesh of 140 rows and 120 columns. Table B-1 shows the

Table B-1

TOTAL MESH SIZE VERSUS TIME  
(Abbreviated Table)  
Problem Number 6001.00720

Time	DX	DY
1.00000	505.30004	395.98632
2.00000	823.22712	677.27099
3.00000	1158.36323	952.98829
4.00000	1478.39763	1216.28139
5.00000	1797.00156	1478.39763
10.00000	3227.15662	2787.73922
15.00000	4767.98011	3922.62904
20.00000	6085.28511	5256.69807
30.00000	8562.60725	7396.70288
40.00000	9912.28821	9440.27449
50.00000	10407.90262	10407.90262
60.00000	10407.90262	10928.29775

increase in column size, DX and row size, DY, with time.\* At 1 second, the computational mesh consisted of zones which were 4 meters high and 5 meters in the radial direction. So the initial cloud which was 200 meters high and 200 meters in radius was described by thousands of zones. At 60 seconds, the computed dust cloud is still the same size, although

---

\* The table as published here is considerably abbreviated from that provided to SRI by the AFWL.

two thirds of the mass has fallen out. The computational mesh has grown to 100 meter zones to follow the shocks, leaving only 4 zones to describe the hydrodynamics of the dust cloud. This inadequate zoning is insufficient to describe the motion of the dust cloud.

The dust density plots were obtained by assigning a fraction of the ejecta mass to each representative particle. The ejecta was divided into size groups (Table B-2). The total amount of ejecta was assumed to be 15 kilotons. This assumes that most of the apparent crater mass is lofted up into the air. If there were  $n$  particles with a radius of 0.007 to 0.0075, then each particle would be assigned a mass of 15 kilotons  $\times$  0.083/ $n$ . A mesh was constructed around the computed dust cloud. The mass of each zone was defined as the sum of the masses of the particles in that zone. To produce a smoother cloud, half of the mass in each zone was moved to the eight surrounding zones. This has been shown to have the same effect as doing a calculation with many more particles, but reduces the cost of calculations considerably.

Table B-2

PARTICLE RADIUS VERSUS FRACTION OF EJECTA MASS

Particle Radius (cm)	Fraction of Ejecta (mass)
0.007 to 0.0075	0.083
0.0075 to 0.013	0.077
0.013 to 0.0205	0.073
0.0205 to 0.0325	0.067
0.0325 to 0.175	0.033
0.175 to 0.5	0.029
0.5 to 0.5	0.153
5. to 50.	0.483



The configuration of the ANFO tends to produce a radial expansion of the detonation products which cause cloud rise. Therefore the AFNO cloud is much slower to rise than a nuclear cloud. The configuration of a TNT tangent sphere produces a toe of detonation products which also slows down the cloud rise, compared to the nuclear case. To learn the effect of charge composition on cloud rise would require two calculations with the same charge shape, but with different materials. No such calculations exist at this time.

Appendix C

DEMONSTRATION OF EFFECT OF ZONING SIZE  
IN FIREBALL REGION ON CLOUD-RISE VELOCITY

## Appendix C

### DEMONSTRATION OF EFFECT OF ZONING SIZE IN FIREBALL REGION ON CLOUD-RISE VELOCITY

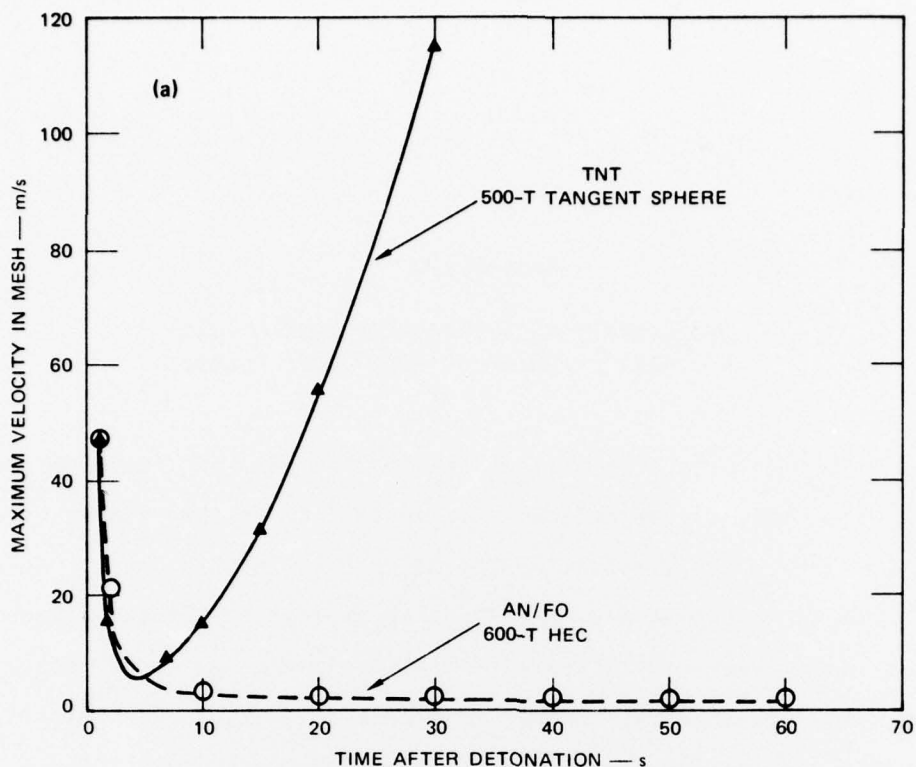
In the body of this report it was pointed out that the HULL/DUSTY calculations that were completed in time for use in this report were thinly meshed in the fireball region of concern in this study. Since completion of our work, the AFWL have reperformed HULL calculations using a finer mesh. The only new results that are available to us indicate that we can expect substantial changes (increases) in cloud rise velocity, which result seems more consistent with the photographic results of PDT II-2. Dr. Charles Needham has written a short memorandum presented below, explaining their rezoning. He has also sent to us a plot of maximum "velocity in the grid" versus time as computed earlier [Figure C-1(a)] and used in the predictions contained in this report. He also provided a plot of maximum velocity as obtained from the revised calculations [Figure C-1(b)]. The reader will observe by comparing results of Figure C-1(a) and C-1(b) that the AN/FO rise velocity is considerably greater in the revised calculations. Dr. Needham's memorandum follows.

Memo for the Record

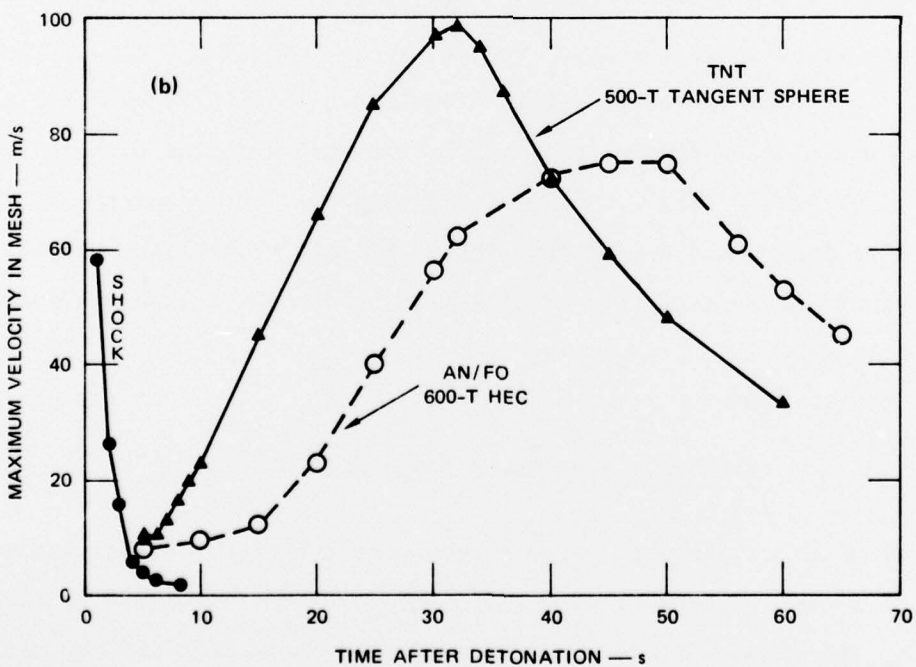
23 August 1976

#### HIGH EXPLOSIVE CLOUD RISE CALCULATIONS

Cloud Rise Calculations have been completed for two high explosive events, a 500-ton tangent sphere of TNT and a 600-ton capped cylinder of AN/FO. The first calculations, in each case, were made with special rezones to carefully follow shock propagation. We found that after a time of half second, the zoning in the vicinity of the fireball became



(a) EARLY CALCULATIONS THAT WERE THINLY ZONED IN FIREBALL REGION



(b) REVISED CALCULATIONS WITH MUCH FINER ZONING IN FIREBALL REGION

FIGURE C-1 MAXIMUM VELOCITY IN ARID vs TIME FOR TWO HIGH-EXPLOSIVE SITUATIONS

too coarse to allow description of the fireball flowfield. A second calculation was performed using as initial conditions, the results of the first calculation at a time of 0.15 seconds. The second calculation used an initial zone size of 2 meters square. A rezone was used so that the zones remained approximately square as the grid expanded. We found that even this method gave zones too large to sufficiently resolve the fireball after five seconds.

A third calculation was made using as initial conditions, the second calculation at a time of 1 second. The third calculation had transmissive top and outer boundary, and no rezone. These calculations were carried to at least sixty seconds.

One additional calculation was made for the 500 ton TNT case. A rezone was used that put five zones in the fireball region. Due to the expense of the calculation it was only carried to 30 seconds.

Those calculations which resulted in large zones in the fireball region, lost resolution of the fireball resulting in no cloud rise.

The calculations which did indicate cloud rise were initially terminated at 30 seconds. This was an unfortunate choice because both high explosive clouds were still accelerating at that time. It therefore appeared that the calculations showed a continuing acceleration for all times. The calculations completed since that time indicate that the maximum velocity is reached at 32 seconds for the tangent sphere case and 45 seconds for the cylinder.

Although these numbers are rather startling at first glance, the effect of the charge geometry is what is seen. The tangent sphere puts out a toe of detonation products along the ground. The amount of products is small compared to the charge weight but the toe establishes a flow in the opposite direction of that necessary for cloud rise. Some time, a few seconds, is required to reverse this flow and allow cloud rise.



In the case of the cylindrical charge, the radial extent of the detonation products is initially much greater than its height. The effect is a slower rise at a later time but approximately the same stability altitude.

There is good reason to believe these calculations because the cloud rise calculations done for Dipole West and Gest experiments are in good agreement with experiment. In addition, the velocities observed in these calculations are smaller than any from nuclear calculations of any yield.

Keep in mind that these are peak material velocities and are between 2 and 3 times greater than the overall cloud rise velocity.

CHARLES E. NEEDHAM  
Project Officer  
Theoretical Branch

# DISTRIBUTION LIST

Organization	No. of Copies	Organization	No. of Copies
<u>DEPARTMENT OF DEFENSE</u>		Director of Defense Research & Engineering	
Director		Department of Defense	
Command Control Technical Center		ATTN: DD/S&SS(OS)	1
ATTN: C-650, G. C. Jones	1	Washington, D.C. 20301	
C-650, W. Heidig	1	Commander	
C-110	1	Field Command	
Pentagon, Room BE 685		Defense Nuclear Agency	
Washington, D.C. 20301		ATTN: FCTMOF	1
Director		FCPR	1
Defense Advanced Research Projects Agency		FCTMOT	3
ATTN: Technical Library	1	FCPRQ	1
Tactical Technical Office	1	Kirtland AFB, NM 87115	
Architect Building		Director	
1400 Wilson Blvd.		Interservice Nuclear Weapons School	
Arlington, VA 22209		ATTN: Document Control	1
Director		Kirtland AFB, NM 87115	
Defense Communications Agency		Director	
ATTN: Code 810, R. W. Rostron	1	Joint Strat TGT Planning	
Code 480	1	Staff JCS	
Washington, D.C. 20305		ATTN: STINFO Library	1
Defense Documentation Center		JPST, Capt. G. D. Goetz	1
ATTN: TC	12	Offutt AFB	
Cameron Station		Omaha, NB 68113	
Alexandria, VA 22314		Chief	
Director		Livermore Division FLD Command	
Defense Intelligence Agency		DNA	
ATTN: DT-1C, Jack Mansfield	1	Lawrence Livermore Laboratory	
DT-2, WPNS & SYS DIV	1	ATTN: FCPRL	1
DT-4B	1	P.O. Box 808	
W. Wittig, DC-7D	1	Livermore, CA 94550	
DIR-4C	1	OJCS/J-3	
Washington, D.C. 20301		The Pentagon	
Director		ATTN: WWMCCS EVAL OFC, Mr. Toma	1
Defense Nuclear Agency		Washington, D.C. 20301	
ATTN: STVL	1	Director	
DDST	1	Telecommunications & COMD & CON SYS	
SPSS	1	ATTN: Scientific Advisor	1
STTL Tech Library	3	Washington, D.C. 20301	
STSI Archives	1		
SPAS	1		
RAAE	3		
RATN	1		
Washington, D.C. 20305			

Organization	No. of Copies	Organization	No. of Copies
<u>DEPARTMENT OF THE ARMY</u>		Commander	
Commander/Director		U.S. Army Comm-Elec Engrg	
Atmospheric Sciences Laboratory		Instal Agency	
U.S. Army Electronics Command		ATTN: EED-PED, George Lane	1
ATTN: DRSEL-BL-D, H. Holt	1	Ft. Huachuca, AZ 85613	
DRSEL-BL-SY-S, F. E. Niles	1	Commander	
White Sands Missile Range, NM 88002		U.S. Army Communications Command	
		ATTN: Technical Library	1
		Ft. Huachuca, AZ 85613	
Director		Commander	
BMD Advanced Technical Center		U.S. Army Electronics Command	
Huntsville Office		ATTN: DRSEL-NL-RD, H. S. Bennet	1
ATTN: ATC-T, Melvin T. Capps	1	Ft. Monmouth, NJ 07703	
ATC-O, W. Davies	1	Director	
ATC-R, W. Dickinson	1	U.S. Army Engr Waterways Exper Sta	
ATC-D, C. Johnson	1	ATTN: Technical Library	1
P.O. Box 1500		Jerry Brown	1
Huntsville, AL 35807		P.O. Box 631	
Program Manager		Vicksburg, MS 39180	
BMD Program Office		Commander	
ATTN: DACS-BMT, John Shea	1	U.S. Army Foreign Science	
5001 Eisenhower Avenue		& Technical Center	
Alexandria, VA 22333		ATTN: P. A. Crowley	1
Commander		220 7th Street, NE	
BMD System Command		Charlottesville, VA 22901	
ATTN: BMDSC-TEN	1	Commander	
SCOM, Myron Pope	1	U.S. Army Materiel Dev &	
P.O. Box 1500		Readiness Command	
Huntsville, AL 35807		ATTN: DRCLDC, J. A. Bender	1
Commander		5001 Eisenhower Avenue	
Harry Diamond Laboratories		Alexandria, VA 22333	
ATTN: DRXDO-TI, Tech Library	1	Commander	
DRXDO-NP, F. N. Wimenitz	1	U.S. Army Missile Command	
2800 Powder Mill Road		ATTN: DRSMI-YTT, W. G. Preussel	1
Adelphi, MD 20783		DRSMI-XS, Chief Scientist	1
Director		Redstone Arsenal, AL 35809	
Trasana		Commander	
ATTN: ATAA-TAC, LtC. John Hesse	1	U.S. Army Nuclear Agency	
TCC/F, Payan Jr.	1	ATTN: MONA-WE, J. Berberet	1
White Sands Missile Range, NM 88002		Technical Library	1
Director		Fort Bliss, TX 79916	
U.S. Army Ballistic Research Labs			
ATTN: DRXBR-X, J. J. Meszaros	1		
Technical Library	1		
J. H. Keefer, DRXBR-TL-IR	1		
Aberdeen Proving Ground, MD 21005			

Organization	No. of Copies	Organization	No. of Copies
<u>DEPARTMENT OF THE NAVY</u>		<u>DEPARTMENT OF THE AIR FORCE</u>	
Chief of Naval Operations		Commander	
Navy Department		Naval Surface Weapons Center	
ATTN: OP 943, LDCR Huff	1	ATTN: Code WA501, Navy NUC	
Washington, D.C. 20350		Programs Office	1
		J. Petes	1
		White Oak, Silver Spring, MD 20910	
Chief of Naval Research		Director	
Navy Department		Strategic Systems Project Office	
ATTN: Code 418	1	Navy Department	
Code 461	1	ATTN: NSP-2141	1
Arlington, VA 22217		NSP-273	1
		NSSP-2722, Fred Wimberly	1
Officer-in-Charge		Washington, D.C. 20376	
Civil Engineering Laboratory			
Naval Construction Battalion Center			
ATTN: Technical Library	1		
Stan Takahashi	1		
Port Hueneme, CA 93041			
Commander			
Naval Electronic System Command			
Naval Electronic Systems Cmd HQS			
ATTN: NAVALEX 034, T. B. Hughes	1		
PME 117-T, Satellite Comm			
Project Office	1		
Washington, D.C. 20360			
Commander			
Naval Ocean Systems Command			
ATTN: Code 2200, W. F. Moler	1		
San Diego, CA 92152			
Commander			
Naval Facilities Engineering Cmd.			
Headquarters			
ATTN: Technical Library	1		
Code 03A	1		
Code 04B	1		
Washington, D.C. 20390			
Director			
Naval Research Laboratory			
ATTN: Code 5430	1		
Code 7701, Jack D. Brown	1		
Code 5180, M. A. Persechino	1		
Code 7700, T. P. Coffey	1		
Code 5460, Radio Electromag	1		
Prop BR	1		
HDQ Command, Dir. Bruce Wald	1		
Washington, D.C. 20375			

<u>Organization</u>	<u>No. of Copies</u>	<u>Organization</u>	<u>No. of Copies</u>
Commander		Los Alamos Scientific Laboratory	
Foreign Technology Division, AFSC		ATTN: Doc Control for R. A. Gentry	1
ATTN: NICD Library	1	Doc Control for Eric Lindman	1
TDFBD, J. D. Pumphrey	1	Doc Control for Eric Jones	1
Wright-Patterson AFB, OH 45433		Doc Control for John S. Malik	1
		Doc Control for John Zinn	1
Commander		Doc Control for R. F. Taschek	1
Rome Air Development Center, AFSC		P.O. Box 1663	
ATTN: EMTLD Doc Library	1	Los Alamos, NM 87545	
Griffiss AFB, NY 13440			
		Sandia Laboratories	
SAMSO/MN		ATTN: Doc Con for A. Dean	
ATTN: MNNH/Maj. Gage	1	Thornbrough, Org 1245	1
MNNL/LtC. Kennedy	1	Doc Con for J. P. Martin,	
Norton AFB, CA 92409		Org 1732	1
(Minuteman)		Doc Con for W. D. Brown,	
		Org 1353	1
SAMSO/RS		Doc Con for T. Wright	1
ATTN: RSSE	1	L. Vortman	1
Post Office Box 92960		P.O. Box 5800	
Worldway Postal Center		Albuquerque, NM 87115	
Los Angeles, CA 90009			
		Union Carbide Corporation	
Commander in Chief		Holifield National Laboratory	
Strategic Air Command		ATTN: Doc Con for Tech Library	1
ATTN: XPFS, Maj. Briam G. Stephan	1	Civ Def Res Proj, Mr. Kearny	1
XOBM	1	P.O. Box X	
ADWATE, Capt. Bruce Bauer	1	Oak Ridge, TN 37830	
NRT	1		
Offutt AFB, NB 68113		<u>OTHER GOVERNMENT</u>	
<u>U.S. ENERGY RESEARCH AND DEVELOPMENT ADMIN</u>		Department of Commerce	
EG&G, Inc.		Office of Telecommunications	
Los Alamos Division		Institute for Telecom Science	
ATTN: J.H.M. Fu	1	ATTN: William F. Utlaut	1
Jim Michaels	1	Library	1
P.O. Box 809		Boulder, CO 80302	
Los Alamos, NM 85544		<u>DEPARTMENT OF DEFENSE CONTRACTORS</u>	
		Acurex Corporation	
University of California		ATTN: Robert M. Kendall	1
Lawrence Livermore Laboratory		485 Clyde Avenue	
ATTN: Technical Info Dept., L-3	1	Mountain View, CA 94040	
B. Hayes	1		
M. Finger	1	Aerospace Corporation	
P.O. Box 808		ATTN: Irving M. Farfunkel	1
Livermore, CA 94550		T. M. Salmi	1
		S. P. Bower	1
		V. Josephson	1
		P.O. Box 92957	
		Los Angeles, CA 90009	



Organization	No. of Copies	Organization	Copies
AVCO Research & Systems Group ATTN: George Weber, J230 201 Lowell Street Wilmington, MA 01887	1	Ford Aerospace & Communications Corp ATTN: J. T. Mattingley, MS X22 3939 Fabian Way Palo Alto, CA 94303	1
Boeing Company ATTN: Aerospace Library Glen Keister P.O. Box 3707 Seattle, WA 98124	1	General Electric Company Space Division Valley Forge Space Center ATTN: Phillip Cline Goddard Blvd. King of Prussia P.O. Box 8555 Philadelphia, PA 19101	1
Brown Engineering Company, Inc. ATTN: N. Passino Romeo A. Deliberis Cummings Research Park Huntsville, AL 35807	1	General Electric Company TEMPO-Center for Advanced Studies ATTN: DASIAC Don Chandler Warren S. Knapp B. Gambill 816 State Street (P.O. Drawer QQ) Santa Barbara, CA 93102	1
Univ. of California at San Diego ATTN: Henry G. Booker 3175 Miramar Road La Jolla, CA 92037	1	General Electric Company ATTN: F. A. Reibert P.O. Box 1122 Syracuse, NY 13201	1
California Research & Technology Inc ATTN: Ken Kreyenhagen 6269 Variel Ave Woodland Hills, CA 91364	1	General Research Corporation ATTN: John Ise, Jr. P.O. Box 3587 Santa Barbara, CA 93105	1
Charles Stark Draper Laboratory Inc ATTN: D. B. Cox 555 Technology Square Cambridge, MA 02139	1	GTE Sylvania, Inc. Electronics Systems GRP-Eastern Div ATTN: Marshal Cross 77 A. Street Needham, MA 02194	1
Civil/Nuclear Systems Corp. ATTN: Robert Crawford 1200 University Blvd., N.E. Albuquerque, NM 87102	1	IIT Research Institute ATTN: A. Longinow 10 West 35th Street Chicago, IL 60616	1
Computer Sciences Corporation ATTN: John Spoor P.O. Box 530 6565 Arlington Blvd. Falls Church, VA 22046	1	Information Science, Inc. ATTN: Walter F. Dudziak 123 West Padre Street Santa Barbara, CA 93105	1
University of Denver Colorado Seminary Denver Research Institute ATTN: Sec Officer for J. Wisotski P.O. Box 10127 Denver, CO 80210	1	Institute for Defense Analyses ATTN: IDA Librarian, Ruth S. Smith Ernest Bauer 400 Army-Navy Drive Arlington, VA 22202	1
ESL, Inc. ATTN: James Marshall 495 Java Drive Sunnyvale, CA 94086	1		

Organization	No. of Copies	Organization	No. of Copies
JAYCOR		Meteorology Research, Inc.	
ATTN: S. R. Goldman	1	ATTN: William D. Green	1
1401 Camino Del Mar		464 West Woodbury Road	
Del Mar, CA 92014		Altadena, CA 91001	
Kaman Avidyne		Mission Research Corporation	
Division of Kaman Sciences Corp		ATTN: Dave Sowle	1
ATTN: E. S. Criscione	1	F. Fajen	1
83 Second Avenue		R. Bogusch	1
Northwest Industrial Park		S. L. Gutsche	1
Burlington, MA 01803		C. L. Longmire	1
Kaman Sciences Corporation		735 State Street	
ATTN: Jerry L. Harper	1	Santa Barbara, CA 93101	
B. J. Bittner	1	The Mitre Corporation	
P.O. Box 7463		ATTN: Chief Scientist, W. Sen	1
Colorado Springs, CO 80933		J. C. Keenan	1
Lockheed Missiles & Space Co. Inc.		C. E. Callahan	1
ATTN: Dept 60-12	1	G. Harding	1
A. Collins, Dept. 81-14	1	S. A. Morin, M/S	1
P.O. Box 504		P.O. Box 208	
Sunnyvale, CA 94088		Bedford, MA 01730	
Lockheed Missiles & Space Company		Pacific-Sierra Research Corp.	
ATTN: Martin Walt, Dept. 52-10	1	ATTN: E. C. Field, Jr.	1
3251 Hanover Street		1456 Cloverfield Blvd.	
Palo Alto, CA 94304		Santa Monica, CA 90404	
Lulejian & Associates, Inc.		Physics International Company	
Los Angeles Operations		ATTN: Doc Con for F. S. Sauer	1
ATTN: R. Daniels	1	Doc Con for Tech Library	1
21515 Hawthorne Blvd.		2700 Merced Street	
Torrance, CA 90503		San Leandro, CA 94577	
M.I.T. Lincoln Laboratory		R & D Associates	
ATTN: Lib, A-082 for D. M. Towle	1	ATTN: Cyrus P. Knowles	1
P.O. Box 73		R. E. LeLevier	1
Lexington, MA 02173		Bryan Gabbard	1
Martin Marietta Aerospace		P.O. Box 9695	
Orlando Division		Marina Del Rey, CA 90291	
ATTN: Roy W. Heffner	1	The Rand Corporation	
P.O. Box 5837		ATTN: Cullen Crain	1
Orlando, FL 32805		1700 Main Street	
McDonnell Douglas Corporation		Santa Monica, CA 90406	
ATTN: Robert W. Halprin	1	Science Applications, Inc.	
5301 Bolsa Avenue		ATTN: John Warner	1
Huntington Beach, CA 92647		D. Sachs	1
		P.O. Box 2351	
		La Jolla, CA 92038	

<u>Organization</u>	<u>No. of Copies</u>	<u>Organization</u>	<u>No. of Copies</u>
Science Applications, Inc. Huntsville Division ATTN: Dale H. Davis 2109 W. Clinton Avenue Suite 700 Huntsville, AL 35805	1	TRW Systems Group San Bernardino Operations ATTN: F. B. Faye, 527/710 P.O. Box 1310 San Bernardino, CA 92402	1
Science Applications, Inc. ATTN: Technical Library P.O. Box 3507 Albuquerque, NM 87110	1	Weidlinger Assoc Consulting Engineers ATTN: Melvin L. Baron 110 East 59th Street New York, NY 10022	1
Science Applications, Inc. ATTN: J. Cockayne William R. Seebaugh John Shannon 8400 Westpark Drive McLean, VA 22101	1 1 1	<u>FOREIGN</u>  Director Defense Research Establishment ATTN: J. Watson C. McKiver	   1 1
Stanford Research Institute ATTN: L. L. Cobb C. L. Rino Alan Burns Donald Nielson W. G. Chesnut Georgellen Smith W. Jaye J. G. Depp P. J. Dolan Robert Bollen V. Elaine Hatfield 333 Ravenswood Avenue Menlo Park, CA 94025	1 1 1 1 1 1 1 1 1 1 1	Suffield Ralston, Alberta, Canada	
System Development Corporation ATTN: E. G. Meyer 4130 Linden Avenue Dayton, Ohio 45432	1		
Systems, Science & Software, Inc. ATTN: Donald R. Grine Technical Library P.O. Box 1620 La Jolla, CA 92038	1 1		
TRW Systems Group ATTN: R. M. Webb, M S R1-1150 R. K. Plebuch, R1-2078 One Space Park Redondo Beach, CA 90278	1 1		